

**SEMMELWEIS EGYETEM**

**DOKTORI ISKOLA**

**Ph.D. értekezések**

**2498.**

**BENKŐ ZSIGMOND**

**Funkcionális Idegtudományok**

című program

Programvezető: Dr. Vizi E. Szilveszter, professor emeritus

Témavezető: Dr. Somogyvári Zoltán, tudományos főmunkatárs

# FROM CLUSTERING TO CAUSALITY ANALYSIS: APPLICATION AND DEVELOPMENT OF SIGNAL PROCESSING METHODS IN A NEUROSCIENCE CONTEXT

PhD thesis

**Zsigmond Benkő**

János Szentágothai Doctoral School of Neurosciences

Semmelweis University



Supervisor: Zoltán Somogyvári, Ph.D

Official reviewers:  
Csaba Kerepesi, Ph.D  
Frigyes Sámuel Rácz, MD, Ph.D

Head of the Final Examination Committee:  
Anita Kamondi, MD, D.Sc

Members of the Final Examination Committee:  
Géza Mészéna, D.Sc  
Péter Barthó, Ph.D

Budapest  
2020

# Contents

<b>Abbreviations</b>	<b>4</b>
<b>1 Introduction</b>	<b>5</b>
1.1 From neuroanatomy to causality analysis . . . . .	5
1.2 Gap Junctions, Connexins and the structure of human retina . . . . .	5
1.3 Dynamical systems . . . . .	6
1.3.1 The logistic map . . . . .	7
1.3.2 Takens theorem and state space reconstruction . . . . .	8
1.3.3 State space reconstruction and the Lorenz system . . . . .	8
1.4 Anomalies and where to find them . . . . .	9
1.5 Intrinsic dimension and the Farahmand-Szepesvari-Audibert estimator . .	13
1.5.1 Intrinsic Dimension . . . . .	13
1.5.2 The Farahmand-Szepesvári-Audibert estimator . . . . .	14
1.6 Analysis of interactions among signals . . . . .	15
1.6.1 Correlation . . . . .	15
1.6.2 Mutual Information . . . . .	16
1.6.3 Cross correlation function and coherence . . . . .	16
1.6.4 Causality analysis . . . . .	17
1.6.5 From cross-correlation to causality . . . . .	18
1.6.6 Granger Causality . . . . .	18
1.6.7 Transfer Entropy . . . . .	19
1.6.8 Convergent Cross Mapping causality . . . . .	20
1.6.9 State-space reconstruction and cross-mapping on coupled logistic maps . . . . .	22
1.7 Local Field Potential and Intrinsic Optical Signal on ex vivo slices . . . .	23
1.7.1 The intrinsic optical signal . . . . .	23
1.7.2 LFP versus IOS and causality . . . . .	23
<b>2 Objectives</b>	<b>25</b>
2.1 Unsupervised identification of clusters in cone pedicle data . . . . .	25
2.2 An algorithm to detect rareness-based outliers in time series . . . . .	25
2.3 An improved measure of intrinsic dimensionality . . . . .	25
2.4 Explore the causal relationship between intrinsic optical signal and Local Field Potential . . . . .	26

<b>3</b>	<b>Methods</b>	<b>27</b>
3.1	Statistical analysis of retinal gap junctions . . . . .	27
3.2	Analysing time series with the Temporal Outlier Factor . . . . .	28
3.2.1	TOF Analysis workflow . . . . .	28
3.2.2	Local Outlier Factor . . . . .	29
3.2.3	Generation of simulated datasets . . . . .	29
3.2.4	Analysis steps on simulations. . . . .	33
3.2.5	Model Evaluation metrics . . . . .	34
3.2.6	Analysis of real-world datasets . . . . .	35
3.3	Simulations and FSA dimension-analysis details . . . . .	37
3.3.1	Simulations . . . . .	37
3.3.2	Comparison on synthetic benchmark datasets . . . . .	40
3.3.3	Dimension estimation of interictal and epileptic dynamics . . . . .	41
3.4	Causality analysis between LFP and IOS . . . . .	42
3.4.1	Experimental procedures . . . . .	42
<b>4</b>	<b>Results</b>	<b>46</b>
4.1	Detecting clusters in slices of retinal cell pedicles . . . . .	46
4.2	An algorithm to detect unique events in time series . . . . .	46
4.2.1	Temporal Outlier Factor . . . . .	46
4.2.2	Mean and variance for $q = 1$ . . . . .	51
4.2.3	Mean and variance for $q = 2$ . . . . .	51
4.2.4	Evaluation of performance on simulated data series . . . . .	53
4.2.5	TOF detects unicorns . . . . .	58
4.2.6	Application examples on real-world data series . . . . .	59
4.3	Estimating intrinsic dimensionality to explore seizure dynamics . . . . .	62
4.3.1	Manifold adaptive dimension estimator revisited . . . . .	62
4.3.2	Results on synthetic benchmarks . . . . .	67
4.3.3	Analysing epileptic seizures . . . . .	69
4.4	Investiating the causal relation between Local Field Potential ant Intrinsic Optical Signal . . . . .	70
4.4.1	The slow and the fast components of the IOS signal . . . . .	72
4.4.2	Time delayed causality between LFP power and the fast compo- nent of IOS . . . . .	73
4.4.3	Causality versus correlation . . . . .	78
4.4.4	Autonomous dynamics of IOSh without discharges . . . . .	79
4.4.5	Reconstruction of IOSh based on LFP . . . . .	80
4.4.6	Simulations . . . . .	83

<b>5</b>	<b>Discussion</b>	<b>84</b>
5.1	About the clusters of cell pedicules in the OPL of the human retina . . . .	84
5.2	About unicorns and the Temporal Outlier Factor . . . . .	84
5.3	About the cmFSA algoritm . . . . .	87
5.4	About IOS and its relation to LFP . . . . .	88
<b>6</b>	<b>Conclusions</b>	<b>92</b>
6.1	Determination of clusters based on cell pedicule-features . . . . .	92
6.2	Temporal Outlier Factor to detect unique events . . . . .	92
6.3	The corrected median Farahmand-Szepesvari-Audibert intrinsic dimen- sionality estimator . . . . .	92
6.4	Causal relationship between local field potential and intrinsic optical signal	93
<b>7</b>	<b>Summary</b>	<b>94</b>
<b>8.</b>	<b>Összefoglalás</b>	<b>95</b>
<b>9</b>	<b>Bibliographies</b>	<b>96</b>
<b>10</b>	<b>Publications</b>	<b>109</b>
<b>11</b>	<b>Acknowledgements</b>	<b>110</b>

## Abbreviations

<b>4AP</b>	<b>4-aminopyridine</b>
<b>ACSF</b>	<b>Artificial CerebroSpinal Fluid</b>
<b>CCM</b>	<b>Convergent Cross Mapping</b>
<b>cmFSA</b>	<b>corrected median Farahmand–Szepesvári–Audibert</b>
<b>CSD</b>	<b>Current Source Density</b>
<b>Cx36</b>	<b>Connexin 36</b>
<b>DANCo</b>	<b>Dimensionality from Angle and Norm Concentration</b>
<b>ECG</b>	<b>ElectroCardioGram</b>
<b>EM</b>	<b>Expectation Maximization</b>
<b>FSA</b>	<b>Farahmand–Szepesvári–Audibert</b>
<b>GJ</b>	<b>Gap Junction</b>
<b>ID</b>	<b>Intrinsic Dimension</b>
<b>IEI</b>	<b>Inter Event Interval</b>
<b>IOS</b>	<b>Intrinsic Optical Signal</b>
<b>IOSh</b>	<b>Intrinsic Optical Signal high frequency component</b>
<b>IOSl</b>	<b>Intrinsic Optical Signal low frequency component</b>
<b>LFP</b>	<b>Local Field Potential</b>
<b>LIBOR</b>	<b>London Interbank offered rate</b>
<b>LOF</b>	<b>Local Outlier Factor</b>
<b>mFSA</b>	<b>median Farahmand–Szepesvári–Audibert</b>
<b>MIND ML</b>	<b>MIInimum Neighbor Distance Maximum Likelihood</b>
<b>MIND KL</b>	<b>MIInimum Neighbor Distance Kullback-Leibner divergence</b>
<b>ML</b>	<b>Maximum Likelihood</b>
<b>MPE</b>	<b>Mean Percentage Error</b>
<b>OPL</b>	<b>Outer Plexiform Layer</b>
<b>ROC AUC</b>	<b>Reciever Operating Characteristic area under curve</b>
<b>ROI</b>	<b>Region Of Interest</b>
<b>SD</b>	<b>Standard Deviation</b>
<b>SE</b>	<b>Standard Error</b>
<b>STIM</b>	<b>electric stimulation</b>
<b>TOF</b>	<b>Temporal Outlier Factor</b>

# 1 Introduction

## 1.1 From neuroanatomy to causality analysis

Neural data analysis has many faces and every novel signal processing approach opens up new possibilities to explore brain anatomy and function. In this thesis I take a deep dive into data analysis: I apply already existing tools and develop new methods to explore neural phenomena. During this journey I use the inventory of probability theory and nonlinear time series analysis. First I examine retinal slices by unsupervised learning. Second I develop a new anomaly detection method to detect unique events in time series and we apply it to detect apnoea, gravitational wave and insider trading. Third I improve an intrinsic dimension estimator and draw epileptic seizure complexity maps from EEG measurements. Fourth I explore and model the causal relationship between optical and electric signals in neural tissue by causality detection.

## 1.2 Gap Junctions, Connexins and the structure of human retina

I give a brief description of Gap Junctions (GJs) and connexins in the context of the human retina focusing on the retinal Outer Plexiform Layer (OPL).

GJs connect two cells electrically and chemically by permitting the diffusion of ions and small molecules up to 1 kDa [1, 2]. They can be observed at sites, where the cell membranes are aligned and only a small gap exists (1-2 nm) between the two membranes.

Connexins are transmembrane proteins with a special poreforming function at GJs. Six connexin (a so called hexamer) form a connexon half-channel, which together with another half-channel forms a pore connecting two cells. The permeability of the pore depends on the type of connexin monomers and the intracellular molecular environment of the connected cells [3, 4]. More than 20 connexins have been described in mammals with molecular sizes ranging from 21 to 70 kDa [4]. Retinal connexins in GJs have been shown to take part in the visual signalprocessing [5].

The human retina has a strictly organized structure consisting of ten layers (Fig. 1). The main functions of this layered structure are photoreception by cones and rods, visual signal processing by the intermediary layers and to convey visual information towards the brain via ganglion cell axons through the optic nerve. The histologic layers reflects the local anatomy of the tissue, the OPL is located at the first synaptic layer of the retina. The synapses in this layer are mainly between receptor cells – rods and cones – and bipolar cells or horizontal cells.

In the mammalian retina, connexin-36 (Cx36) and connexin-45 was found in both plexiform layers [6, 7] and the former shows the same expression pattern in humans [8].

The access to the electrical circuits of human retina has been problematic because of the disintegration of the available post mortem tissue. Thus, it is still not clear if the human retina has the same type of GJ connections as other species.

There are three main cone types in the human retina: the L, the M, and the S types. These groups show more or less specific sensitivities to different regions of the electromagnetic spectrum. The pigment of L (Long wavelength) cones shows absorption-peak at 564 nm (red), the M (Medium wavelength) cones' pigment has a peak at 534 nm (green) and the S (Short wavelength) cones carry a pigment with an absorption-peak at 420 nm (blue) [9]. This division of the spectrum makes RGB colorvision possible in humans.

In terms of function, we see that separate groups could be distinguished in the retinal cone cell population, but the question arises that whether or not this functional difference is reflected by the structure on a cellular level. More specifically: how many different groups can be distinguished based on the morphology of the synaptic pedicles in the OPL? The answer to this question could bear relevant information about the signal processing in first synaptic layer of the human retina.

In this work – as a part of characterizing the connexin36 GJs in the outer human retina – we conduct an unsupervised analysis of cone pedicles in the OPL.

### 1.3 Dynamical systems

Dynamical systems are systems with a state space, whose state changes according to an update rule [11].

One can talk about discrete time and continuous time dynamical systems. Discrete time dynamical systems are defined by a map, which can be applied recursively on the state to generate the process (Eq 1).

$$x_{t+1} = f(x_t) \tag{1}$$

where  $x_t$  is the state of the system,  $f$  is the generating map.

Continuous time dynamical systems can be represented by a flow (Eq. 2):

$$x(t) = \phi_t(x(0)) \tag{2}$$

Here  $x(t)$  is the system's state and  $\phi_t$  is the flow, which determines the time evolution of the system from an initial condition  $x(0)$ .

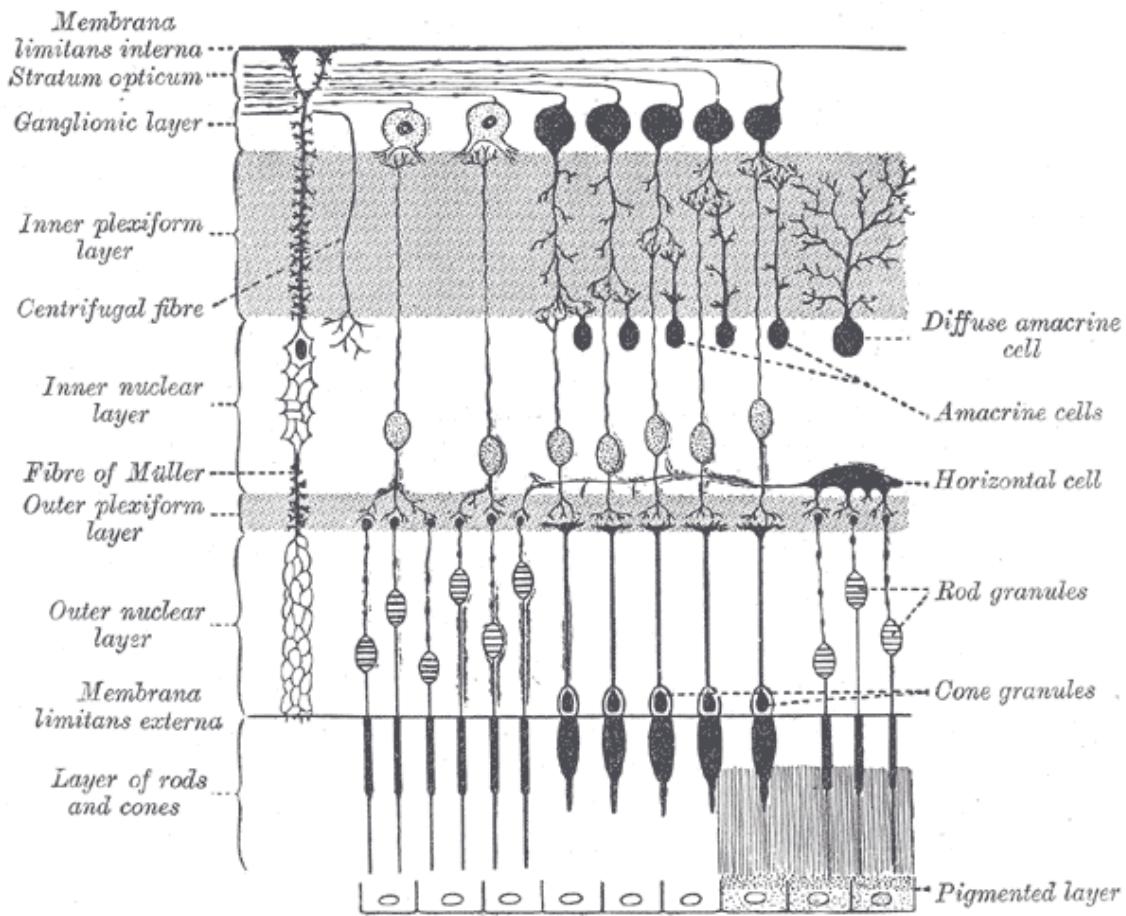


Figure 1: **The structure of the human retina [10].** The Outer Plexiform Layer is the first synaptic layer which is located between the inner nuclear and the outer nuclear layers. Synapses are formed between receptor cells and bipolar or horizontal cells. (Image source: <https://www.bartleby.com/107/illus882.html>)

### 1.3.1 The logistic map

The logistic map is a discrete time nonlinear dynamical system, a workhorse of nonlinear signalprocessing methods exhibiting potentially complex behavior [12].

The update rule is a quadratic function (Eq. 3).

$$x_t = rx_{t-1}(1 - x_{t-1}) \quad (3)$$

where  $x_t$  is the state of the system at time  $t$  and  $r$  is a parameter.

The meaningful domain of the parameter is the  $[0, 4]$  interval, and depending on its value the system can exhibit simple periodic oscillations or chaotic behavior. Above  $r \approx 3.56995$  the system shows chaotic behaviour for most parameter values and initial conditions [12]. At  $r = 4$  also the invariant measure can be computed over the state space [13].

### 1.3.2 Takens theorem and state space reconstruction

The dynamical state of the system can be reconstructed from scalar time series [14] by taking the temporal context of each point according to Takens embedding theorem [15]. This theorem forms the basis of nonlinear time series analysis, therefore we quote it here as stated by Huke [16]:

**Theorem 1.** (Takens) *Let  $M$  be a compact manifold with a dimensionality of  $d$ . For pairs  $(f, y)$  with  $f \in \text{Diff}^2(M)$  and  $y \in C^2(M, \mathbb{R})$  it is a generic property that  $\Phi : M \mapsto \mathbb{R}^{2d+1}$ , defined by*

$$\Phi_{(f,y)}(x) = (y(x), y(f(x)), y(f^2(x)), \dots, y(f^{2d}(x))) \quad (4)$$

*is an embedding.*

By 'generic' we mean that 'good' pairs form open and dense set in all possible pairs.

If we take the pair of dynamics (flow or generating map) and an observation function  $(x)$ , then the procedure in Eq. 4 can be implemented via time delay embedding:

$$X(t) = [x(t), x(t + \tau), x(t + 2 * \tau), \dots, x(t + (E - 1) * \tau)] \quad (5)$$

where  $X(t)$  is the reconstructed state at time  $t$ ,  $x(t)$  is the scalar time series. This procedure has two parameters: the embedding delay ( $\tau$ ) and the embedding dimension ( $E$ ). If  $E$  is sufficiently big ( $E > 2 * d$ ) compared to the dimension of the attractor ( $d$ ) and some mild conditions are met, then the embedded (reconstructed) space is topologically equivalent to the system's state space (see Theorem 1, [15, 16]). Moreover, it has been shown that overembedding can tackle challenges posed by nonstationary signals, if  $E > 2 * (d + p)$ , where  $p$  is the number of slowly changing nonstationary parameters [17]. In the over-embedded state space, different values of  $p$  maps into different state space domains.

As a consequence of Takens theorem, small neighborhoods around points in the reconstructed state-space also form neighborhoods in the original state space, therefore a small neighborhood around a point represents nearly similar states. This topological property has been leveraged to perform nonlinear prediction [18], noise filtering [19, 20] and causality analysis [21–24].

### 1.3.3 State space reconstruction and the Lorenz system

We demonstrate time delay embedding on the Lorenz system [25]. The Lorenz system is a continuous-time dynamical system, an abstract model for atmospheric convection

described by the following differential equation system:

$$\begin{aligned}
 \dot{x} &= \sigma(y - x) \\
 \dot{y} &= x(\rho - z) - y \\
 \dot{z} &= xy - \beta z
 \end{aligned} \tag{6}$$

Where  $x$ ,  $y$  and  $z$  are the state variables, and  $\sigma$ ,  $\rho$  and  $\beta$  are constant parameters.

In certain parameter- and initial condition-combinations the system shows chaotic behaviour. Then the state evolves on a nonperiodic orbit in the state space and converges to a strange attractor [26] (Fig. 2 A). This attractor has two wings, and the system switches between these two quite irregularly.

To reconstruct the system's state from the  $x$ ,  $y$  and  $z$  variables separately, we apply time delay embedding. We can reconstruct the system's state from both the  $x$  and the  $y$  variables alone, and the resulting trajectory draws out a slightly distorted version of the original attractor (Fig. 2 B, C). However one can not reconstruct the state of the system from the  $z$  variable alone, because the information about which wing the system was on is lost due to special symmetry of the attractor to this coordinate (Fig. 2 D).

## 1.4 Anomalies and where to find them

Anomalies in time series are rare and non-typical patterns that deviate from normal observations and may indicate a transiently activated mechanism different from the generating process of normal data. Accordingly, recognition of anomalies is often important or critical, invoking interventions in various industrial and scientific applications.

Anomalies can be classified according to various aspects [27]. Based on their appearance, these non-standard observations can be point outliers, whose amplitude is out of range from the standard amplitude or contextual outliers, whose measured values do not fit into some context. A combination of values can also form an anomaly named a collective outlier. Thus, in case of point outliers, a single point is enough to distinguish between normal and anomalous states, whilst in the case of collective anomalies a pattern of multiple observations is required to recognize the outliers. Based on their generation process, two characteristic examples of extreme events are black swans [28] and dragon kings [29]. Black swans are generated by a power law process and they are usually unpredictable by nature. In contrast, the dragon king, such as stock market crashes, occurs after a phase transition and it is generated by different mechanisms from normal samples making it predictable. Both black swans and dragon kings are extreme events easily recognizable post-hoc (retrospectively), but not all the anomalies are so effortless to detect. Even post-hoc detection can be a troublesome procedure when the amplitude of the event

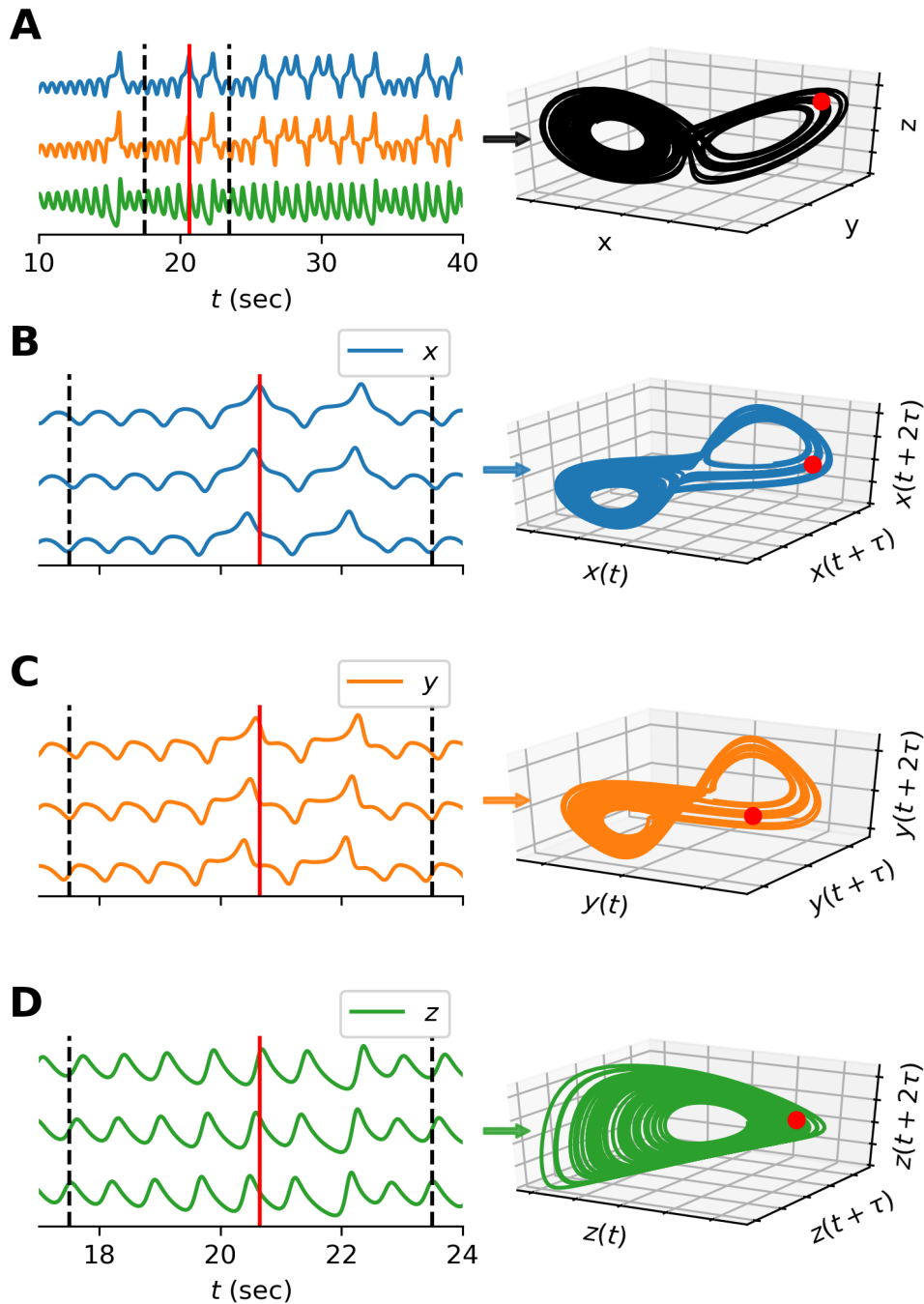


Figure 2: **Time delay embedding the Lorenz system.** **A** Simulation of the Lorenz system. Time series of the  $x$  (blue),  $y$  (orange) and  $z$  (green) variables is shown at the left and the trajectory in the state-space is shown at the right. Also, the state at a time-moment is drawn (red line and red circle). **B** State space reconstruction from the  $x$  variable. The original and the time shifted versions of  $x_t$  is shown at the left and the reconstructed state space is shown at the right. **C** State space reconstruction from the  $y$  variable. **D** Attempt for state space reconstruction from the  $z$  variable. The original and the time shifted versions of  $z_t$  is shown at the left and the reconstructed state space is shown at the right. In this last case, the state can not be reconstructed.

does not fall out of the data distribution.

Although the definition of an anomaly is not straightforward, two of its key features include rarity and dissimilarity from normal data.

Most, if not all the outlier detection algorithms approach the anomalies from the dissimilarity point of view. They search for the most distant and deviant points without much emphasis on their rarity. In contrast, our approach is the opposite: we quantify the rarity of a state, largely independent of the dissimilarity.

Here we introduce a new type of anomaly, the unique event, which is not an outlier in the classical sense of the word: it does not necessarily lie out from the background distribution, neither point-wise, nor collectively. A unique event is defined as a unique pattern which appears only once during the investigated history of the system. Based on their hidden nature and uniqueness one could call these unique events "unicorns" and add them to the strange zoo of anomalies. Note that unicorns can be both traditional outliers appearing only once or patterns that do not differ from the normal population in any of their parameters.

But how do you find something you've never seen before, and the only thing you know about is that it only appeared once? Although the answer would be straightforward for discrete patterns, it is more challenging for continuous variables (where none of the states are exactly the same) to distinguish the unique states from dynamical point of view.

Classical supervised, semi-supervised and unsupervised strategies have been used to detect anomalies [27, 30, 31] and recently deep learning techniques [32–34] were applied to detect extreme events of complex systems [35]. Supervised outlier detection techniques can be applied to identify anomalies, when labeled training data is available for both normal and outlier classes. Semi-supervised techniques also utilize labeled training data, but this is limited to the normal or the outlier class. Model based pattern matching techniques can be applied to detect specific anomalies with best results when the mechanism causing the anomaly is well known and simple [36]. However when the background is less well known or the system is too complex to get analytical results (or to run detailed simulations), it is hard to detect even specific types of anomalies with model-based techniques due to the unknown nature of the waveforms. Model-free unsupervised outlier detection techniques can be applied to detect unexpected events from time series in cases when no tractable models or training data is available. This Exploratory Data Analysis (EDA) is the opposite of the conventional modeling framework: events are detected from time-series, then the detected parts are interpreted by domain experts. Several detection methods can be run in unsupervised mode, including the  $k$  nearest neighbors (kNN) distance-based anomaly detection techniques, which are amongst the simplest methods. A widely used example for this approach is the standard Local Outlier Factor (LOF) algorithm [37],

which was also adapted to time series data [38].

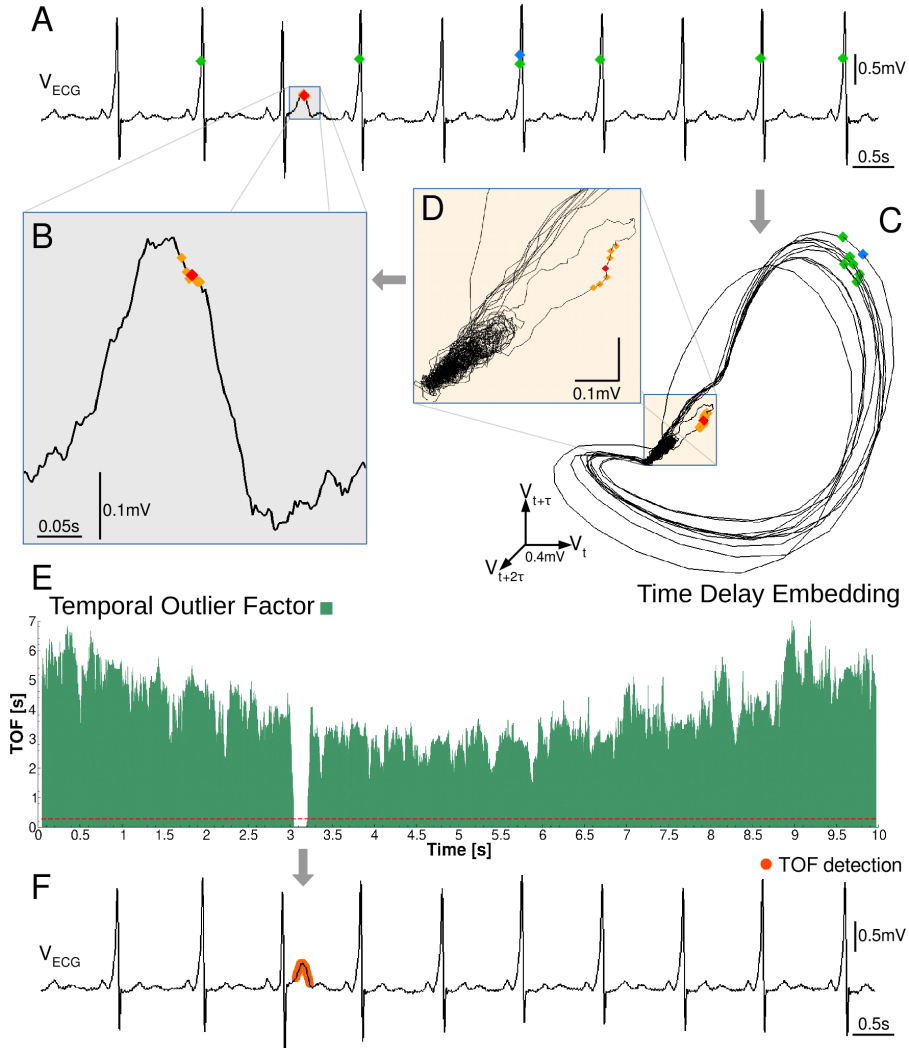


Figure 3: **Schema of our unique event detection method and the Temporal Outlier Factor (TOF).** **a** An ECG time series from a patient with Wolff-Parkinson-White Syndrome, a strange and unique t-wave zoomed on the graph **b**. **c** The reconstructed attractor in the 3D state space by time delay embedding ( $E=3$ ,  $\tau = 0.011s$ ). Two example states (red and blue diamonds) and their 6 nearest states space neighbors (orange and green diamonds respectively) are shown. The system returned several times back to the close vicinity of the blue state, thus the green diamonds are evenly distributed in time, on graph **a**. In contrast, the orange state space neighbors of the red point (zoomed on graph **d**) are close to the red point in time as well on graph **b**. These low temporal distances show that the red point marks a unique event. **e** TOF measures the temporal dispersion of the  $k$  nearest state space neighbors ( $k = 20$ ). Red dashed line is the threshold  $\theta = 0.28s$ . Low values of TOF below the threshold mark the unique events, denoted by orange dots on the original ECG data on graph **f**.

To adapt collective outlier-detection to time series data, nonlinear time series analysis provides the possibility to generate the multivariate state space from scalar observations

[14,15]. Naturally, time delay embedding can be introduced as a preprocessing step before outlier detection (with already existing methods i.e. LOF) to create the contextual space for collective outlier detection from time series.

Besides the spatial information preserved in reconstructed state space, temporal relations in small neighborhoods can contain clues about the dynamics. For example recurrence time statistics were applied to discover nonstationary time series [39,40], to measure attractor dimensions [41–43] and to detect changes in dynamics [44,45].

In the followings we introduce a new method leveraging nonlinear time series analysis and temporal information to quantify uniqueness, which forms an effective tool to find unicorns.

## 1.5 Intrinsic dimension and the Farahmand-Szepesvari-Audibert estimator

### 1.5.1 Intrinsic Dimension

Dimensionality sets profound limits on the stage where data takes place, therefore it is often crucial to know the intrinsic dimension of data to carry out meaningful analysis. Intrinsic dimension provides direct information about data complexity, as such, it was recognised as a useful measure to describe the dynamics of dynamical systems [46], to detect anomalies in time series [47], to diagnose patients with various conditions [48–51] and to use it simply as plugin parameter for signal processing algorithms.

Most of the multivariate datasets lie on a lower dimensional manifold embedded in a potentially very high-dimensional embedding space. This is because the observed variables are far from independent, and this interdependence introduces redundancies resulting in a lower intrinsic dimension (ID) of data compared with the number of observed variables. To capture this – possibly non-linear – interdependence, nonlinear dimension-estimation techniques can be applied [24, 52–54].

To estimate the ID of data various approaches have been proposed, for a full review of techniques see the work of Campadelli et al. [55]. Here we discuss the  $k$ -Nearest Neighbor (kNN) ID estimators, with some recent advancements in the focus.

A usually basic assumption of  $k$ NN ID estimators is that the fraction of points in a neighborhood is approximately determined by the intrinsic dimensionality ( $D$ ) and distance ( $R$ ) times a – locally almost constant – mostly density-dependent factor ( $\eta(x, R)$ , Eq. 7).

$$\frac{k}{n} \approx \eta(x, R) * R_k^D \quad (7)$$

where  $k$  is the number of samples in a neighborhood and  $n$  is the total number of samples on the manifold.

Assuming a Poisson sampling process on the manifold Levina and Bickel [56] derived a Maximum Likelihood estimator, which became a popular method and got several updates [57, 58]. These estimators are prone to underestimation of dimensionality because of finite sample effects and overestimations because of the curvature.

To address the challenges posed by curvature and finite sample, new estimators were proposed [59–62]. To tackle the effect of curvature, a minimal neighborhood size can be taken on normalized neighborhood distances as in the case of  $\text{MIND}_{\text{ML}}$  [59]. To tackle the underestimation due to finite sample effects, empirical corrections were applied. A naive empirical correction approach was applied by Camastra and Vinciarelli [63]: a perceptron was trained on the estimates computed for randomly sampled hypercubes to learn a correction function. Motivated by the correction in the previous work, the IDEA method was created [59]; and a more principled approach was carried out, where the full distribution of estimates was compared to the distributions computed on test data sets using the Kullback-Leibner divergence ( $\text{MIND}_{\text{KL}}$  [59],  $\text{DANCo}$  [61]). In the case of  $\text{DANCo}$ , not just the nearest neighbor distances, but the angles are measured and taken into account in the estimation process resulting in more accurate estimates.

In the recent years, further estimators have been proposed, such as the estimator that uses minimal neighborhood information leveraging the empirical distribution of the ratio of the nearest neighbors to fit intrinsic dimension [62], or other approaches based on simplex skewness [64] and normalized distances [65–68].

### 1.5.2 The Farahmand-Szepesvári-Audibert estimator

In the following section, we revisit the manifold adaptive dimension estimator proposed by Farahmand et al. [69] to measure intrinsic dimensionality of datasets. From Eq. 7 we can take the logarithm of both sides:

$$\begin{aligned} \ln\left(\frac{k}{n}\right) &\approx \ln \eta + D \ln R_k \\ \ln\left(\frac{2k}{n}\right) &\approx \ln \eta + D \ln R_{2k} \end{aligned} \tag{8}$$

If  $\eta$  is slowly varying and  $R$  is small, we can take it as a constant.

If we subtract the two equations from each other we get:

$$\ln(2) \approx D \ln\left(\frac{R_{2k}}{R_k}\right) \tag{9}$$

Thus, to compute the local estimates, we fit a line through the log-distance  $k$ th and  $2k$ th nearest neighbor at a given location.

$$d(x) = \frac{\ln(2)}{\ln(R_{2k}/R_k)} \quad (10)$$

To compute a global ID estimate, the authors proposed the mean of local estimates at sample-points, or a vote for the winner global ID value (the mode), if the estimator is used in integer-mode. They proved that the above global ID estimates are consistent for  $k > 1$ , if  $\eta$  is differentiable and the manifold is regular. They calculated the upper bound for the probability of error for the global estimate, however this bound contains unknown constants [69].

In this work we propose an improved FSA estimator, based on the assumption that the density is locally uniform. We suggest to use the median of local values for a global intrinsic dimension estimate. We correct the underestimation effect by an exponential formula and test the new algorithm on benchmark datasets. We apply the proposed estimator to locate epileptic focus on field potential measurements.

## 1.6 Analysis of interactions among signals

### 1.6.1 Correlation

Linear correlation coefficient ( $\rho_{xy}$ ) is the simplest and most natural measure to quantify association between two signals:

$$\rho_{xy} = \frac{\sum_t (x_t - \mu_x)(y_t - \mu_y)}{N\sigma_x\sigma_y}$$

where  $x_t$  and  $y_t$  are the data points of two time series,  $\mu_x$  and  $\mu_y$  are their respective mean values,  $\sigma_x$  and  $\sigma_y$  are the respective standard deviations, and  $N$  is the number of data points.

This correlation method assumes that signals depend on each other linearly and that there is no time delay between the analyzed signals; linear dependency effectively means that the signals have the same waveforms in the case of time series.

In the case of macroscopic electric signals from the brain, high correlation, and thus high instantaneous linear coupling, is often the consequence of electric cross-talk between electrodes and wires or the effect of far fields. If high correlation is observed, care should be taken to eliminate these effects.

Besides the assumption of instant and linear interaction, the correlation method has a third important constraint: it is a symmetric measure, and hence, an undirected measure of connection strength. There are methods to exceed these limitations and overcome these

three constraints, but there is no one perfect method. The simplicity of the linear correlation is always an advantage because it not only requires less computational resource, but more importantly less data and is also less sensitive to noise.

### 1.6.2 Mutual Information

The most important symmetric connection measure, which can reveal any types of non-linear dependencies, is mutual information. It is based on the entropy measure of a signal and quantifies the information known about a random variable with knowledge of an other random variable. Specifically, it calculates the difference between the entropy of the joint distribution of the two variable ( $H(X, Y)$ ) and the entropies of the individual variables ( $H(X), H(Y)$ ):

$$I(X; Y) = H(X) + H(Y) - H(X, Y)$$

Although it can reveal nonlinear connections, its calculation requires constructing probability density functions for each marginal variable and for the joint variable, typically by means of histograms. Much more data is typically required to determine the full probability distribution function with the necessary precision, especially when compared to the simpler linear correlation method. Generally, calculation of mutual information requires more data and more computational efforts, but rarely gives proportionally more information about the existence of the interaction. It is because the majority of the interactions, even the nonlinear forms can be approximated linearly to some extent, thus can be revealed by linear correlation, and those forms of interactions are rare which can not be approximated linearly at all, thus can not be revealed by correlation.

### 1.6.3 Cross correlation function and coherence

The cross correlation function measures the linear correlation coefficient between one signal and a time-delayed version of a second signal as a function of the time delay between the two signals, thereby overcoming the instantaneous assumption of the simple linear correlation:

$$\rho_{xy}(\tau) = \frac{\sum_t (x_t - \mu_x)(y_{t+\tau} - \mu_y)}{N\sigma_x\sigma_y}.$$

Here,  $\rho_{xy}(\tau)$  is the correlation coefficient for  $\tau$  time lag and  $y_{t+\tau}$  is the  $\tau$ -lagged version of the time series  $y_t$ .

The cross correlation function is also used to determine two functions: cross-spectrum ( $S_{xy}(\omega)$ ) and its normalized version called the coherence ( $C_{xy}(\omega)$ ) given by

$$C_{xy}(\omega) = \frac{|S_{xy}(\omega)|^2}{|S_{xx}(\omega)||S_{yy}(\omega)|}$$

Specifically, the cross spectrum  $S_{xy}(\omega)$ , also called cross-spectral density, is the Fourier transform of the cross-correlation function.

Coherence expresses the stability of the phase lag on different frequency regimes between the two time series. As a Fourier-spectrum, coherence represents phase relations with complex numbers. High amplitude in a given frequency regime means that the two oscillations follow each other by a constant phase lag through the majority of the time, whereas small amplitude means that the phase lag changes randomly in that frequency regime. The specific phase lag between the two signals is contained by the argument of the complex number. By using complex wavelet transform, instead of Fourier transform, even temporal changes in the phase coherence and phase lag can be described.

An interesting application of coherence can be found in the micro electric imaging concept introduced by Somogyvári et al. [70], where they applied coherence clustering on Local Field Potential (LFP) recordings of high-density micro-electrode arrays implanted in the hippocampus of the rat. They performed the coherence clustering in different frequency bands and by this, he could identify the anatomical structure of the hippocampus based solely on the LFP recordings.

Applying this coherence clustering method to neocortical micro-electrode recordings resulted in a less clear structure, but supragranular, granular and infragranular layers can be identified clearly on the micro-electroanatomical structure [70, 71].

Coherence were applied to identify differences in subtypes of temporal lobe epilepsies [72]. Walker et al. [73] found excessive delta and theta power in slow foci in all intractable patients, and hypocoherence in theta in 75% of patients. In this study, the aim for neurofeedback training was to restore the normal, healthy coherence pattern between EEG channels. When power and coherence abnormalities could be restored by the neurofeedback training, patients become seizure free [73].

#### **1.6.4 Causality analysis**

Detecting causal relations between observed components would be extremely useful to exploit the vast amount of data provided by measurement technologies to understand complex systems such as the ecosystem of our planet or the human brain.

David Hume was the first, who approached causal effect from an empirical viewpoint and introduced the notion of counterfactual statements [74].

We define causal effect between two variables – in the spirit of Hume and Miguel Hernán [75] – through counterfactual statements, that is changed values of one variable would have led to different future values of the other variable, meanwhile values of all the

other variables are kept unchanged at the present (Eq. 11).

$$x_{t+i} = f_i(x_t, y_t, \theta_t) \quad (11)$$

$$y \rightarrow x := \exists y'_t \neq y_t : f_i(x_t, y_t, \theta_t) \neq f_i(x_t, y'_t, \theta_t) \quad (12)$$

Where  $x_{t+i}$  and  $x_t$  are the value of  $x$  in the future and in the present respectively and  $i > 0$ .  $f_i$  is a stochastic or deterministic function determining the time evolution of  $x$ .

In real world cases, it is almost impossible to test the outcome of counterfactuals, therefore additional assumptions are necessary to infer causal structures. On the one hand as a standard approach for emulating counterfactuals, randomized experiments were introduced to ensure the exchangeability of elements, allowing the approximation of the average causal effect in a population [75–77]. On the other hand observational causal discovery methods were invented to infer causal relations based purely on observations [78] or specifically time series observations [21, 79, 80]. These latter methods use stationarity and ergodicity assumptions to ensure, that during the time evolution, the system visits the all the  $(x, y)$  state pairs necessary to evaluate the counterfactuals .

### 1.6.5 From cross-correlation to causality

The cross correlation function, as well as coherence spectrum, could be used to determine directional effects between the analyzed signals based on the phase of the peak, corresponding to the time delay between the signals in a given frequency (eq. phase lag index). However, this approach builds on two main assumptions. First, it assumes that there are no difference in the observational delays for the two signals; second, it assumes similar wave-shapes on the two channels, as it is based on the linear correlation coefficient implicitly. Although both assumptions can be valid in many situations, it is hard to verify them in general.

### 1.6.6 Granger Causality

The majority of causality analysis methods are based on Norbert Wiener’s principle on predictability: a time series is said to be causal to an other, if it’s inclusion makes the prediction of the caused time series more precise [79]. The first practical and applicable implementation of this principle is the Granger-causality introduced by Clive Granger in 1969 [81]. The Granger formalization is based on auto-regressive (AR) models, where the next element of a time series is approximated by the linear mixture on the recent elements.

Specifically, the formalization can be written as follows:

$$\begin{aligned}
 x_t &= \sum_{i=1}^p a_i x_{t-i} + \varepsilon_t \\
 x_t &= \sum_{i=1}^p b_i x_{t-i} + \sum_{j=1}^q c_j y_{t-j} + \eta_t \\
 F_{y \rightarrow x} &= \log \left( \frac{\sigma_\varepsilon^2}{\sigma_\eta^2} \right)
 \end{aligned}$$

where  $a_i$ ,  $b_i$  and  $c_j$  are the AR coefficients;  $p$  and  $q$  control the order of the models;  $\varepsilon_t$  and  $\eta_t$  are error residuals;  $\sigma$ -s are the variances of residual errors and  $F_{y \rightarrow x}$  is the directed Granger-causality index. Inclusion of the recent past of the other time series into the auto-regressive model does not necessarily result in the same improvement of prediction error in both directions, thus  $F_{y \rightarrow x}$  and  $F_{x \rightarrow y}$  are generally non-equal. The original Granger method quantifies the effect of including the other time series using the log-ratio of the variance of the residual error signal between a prediction with the other time series and a prediction without the other time series.

Since then, numerous versions and improvements of the original Wiener-Granger idea exist. Directed transfer function and Partial Directed Coherence solve the Granger problem in the frequency domain instead of time domain [82–84]. Conditional or multivariate Granger causality includes non-pairwise comparisons and there are nonlinear extensions as well. A version of Granger-causality called short-time directed transfer function has been adapted to analyze the event related activity, developed by [85] and applied to reveal information transmission during visual stimulation of the brain.

### 1.6.7 Transfer Entropy

A non-parametric translation of Norbert Wiener's original idea to information theory's language is Transfer Entropy introduced by Thomas Schreiber in 2008 [86]. Transfer Entropy quantifies the predictive information transfer, the Mutual Information between present X values and past Y states ( $Y^-$ ) conditioned on past X states ( $X^-$ ):

$$TE(Y \rightarrow X) = I(X; Y^- | X^-)$$

Transfer Entropy and Granger causality are equivalent in the case of jointly Gaussian variables. TE was used to reconstruct interaction delays in turtle visual system and for various other applications [87]. There are several toolboxes for the computation of TE, for example JIDT with python bindings or TRENTOOL for MATLAB.

### 1.6.8 Convergent Cross Mapping causality

A new approach of causal discovery were introduced by George Sugihara based on theorems of nonlinear dynamical systems [88]. Given a dynamical system whose state changes with time, from the current state, one can predict all the coming future states, if time evolution rules are known. The actual state is a point in state space, the space with state variables on each axis. As time evolves, the system's state traces out a trajectory in state space. In many cases, the system's state is attracted to a lower dimensional subset of state space and the points form a manifold.

Sugihara's idea is based on Takens theorem [89]. Deyle and Sugihara [90] generalized Takens theorem into a multivariate form, when not only the different time lags of a time series provides the state-space embedding, but different observation functions of the same dynamical systems as well. Based on this theorem, they found a new principle for causality analysis: The new idea is that if two time series measurements ( $X, Y$ ) were from the same dynamical system, then the reconstructed state spaces can be mapped back to the same original manifold, and so, there should also be a smooth mapping between the two reconstructed state spaces. In this case, one can identify causality between the two variable as well.

An asymmetrical relationship between the variables can also be revealed when their original state-spaces are not the same, but one of them is a lower dimensional sub-manifold, a (not necessarily linear) projected version of the other. The mapping works in one direction, but is non-invertible. In this case, one can speak about unidirectional causal relationship, wherein one variable causes the other variable but not the reverse.

If there are no such mappings between the two reconstructed manifolds, they do not belong to the same dynamical system. In this case, one can say that there is no causality between the two variables. Convergent Cross-Mapping is a procedure which tests the existence of this mapping. It is considered a cross-mapping procedure, because it estimates the mapping between the two reconstructed manifolds; it is considered convergent because this estimate converges to the true mapping as one lengthens the time series.

To check the existence of the casual effect of  $x$  on  $y$ , the steps of the CCM procedure are as follows :

1. State space reconstruction from the scalar time series.

One can apply time delay embedding to reconstruct the state of the system, where a modified version of Eq. 5 ensures a time-centered embedding

$$Y(t) = [y(t - D\tau), \dots, y(t), \dots, y(t + D\tau)] \quad (13)$$

Where  $y(t)$  denotes the original time series,  $Y(t)$  is the time series of the embedded,

$E = 2D + 1$  dimensional vectors and  $\tau$  is the delay used for the embedding.

2. Fitting a mapping function by robust local kNN regression. The algorithm runs through all the points of  $Y(t)$  and identify a local neighborhood around each point. The  $E + 1$  nearest neighbor points  $Y(t_i)$  are chosen and a weighting factor  $W_i(t)$  is calculated for each neighbor  $Y(t_i)$  through: 1, normalizing the distances by the distance of the closest neighbor  $Y(t_1)$ ; 2, using an exponential kernel; 3, renormalizing the sum to 1:

$$W_i(t) = \frac{e^{-\frac{|Y(t_i)-Y(t)|}{|Y(t_1)-Y(t)|}}}{\sum_i^{E+1} e^{-\frac{|Y(t_i)-Y(t)|}{|Y(t_1)-Y(t)|}}} \quad (14)$$

where,  $|Y(t_i) - Y(t)|$  denotes the Euclidean distance between the  $i^{th}$  closest neighbor  $Y(t_i)$  and the original point  $Y(t)$  in the embedding space.

3. Compute predictions based on the mapping. An estimation  $\hat{x}(t)$  is calculated from  $x(t)$  as a weighted average of the mapped  $x(t_i)$  points, by using the  $W_i(t)$  weight factors:

$$\hat{x}(t) = \sum_i W_i(t) * x(t_i) \quad (15)$$

4. Evaluation of the model-fit. The estimated  $\hat{x}(t)$  and the original  $x(t)$  time series are compared by calculating the linear correlation coefficient between them:

$$CCM_{x \rightarrow y} = r(x, \hat{x}) \quad (16)$$

High values of the  $CCM_{x \rightarrow y}$  show, that the consequence  $y(t)$  contains information about the cause  $x(t)$ , thus refers to the existence of a directed causal connection from the cause to the consequence. Causality  $CCM_{y \rightarrow x}$  in the reverse direction calculated similarly, only the role of the  $x$  and  $y$  is reversed.

Ye et al. [91] extended the original CCM method by introducing time delay between the cause and consequence and examining the causal relationships at many time lags. Parallel work of Schumacher et al. is based on similar principles and also contains time delay detection and in addition they applied their method to neural data [92].

There are various methods to test the existence of the smooth mapping between the reconstructed trajectories. Ma et al. used a feed forward neural network to explicitly estimate the smooth mapping between the embedded times series. When the mapping error was sufficiently small, they detected a causal relationship, otherwise they said that the two time series were independent in the time segment [93].

CCM works well on deterministic data and when there is direct causality between variables, but it cannot detect hidden common causes. So far, we found only one attempt in the data analysis literature to distinguish direct causality from common cause, but this method has yet to be applied neural data [94]. Moreover the cross-talk or linear mixing, which always appears between multiple electric signals recorded in a volume conductor restricts the applicability of CCM on raw extracellular signals. Due to linear mixing, each of the recorded signals contains the effect of all neural sources with different weights. Thus, all the sources can be reconstructed from all recorded mixtures to some extent, resulting false detection of circular causal connections between all recordings. To avoid these false positive detections, determination of the individual sources from the measured potentials is necessary and the causality analysis should be applied between the reconstructed time series of the sources, instead of potentials. This could be achieved by current source density calculation [95–99] or linear demixing due to independent component analysis [100].

### 1.6.9 State-space reconstruction and cross-mapping on coupled logistic maps

State variables are  $x$  and  $y$  and the state of the system is  $(x_t, y_t)$  at time  $t$ . The update rule for time evolution is:

$$f : x_t = rx_{t-1}(1 - x_{t-1}) \quad (17)$$

$$g : y_t = ry_{t-1}(1 - y_{t-1} - \beta x_{t-1}) \quad (18)$$

where  $r$  is a constant parameter, and  $\beta$  is the coupling constant.

We can express  $x_{t-1}$  from Eq. 18:

$$w : x_{t-1} = \frac{1 - y_{t-1} - \frac{y_t}{ry_{t-1}}}{\beta} \quad (19)$$

So we could reconstruct  $x_{t-1}$  from  $Y_t = (y_t, y_{t-1})$ . From the function composition  $(f \circ w)(Y_t) = x_t$  we can also reconstruct  $x_t$ . From this follows, that we could reconstruct any  $x_\delta$ , where  $\delta \geq t - 1$  with  $(f \circ f \circ f \circ \dots \circ f \circ w)(Y_t) = x_\delta$ .

In contrast, using  $x_{t-1}$  alone, one can not infer  $y_t$ , because  $y_{t-1}$  is also present in Eq. 18. So one can try to express  $y_{t-1}$  with the help of  $x_{t-2}$ , but then  $y_{t-2}$  shows up in the equation. This can be continued to the initial condition  $x_0$  and  $y_0$ , but  $y_0$  is unknown.

From these we can see, that the time-delay embedding with  $D = 2$  and  $\tau = 1$  applied on  $y_t$  is enough to reconstruct the state of the system. So we can build the dynamics solely on the  $Y$  state-space alone (no need for  $x_t$ ):

$$y_{t+1} = ry_t(1 - y_t - \beta(f \circ w)(Y_t)) \quad (20)$$

Also, from here we can predict the time-shift properties between X and Y

$$(y_t, y_{t-1}) \rightarrow (x_t, x_{t-1}) \quad (21)$$

## 1.7 Local Field Potential and Intrinsic Optical Signal on ex vivo slices

### 1.7.1 The intrinsic optical signal

Different methods are used to monitor activity-dependent changes in nervous tissue, when both neuronal and glial cell function may be altered. Beside detection of fast electrical changes with different electrophysiological approaches, optical techniques can also be used to follow neuronal activity with a non-invasive manner [101, 102]. The intrinsic optical signal (IOS) quantifies the changes of optical properties of the tissue by measuring the transmitted or the reflected light in brain slices. Contrary to the in vivo IOS method, the in vitro IOS is independent of the blood flow changes, and it may develop as a result of different cellular processes, such as ionic movement across the membranes, synaptic activity and metabolic changes, which may cause cell swelling or shrinkage [103]. These volumetric changes of both neural and glial cells lead to changes in the light scattering properties of the tissue, thus it is widely accepted, that they form the basis of the IOS generation: swelling of the cells decreases the scattering, thus increases the transmittance of the tissue [101–105]. Although most of these processes are slow, there are evidences of faster IOS components as well, which may change on time scales similar to the electrophysiological signals.

### 1.7.2 LFP versus IOS and causality

While the correlation between electrical- and intrinsic optical signals has been known for a long while [104, 106], the precise causal relationship of electrical and intrinsic optical signals has not yet been analyzed in detail. In spite of several studies, it is not yet clarified, how different IOS components parallel develop, and it is also questionable, which types of underlying processes are consecutively activated [107]. Epileptiform activity can be easily provoked in acute brain slices in various ways. Different chemicals, i.e., 4-aminopyridine (4AP) applied into the incubation solution results in spontaneous epileptic discharges in hippocampal or cortical brain slices [108]. In  $Mg^{2+}$ -free solution, spontaneous epileptiform activity develops with slightly different characteristics [109]. Strong electrical stimulation of the white matter results in after-discharges, which can be regarded as an electrically evoked epileptiform activity [110]. The aim of our present investigation

was to analyze the processes of IOS generation following seizure induction in acute brain slices, when both fast and slow IOS components are detectable [111].

The correlated appearance of epileptiform electrophysiological and IOS signals raised the question of the direction and type of the causal connection between them. At least two alternative hypothesis can be set up for the causal relation between the activity observed in the local field potential (LFP) and the activity dependent IOS components: On one hand, it is possible that the epileptiform activity causes the osmotic changes, and the resulting swelling of the cells is measured by the IOS, while the electrophysiological activity develops and runs independently from those osmotic changes. In this case a unidirectional causal drive would exist from the LFP to the IOS. On the other hand, it is also possible that the changes within the ionic concentration, reflected by the IOS signal, have a feedback effect on the epileptic activity, presumably determining the termination and the recurrence of the epileptic bursts. In this case, circular or bidirectional causal connection would exist between the LFP and the IOS signals.

As the CCM, introduced by Sugihara et al. [88] and extended to delayed causal effects by Ye et al. [91], is well suited to determine both unidirectional and circular causal couplings, we applied this method in this work, to determine the causal relationship between the electrophysiological and optical signals.

## **2 Objectives**

### **2.1 Unsupervised identification of clusters in cone pedicle data**

At the outer synapse layer of the human retina cone cells contact and interact with each other and with bipolar cells through gap junctions. We attempt to explore that whether different types of cone pedicles can be distinguished in a statistically robust manner in the human outer retina. We will use lognormal mixture model, fit by the expectation maximization algorithm and Bayesian information criteria for model selection to determine the optimal number of clusters.

### **2.2 An algorithm to detect rareness-based outliers in time series**

Outliers are rare and different compared with normal samples. Most outlier detection algorithms use explicitly the latter – difference – criteria to identify outliers.

We develop a new outlier detection algorithm, which explicitly leverages the rareness of anomalies. We will call the new method as Temporal Outlier Factor (TOF). We will compare the performance of TOF algorithm with the performance of the density-based Local Outlier Factor (LOF). We will investigate on various real-world datasets, that whether this rareness-based approach provides us with excess information or not, compared with the density-based anomaly detection approach.

### **2.3 An improved measure of intrinsic dimensionality**

Intrinsic dimensionality provides a direct measure of data complexity and the reliability of such information is often crucial to convey successful data analysis.

Here, we will formulate the probability density function of the – manifolds adaptive – Farahmand-Szepesvari-Audibert intrinsic dimensionality estimator to develop more reliable methods estimating intrinsic dimension of datasets. Given the probability density function, we attempt to calculate maximum likelihood solution, then we investigate possible improvements in the Farahmand-Szepesvari algorithm. We will benchmark the original and improved algorithm against the classical Levina-Bickel and DANCo estimators. We will leverage the improved estimator to map out the dynamics of epileptic seizures from human intracranial EEG recordings.

## **2.4 Explore the causal relationship between intrinsic optical signal and Local Field Potential**

The intrinsic optical signal stems from the reflection and absorption changes of the neural tissue caused by mostly the swelling due to osmotic changes. Therefore, it has complex connections with the electrical environment and the measured local field potentials, but this relationship is highly unexplored.

We apply Convergent Cross Mapping algorithm – a causal discovery technique leveraging theorems of nonlinear dynamical systems – to explore the causal relationship between intrinsic optical signal and local field potential measured in rodent brain-slices during resting state and evoked seizure events. We will compare the results of the analysis with the ones produced with linear cross-correlation function and further explore the implications of this comparison. Finally we will build an empirical model – based on the exploratory analysis – to infer one signal from the other, if it is possible.

## 3 Methods

### 3.1 Statistical analysis of retinal gap junctions

For experimental procedures see Kantor et al [112]. We then estimated the probability density function ( $P(x)$ ) of the pedicle area, the convex hull area and the number of Cx36 plaques with a weighted sum of log-normal components for each case:

$$P(x) = \sum_{k=1}^K \pi_k p_k(x) \quad (22)$$

where  $K$  is the number of components and  $\pi_k$  is the mixing coefficient of the  $k$ -th component. The coefficients are normalized, that is  $\sum_{k=1}^K \pi_k = 1$ .  $p_k(x)$ -s are the log-normal components which are given by:

$$p_k(x) = \frac{1}{x\sigma_k\sqrt{2\pi}} \exp\left(-\frac{(\log x - \mu_k)^2}{2\sigma_k^2}\right) \quad (23)$$

where  $\mu$  and  $\sigma$  are the location and the shape parameters of the distribution, respectively. We fitted the model through maximization of the likelihood given the model using an iterative procedure called the Expectation Maximization (EM) algorithm. The likelihood is the probability of the data set given the parameters:

$$\mathcal{L} = P(\text{data}|\pi, \mu, \sigma) = \prod_{i=1}^n P(x_i) \quad (24)$$

The data set is the co-occurrence of observed data points ( $x_i$ ), so the probability of the data set is the product of the  $n$  individual data-point probabilities (here, we assumed that the data points are independent and identically distributed). We initialized the parameters randomly and then waited 800 iteration steps, this procedure was repeated 20 times and the solution with maximal likelihood was accepted. We performed the above procedure for a different number of components (from 1 to 9). The optimal number of components ( $\star K$ ) was chosen according to the Bayesian Information Criterion (BIC). BIC shows the optimality of a model by introducing a trade-off between the likelihood and model complexity:

$$\text{BIC}(K) = -2 \log \mathcal{L} + (3K - 1) \log n \quad (25)$$

The first term on the right-hand side is the negative logarithm of the likelihood, which is a monotonically decreasing function of  $K$ . In the second term is the number of free fitted parameters, namely the log-scale, the shape and the mixing coefficient for each component

and minus one due to the normalization restriction for mixing coefficients. This latter term is a monotonically increasing function of  $K$ , acting as a penalty for the number of parameters, which is a simple estimate of model complexity. The optimal model has the smallest BIC value.

## 3.2 Analysing time series with the Temporal Outlier Factor

### 3.2.1 TOF Analysis workflow

1. Preprocessing and applicability check:

This step varies from case to case, and depends on the data or on the goals of analysis. Usually it is advisable to make the data stationary. For example, in the case of oscillatory signals, the signal must contain many periods even from the lowest frequency components. If this latter condition does not hold, then Fourier filtering can be applied to get rid of the low frequency components of the signal.

2. Time delay embedding:

We embedded the scalar time series into an  $E$  dimensional space with even time delays ( $\tau$ , Eq. (5), Fig. 4 a). The embedding parameters can be set with prior knowledge of the dynamics or by other optimization methods. Such optimization methods include the first minimum or zerocrossing of the autocorrelation function (for delay selection), the false nearest neighbor method [113, 114] or the differential entropy based embedding optimizer that we applied [115].

3. kNN Neighbor search:

We search for  $k$ -Neighborhoods around each data-point in state-space and save the distance and temporal index of neighbors.

4. Compute TOF score:

We compute the TOF score according to equation (51).

5. Apply a threshold  $\theta$  on TOF score to detect unicorns (Fig. 4 c):

The threshold can be established by prior knowledge, by clustering techniques or supervised learning. The maximum event length parameter ( $M$ ) determines the level of threshold on TOF score (Eq. 56): we set the threshold according to prior knowledge about the longest possible occurrence of the event. After thresholding, we may apply a padding around detected points with symmetric window length  $w = k/2$ , since the  $k$  parameter sets the minimal length of the detectable events.

We implemented these steps in the python programming language (python 3). Time delay embedding and embedding parameter optimization was carried out by custom python scripts. We used the scikit-learn package [116] to calculate LOF, and the neighbor search was established by the kd-tree algorithm of the scipy package [117].

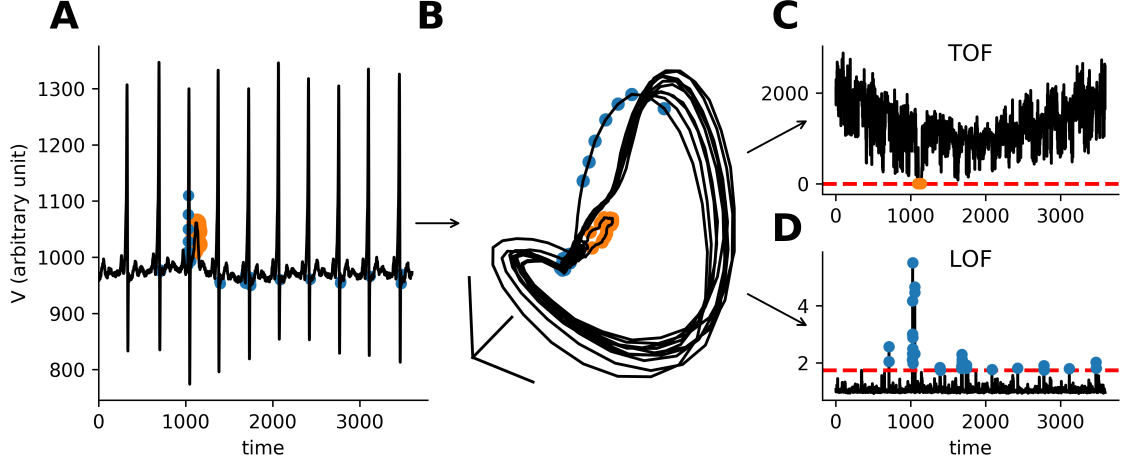


Figure 4: **The workflow for TOF and LOF analysis for time series.** (a) We start with a time series generated by a dynamical system, orange and blue marks TOF and LOF detections respectively. (b) As a next step of our analysis we apply time delay embedding, then kNN search in the reconstructed state-space. (c) We calculate TOF and LOF scores and apply thresholds on the outlier scores to detect anomalies.

### 3.2.2 Local Outlier Factor

The Local Outlier Factor [37] compares local density around a point ( $X$ ) with the density around its neighbors (Eq. 26).

$$\text{LOF}_k(X) = \frac{1}{|N_k(X)|} \sum_{o \in N_k(X)} \frac{\text{lrd}_k(o)}{\text{lrd}_k(X)} \quad (26)$$

Where  $|N_k(X)|$  is the cardinality of the  $k$ -distance neighborhood of  $X$ ,  $\text{lrd}_k$  is the local reaching density for  $k$ -neighborhood (see Breunig et al. [37] for details, Fig. 4).

### 3.2.3 Generation of simulated datasets

**Simulation of outlier datasets.** We simulated 4 systems: logistic map with linear tent map outlier segment, logistic map with linear outlier segment, simulated ECG data with tachycardia outlier segment and random walk with linear outlier segment. The first three datasets stem from deterministic dynamics, whereas the last simulated dataset has stochastic nature.

We generated 100 time series from each type, the length and the position of outlier segments were determined randomly in each case.

**Logistic map with tent-map anomaly.** 100 instances of logistic map data-series were simulated ( $N = 2000$ ) with one randomly (uniform) inserted outlier period in each dataset. The length of outlier periods was randomly chosen with length between  $(2 - 200)$ . The basic dynamics in normal conditions were governed by the update rule:

$$x_{t+1} = rx_t(1 - x_t) \quad (27)$$

where  $r = 3.9$ . The equation was changed during anomaly periods:

$$x_{t+1} = 1.59 - 2.15 \times |x_t - 0.7| - 0.9 \times x_t. \quad (28)$$

**Logistic map with linear anomaly.** The background generation process exhibited the logistic dynamics (Eq. 27) while the anomaly can be described by linear time dependence:

$$x_{t+1} = a * x_t + x_t \quad (29)$$

Here we used  $a = \pm 0.001$ , where the sign of the slope is positive by default and changes when the border of the  $(0, 1)$  domain is reached ensuring reflective boundary condition.

**Random walk data with linear anomaly.** We simulated 100 instances of multiplicative random walks with 2-200 time-step long linear outlier-insets. The generation procedure was as follows:

1. Generate  $w_i$  random numbers from a normal distribution with  $\mu = 0.001$  and  $\sigma = 0.01$
2. Transform  $w_i$  to get the multiplicative random walk data as follows:  $x_i = \prod_{j=1}^i (1 + w_j)$
3. Draw the length ( $L$ ) and position of outlier-section from discrete uniform distributions between  $2 - 200$  and  $1 - (N - L)$  respectively.
4. Use linear interpolation between the section-endpoint values.

**Simulated ECG datasets with tachyarrhythmic segments.** We generated artificial ECG data series according to the model of Ryzhii and Ryzhii [118]. The pacemakers of

the heart: the sinoatrial node (SA), the atroventriclular node (AV) and the His-Purkinje system (HP) are simulated by van der Pol equations:

$$SN \begin{cases} \dot{x}_1 &= y_1 \\ \dot{y}_1 &= -a_1 y_1 (x_1 - u_{11})(x_1 - u_{12}) - f_1 x_1 (x_1 + d_1)(x_1 + e_1) \end{cases} \quad (30)$$

$$AV \begin{cases} \dot{x}_2 &= y_2 \\ \dot{y}_2 &= -a_2 y_2 (x_2 - u_{21})(x_2 - u_{22}) - f_2 x_2 (x_2 + d_2)(x_2 + e_2) + K_{SA-AV} (y_1^{\tau_{SA-AV}} - y_2) \end{cases} \quad (31)$$

$$HP \begin{cases} \dot{x}_3 &= y_3 \\ \dot{y}_3 &= -a_3 y_3 (x_3 - u_{31})(x_3 - u_{32}) - f_3 x_3 (x_3 + d_3)(x_3 + e_3) + K_{AV-HP} (y_2^{\tau_{AV-HP}} - y_3) \end{cases} \quad (32)$$

where the parameters were set according to Ryzhii [118]:  $a_1 = 40$ ,  $a_2 = a_3 = 50$ ,  $u_{11} = u_{21} = u_{31} = 0.83$ ,  $u_{12} = u_{22} = u_{32} = -0.83$ ,  $f_1 = 22$ ,  $f_2 = 8.4$ ,  $f_3 = 1.5$ ,  $d_1 = d_2 = d_3 = 3$ ,  $e_1 = 3.5$ ,  $e_2 = 5$ ,  $e_3 = 12$  and  $K_{SA-AV} = K_{AV-HP} = f_1$ .

The following FitzHugh-Nagumo equations describe the atrial and ventricular muscle depolarization and repolarization responses to pacemaker activity:

$$\text{P wave} \begin{cases} \dot{z}_1 = k_1 (-c_1 z_1 (z_1 - w_{11})(z_1 - w_{12}) - b_1 v_1 - d_1 v_1 z_1 + I_{AT_{De}}) \\ \dot{v}_1 = k_1 h_1 (z_1 - g_1 v_1) \end{cases} \quad (33)$$

$$\text{Ta wave} \begin{cases} \dot{z}_2 = k_2 (-c_2 z_2 (z_2 - w_{21})(z_2 - w_{22}) - b_2 v_2 - d_2 v_2 z_2 + I_{AT_{Re}}) \\ \dot{v}_2 = k_2 h_2 (z_2 - g_2 v_2) \end{cases} \quad (34)$$

$$\text{QRS} \begin{cases} \dot{z}_3 = k_3 (-c_3 z_3 (z_3 - w_{31})(z_3 - w_{32}) - b_3 v_3 - d_3 v_3 z_3 + I_{VN_{De}}) \\ \dot{v}_3 = k_3 h_3 (z_3 - g_3 v_3) \end{cases} \quad (35)$$

$$\text{T wave} \begin{cases} \dot{z}_4 = k_4 (-c_4 z_4 (z_4 - w_{41})(z_4 - w_{42}) - b_4 v_4 - d_4 v_4 z_4 + I_{VN_{Re}}) \\ \dot{v}_4 = k_4 h_4 (z_4 - g_4 v_4) \end{cases} \quad (36)$$

where  $k_1 = 2 \times 10^3$ ,  $k_2 = 4 \times 10^2$ ,  $k_3 = 10^4$ ,  $k_4 = 2 \times 10^3$ ,  $c_1 = c_2 = 0.26$ ,  $c_3 = 0.12$ ,  $c_4 = 0.1$ ,  $b_1 = b_2 = b_4 = 0$ ,  $b_3 = 0.015$ ,  $d_1 = d_2 = 0.4$ ,  $d_3 = 0.09$ ,  $d_4 = 0.1$ ,  $h_1 = h_2 = 0.004$ ,  $h_3 = h_4 = 0.008$ ,  $g_1 = g_2 = g_3 = g_4 = 1$ ,  $w_{11} = 0.13$ ,  $w_{12} = w_{22} = 1$ ,  $w_{21} = 0.19$ ,  $w_{31} = 0.12$ ,  $w_{32} = 0.11$ ,  $w_{41} = 0.22$ ,  $w_{42} = 0.8$ .

The input-currents ( $I_i$ ) are caused by pacemaker centra.

$$I_{\text{ATDe}} = \begin{cases} 0 & \text{for } y_1 \leq 0 \\ K_{\text{ATDe}} y_1 & \text{for } y_1 > 0 \end{cases} \quad (37)$$

$$I_{\text{ATRe}} = \begin{cases} -K_{\text{ATRe}} y_1 & \text{for } y_1 \leq 0 \\ 0 & \text{for } y_1 > 0 \end{cases} \quad (38)$$

$$I_{\text{VNDe}} = \begin{cases} 0 & \text{for } y_3 \leq 0 \\ K_{\text{VNDe}} y_3 & \text{for } y_3 > 0 \end{cases} \quad (39)$$

$$I_{\text{VNRe}} = \begin{cases} -K_{\text{VNRe}} y_3 & \text{for } y_3 \leq 0 \\ 0 & \text{for } y_3 > 0 \end{cases} \quad (40)$$

where  $K_{\text{ATDe}} = 4 \times 10^{-5}$ ,  $K_{\text{ATRe}} = 4 \times 10^{-5}$ ,  $K_{\text{VNDe}} = 9 \times 10^{-5}$  and  $K_{\text{VNRe}} = 6 \times 10^{-5}$ .

The net ECG signal is given by the weighted sum of muscle depolarization and repolarization responses:

$$ECG = z_0 + z_1 - z_2 + z_3 + z_4 \quad (41)$$

where  $z_0 = 0.2$  is a constant offset.

We simulated 100 instances of  $t = 100$  seconds long ECG data with base rate parameter chosen from a Gaussian distribution ( $f_1 \sim \mathcal{N}(\mu = 22, \sigma = 3)$ ). We randomly inserted 2 – 20 seconds long fast heart-beat segments by adjusting the rate parameter ( $f_1 \sim \mathcal{N}(\mu = 82, \sigma = 3)$ ). The simulations were carried out by the `ddeint` python package, with simulation time-step  $\Delta t = 0.001$  from random initial condition and warm-up time of 2 seconds. Also, a  $10\times$  rolling-mean down-sampling was applied on the data series before analysis.

**Generating non-unique anomalies dataset.** To show the selectiveness of TOF for the detection of unicorns, we simulated logistic map data with two tent-map outlier segments. The governing equations were the same as in the previous section, but instead of one, we randomly placed two non-overlapping outlier segments into the time series during data generation, ( $N = 2000$ ,  $L = 20 - 200$ ).

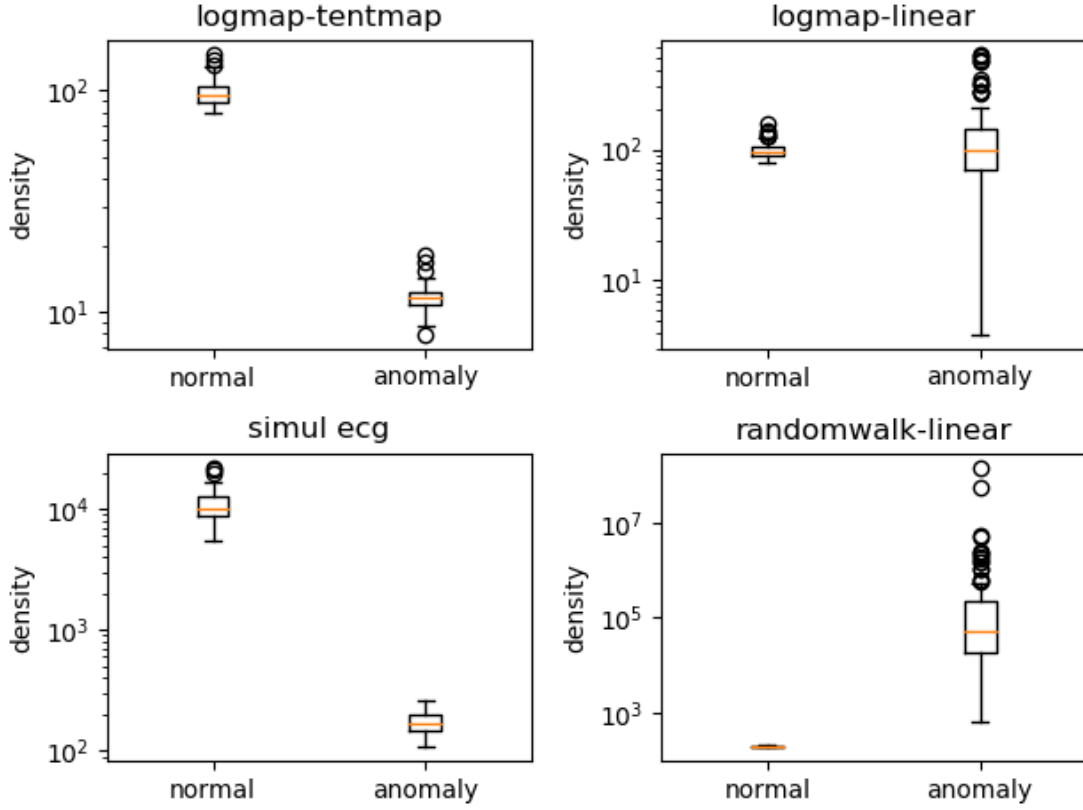


Figure 5: **Point density in normal and anomalous data.** The density around each data point is computed by the inverse distance from the  $k$ -th neighbor ( $E = 3, \tau = 1, k = 20$ ).

### 3.2.4 Analysis steps on simulations.

We applied optional preprocessing, embedded the time series, then applied TOF and LOF with specific threshold value and neighborhood size on all simulated datasets.

For logistic map with tent map anomaly datasets no preprocessing was applied. Since the generated dynamics is known and simple, we could chose embedding parameters manually, without any sophisticated selection criteria. The dynamics is approximately one dimensional ( $d = 1$ ), therefore  $E = 3$  is sufficient to embed the dynamics according to Takens theorem ( $2d + 1 = 3$ ). Also for this discrete time dynamics  $\tau = 1$  is a good choice of embedding delay. The expected anomaly length was calculated from the simulations and the threshold was set accordingly, more specifically  $M = 110$  time steps (Eq. 42).

$$M = \frac{L_{\max} + L_{\min}}{2} = \frac{200 + 20}{2} = 110 \quad (42)$$

Where  $L$  is the possible length of inserted anomalies. Since this event length is 5.5 % of the whole data series' length, we set LOF threshold to detect the top 5.5 % of points based on LOF score. The neighborhood size was scanned between 1 and 100 points and ROC

AUC was computed on the range for TOF and LOF. Also the  $F_1$ , precision and recall score were calculated, where  $k_{\text{TOF}=4}$  neighbors and the best neighborhood size based on ROC AUC were selected for TOF and LOF respectively. We used this setting for  $k_{\text{TOF}}$  as an uninformed rule of thumb, since  $E + 1$  points define a simplex in embedding-space determining unequivocally the position of the neighborhood's center. For LOF we used  $k_{\text{LOF}} = 28$ . This parameter setting scheme was used for all simulated datasets.

For the logistic map with linear anomaly segment datasets we set the parameters as in the tent map anomaly's case, the only difference being that the neighborhood size for LOF was set to  $k_{\text{LOF}} = 28$  as the maximal place of ROC AUC.

For the simulated ECG data we applied a tenfold down-sampling, thus sampling period became  $\Delta t = 0.01$  s. The dynamics seems approximately 2 dimensional, so we set  $E = 3$ , which may be enough to reconstruct the dynamics, also  $\tau = 0.01$  s was set as embedding delay. The threshold was set to  $M = 11$  for TOF and 11% for LOF as the expectation of tachycardia event length. The neighborhood size was scanned for ROC AUC values, and  $k = 4$  and  $k = 99$  were used to compute  $F_1$  score, precision and recall for TOF and LOF respectively.

We applied a logarithmic difference for the multiplicative random walk with linear anomaly dataset as a preprocessing step in order to get rid of nonstationarity in the time series (Eq. 43).

$$y_t = \log(x_t) - \log(x_{t-1}) \quad (43)$$

where  $x$  is the original time series,  $\log$  is the natural logarithm and  $y$  is the preprocessed time series. Embedding parameters were set to  $E = 3$  and  $\tau = 1$  arbitrarily, since the basic dynamics is stochastic. We set the event threshold parameter to  $M = 110$  and 5.5% for TOF and LOF respectively. We also used  $k_{\text{TOF}} = 4$  and  $k_{\text{LOF}} = 1$  since the later was the maximal of a ROC AUC performance scanning.

On the logistic map with two tent-map anomalies dataset we did not apply any preprocessing and we set the embedding parameters to  $E = 3$  and  $\tau = 1$ . Also the neighborhood size was set to  $k_{\text{TOF}} = 4$  and  $k_{\text{LOF}} = 28$  for TOF and LOF respectively. We calculated the ROC AUC values for each simulated instance and plotted these values as the function of inter event interval (Fig. 16).

### 3.2.5 Model Evaluation metrics

We used precision, recall,  $F_1$  score and ROC-AUC to evaluate the detection-performance on the simulated datasets.

The precision metrics characterizes how precise the detections were:

$$\text{precision} = \frac{\text{true positives}}{\text{true positives} + \text{false positives}} \quad (44)$$

The recall evaluates what fraction of the points to be detected were actually detected:

$$\text{recall} = \frac{\text{true positives}}{\text{true positives} + \text{false negatives}} \quad (45)$$

$F_1$  score is a mixture of precision and recall and it provides a single scalar to rate model performance:

$$F_1 = 2 \frac{\text{precision} \times \text{recall}}{\text{precision} + \text{recall}} \quad (46)$$

As an alternative evaluation metrics we applied the area under Receiver Operating Characteristic curve [119]. The ROC curve consists of point-pairs of True Positive Rate (recall) and False Positive Rate parameterized by a threshold ( $\alpha$ , Eq. 47).

$$ROC(\alpha) := (\text{precision}(\alpha), \text{FPR}(\alpha)) \quad (47)$$

where  $\text{FPR} = 1 - \text{recall}$  is the false positive rate and  $\alpha \in [-\infty, \infty]$ .

We computed the median and median absolute deviance from the 100 simulations on each simulated datasets (Fig. 15).

### 3.2.6 Analysis of real-world datasets

**Polysomnography data-set.** We analysed a part of the first recording of the MIT-BIH polysomnographic database [120] on Physionet [121]. The ECG data was sampled at 250 Hz. At the 300. s of the recording we selected a 160 s long segment to be analyzed. The embedding parameters were set by a manual procedure to  $E_{\text{TOF}} = 3$  and  $\tau = 0.02$  s. The embedding delay was set according to the first zero-crossing of the autocorrelation function, embedding dimension was determined by an iterative embedding process, where the intrinsic dimensionality [69] of the dataset was measured for various embedding dimensions (Fig 6). The embedding dimension where the intrinsic dimensionality started to saturate was selected. For LOF, the embedding dimension was set higher ( $E_{\text{LOF}} = 7$ ), because the results became more informative about the apnoe event. The neighborhood size was set according to simulation results; we used a smaller neighborhood for TOF ( $k = 11$ ) and a large neighborhood for LOF ( $k = 200$ ). Moreover we set the event length to  $M = 5$  s for TOF, corresponding to 3.125% for LOF, which turned out to be a too loose condition. Therefore we used the more conservative 0.5% threshold for LOF to get more informative results.

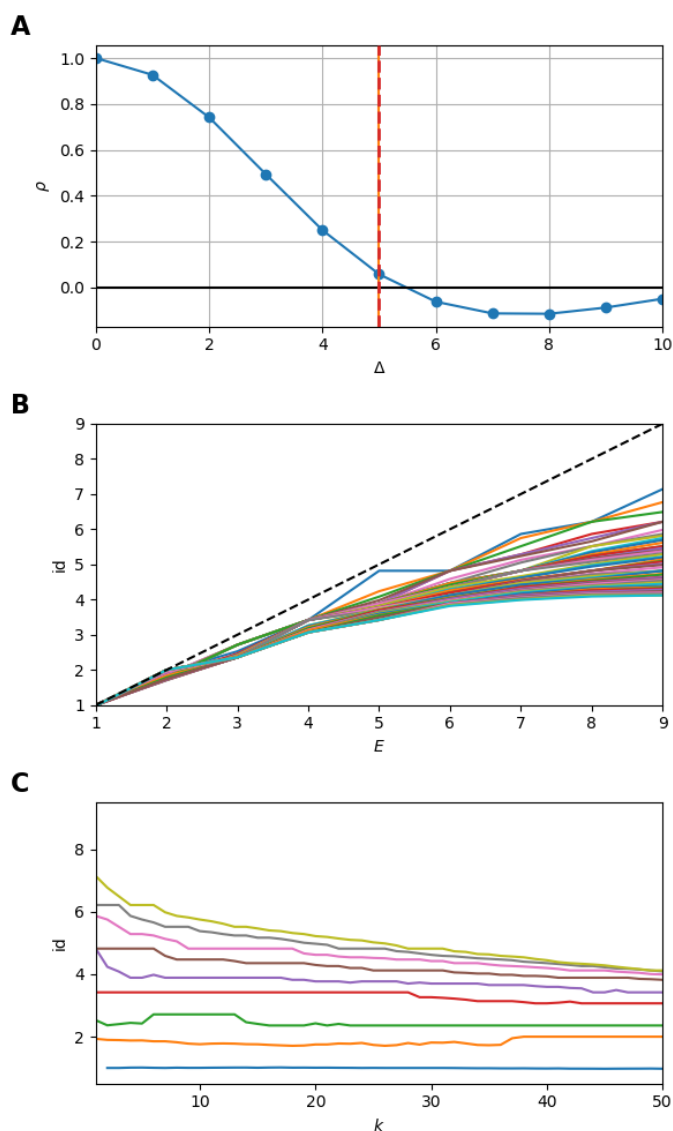


Figure 6: **Embedding parameter selection for the polysomnography data.** **a** Embedding delay was selected ( $\tau = 5$  sampling period) according to the first zero-crossing of the autocorrelation function. The time-shift ensures the most linearly independent axes in reconstructed state-space. **b** The intrinsic dimensionality is measured in the function of embedding dimension ( $E$ ) for various neighborhood sizes. The dimension-estimates start to deviate from the diagonal at  $E = 3$ . **c** Intrinsic dimensionality in the function of neighborhood size ( $k$ ) for various embedding dimensions.

**Gravitational wave dataset.** We analyzed the 4096 Hz sampling rate strain data of the LIGO Hanford (H1) detector around the GW150914 merger event. The analysed 12 s recording starts 10 s before the event. We investigated the q transform spectrogram of the time series around the event at  $5 \times 10^{-4}$  s time resolution by using the gwpy python package (<https://doi.org/10.5281/zenodo.3598469>). Based on the spectrogram we applied 50-300 Hz band-pass filtering on the time series as a preprocessing step. Embedding parameters

were selected manually (Fig. 7), by choosing the first minima of the autocorrelation function for the embedding delay ( $\tau = 8$  sampling periods  $\approx 1.95$  ms) and then we selected the embedding dimension according to a manual procedure. Successive embedding of the time series into higher and higher dimensional space showed, that the intrinsic dimensionality of the dataset starts to deviate from the embedding dimension at  $E = 6$ . Thus, we set this latter value as embedding dimension for TOF. For LOF a higher embedding dimension ( $E = 11$ ) led to informative results. We set the neighborhood sizes based on our experiences with the simulated data-sets: smaller value was set for TOF ( $k = 12$ ) and larger for LOF ( $k = 100$ ). The event length was set to  $M = 146$  ms for TOF as the visible length of the chirp on the spectrogram and 0.5 % for LOF. Also, a  $w = 7$  widening window was applied on the TOF detections.

**LIBOR dataset.** The monthly LIBOR dataset was analyzed to identify interesting periods. As a preprocessing step, the first difference was applied for detrending purposes.

Optimal Embedding parameters were selected according to the minima of the relative entropy ( $E = 3$ ,  $\tau = 1$  month, Fig. 8-9). The neighborhood size was set manually to  $k_{\text{TOF}} = 5$  and  $k_{\text{LOF}} = 30$  for TOF and LOF respectively. Also, the event length was  $M = 30$  for TOF and the threshold was set to 18.86 % for LOF. Also, a widening window  $w = 3$  was applied on the TOF detections.

### 3.3 Simulations and FSA dimension-analysis details

The simulations and the FSA algorithms were implemented in python3 [122] using the numpy [123], scipy [117] and matplotlib [124] packages, unless otherwise stated.

#### 3.3.1 Simulations

We generated test-datasets by uniform random sampling from the unit  $D$ -cube to demonstrate, that theoretical derivations fit to data. We measured distances with a circular boundary condition to avoid edge effects, hence the data is as close to the theoretical assumptions as possible.

To illustrate the probability density function of the FSA estimator, we computed the local FSA intrinsic dimension values (Fig. 20). We generated  $d$ -hypercubes ( $n = 10000$ , one realization) with dimensions of 2, 3, 5, 8, 10 and 12, then computed histograms of local FSA estimates for three neighborhood sizes:  $k = 1, 11, 50$  respectively (Fig. 20 A-F). We drew the theoretically computed pdf to illustrate the fit.

To show that the theoretically computed sampling distribution of the mFSA fits to the hypercube datasets, we varied the sample size ( $n = 11, 101, 1001$ ) with  $N = 5000$

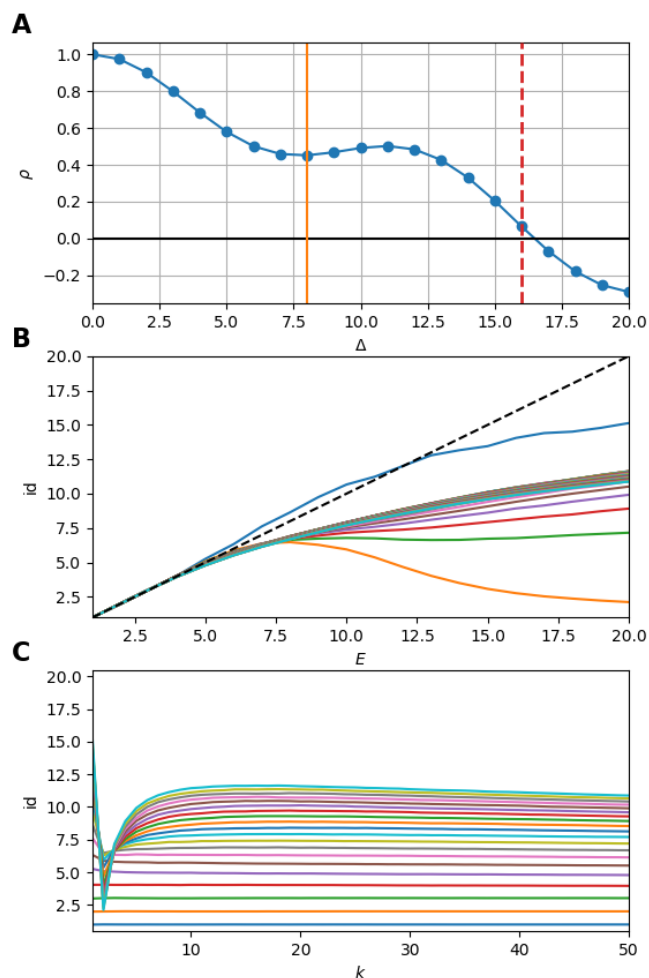


Figure 7: **Embedding parameter selection for the gravitational wave data.** **a** Embedding delay was selected ( $\tau = 8$  sampling period) according to the first minima of the autocorrelation function. The first zero point was between 16 and 17 sampling periods. **b** The intrinsic dimensionality is measured in the function of embedding dimension ( $E$ ) for various neighborhood sizes. The dimension estimates start to deviate from the diagonal at  $E = 5$ . **c** Intrinsic dimensionality in the function of neighborhood size ( $k$ ) for various embedding dimensions.

realizations from each. We computed the mFSA for each realization and plotted the results for  $d = 2$  (Fig. 21 A) and  $d = 5$  (Fig. 21 B).

We investigated the dimensionality and sample-size effects on mFSA estimates (Fig. 22 A-F). We simulated the hypercube data in the 2-30 dimension-range, and applied various sample sizes:  $n = 10, 100, 1000, 2500, 10000$ ; one hundred realizations each ( $N = 100$ ). We computed the mFSA values with minimal neighborhood size ( $k = 1$ ), and observed

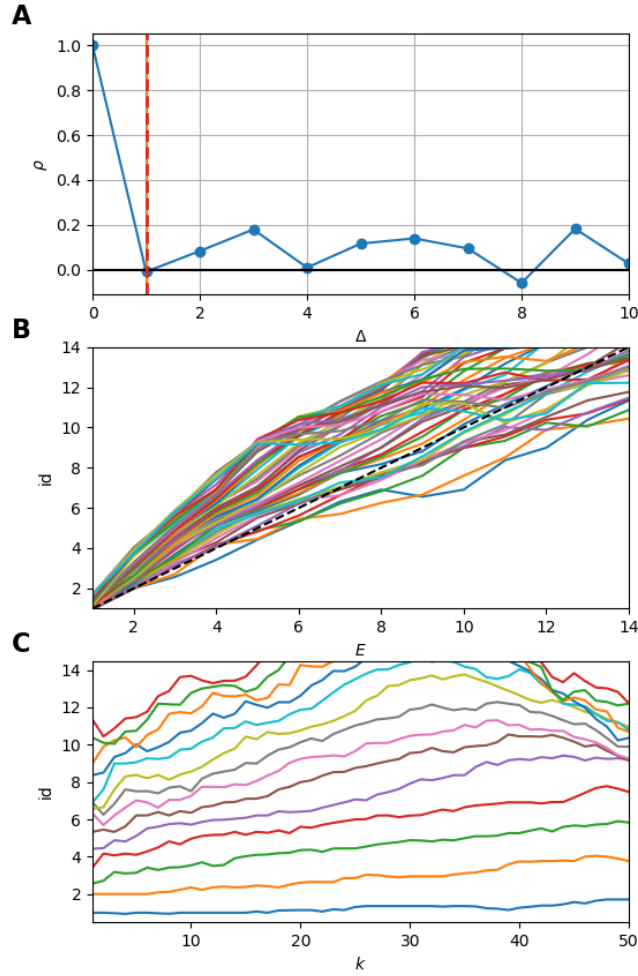


Figure 8: **Autocorrelation and intrinsic dimension measurement of the preprocessed LIBOR time series.**

finite-sample-effects, and asymptotic convergence. The finite sample effect was pronounced at low sample sizes and high dimensions, but we experienced convergence to the real dimension value as we increased sample size. We repeated the analysis with hard boundary conditions.

We fitted a correction formula on the logarithm of dimension values and estimates with the least squares method (Eq. 48), using all 100 realizations for each sample sizes separately.

$$\alpha = \frac{\sum (\ln E_i) d^{(i)}}{\sum (d^{(i)})^2} \quad (48)$$

Where  $E_i = D_i/d^{(i)}$  is the relative error,  $D_i$  is the intrinsic dimension of the data, and

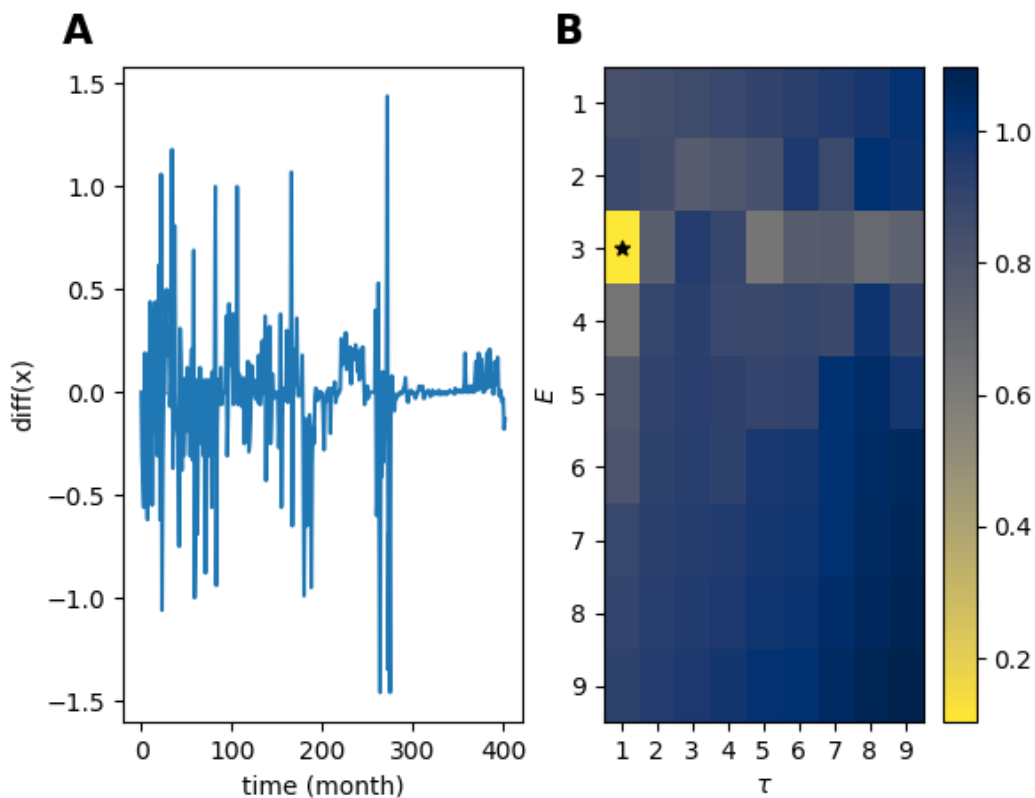


Figure 9: **Preprocessing and embedding parameter selection for the LIBOR time series with differential entropy.** (left) The simple difference of the original time series were taken to detrend the data (right) The minima of the entropy landscape marks the optimal embedding parameters ( $E = 3, \tau = 1$  time-step).

$d^{(i)}$  are the corresponding mFSA estimates. This procedure fit well to data in the intrinsic dimension range 2-30 (Fig. 24 A-F).

Wider range of intrinsic dimension values (2-80) required more coefficients in the polynomial fit procedure (Fig. 26 A). Also, we used orthogonal distance regression to fit the mean over realizations of  $\ln E_i$  with the same  $D_i$  value (Fig. 26 B). We utilized the mean and standard deviation of the regression error to compute the error rate of cmFSA estimator, if the error-distributions are normal (Fig. 26 C-D). We applied this calibration procedure ( $n = 2500$ ) to compute cmFSA on the following benchmark datasets.

### 3.3.2 Comparison on synthetic benchmark datasets

We simulated  $N = 100$  instances of 15 manifolds ( $M_i, n = 2500$ ) with various intrinsic dimensions (see Table 1, 2, 4 in Campadelli et al. [55], <http://www.mL.uni-saarland.de/code/Int-Dim/IntDim.htm>).

We measured the performance of the mFSA and corrected-mFSA estimators on the

benchmark datasets, and compared them with the performance of ML [56] and DANCo [61] estimators. We used the matlab [125, 126](<https://github.com/cran/intrinsicDimension>) and an R package [64] implementation of DANCo.

To quantify the performance we adopted the Mean Percentage Error (MPE, Eq.49) metric [55]:

$$\text{MPE} = \frac{100}{MN} \sum_{j=1}^M \sum_{i=1}^N \frac{|D_j - \hat{d}_{ij}|}{D_j} \quad (49)$$

Where there is  $N$  realizations of  $M$  types of manifolds,  $d_j$  are the true dimension values,  $\hat{d}_{ij}$  are the dimension estimates.

Also, we used the error rate – the fraction of cases, when the estimator did not find (missed) the true dimensionality – as an alternative metric.

We found that the corrected-mFSA estimator produced the second smallest MPE and the smallest error rate on the test datasets (Fig. 25).

### 3.3.3 Dimension estimation of interictal and epileptic dynamics

We used data of intracranial field potentials from two subdural grids positioned – parietofrontally and frontobasally – on the brain surface and from three strips located in the left and the right hippocampus and in the right temporal cortex as part of presurgical protocol for a subject with drug resistant epilepsy. This equipment recorded extracellular field potentials at 88 neural channels at a sampling rate of 2048 Hz. Moreover, we read in – using the neo package [127]– selected 10 second long chunks of the recordings from interictal periods ( $N = 16$ ) and seizures ( $N = 18$ ) to further analysis.

We standardized the data series and computed the Current Source Density (CSD) as the second spatial derivative of the recorded potential. We rescaled the 10 second long signal chunks by subtracting the mean and dividing by the standard deviation. Then, we computed the CSD of the signals by applying the graph Laplacian operator on the time-series. The Laplacian contains information about the topology of the electrode grids, to encode this topology, we used von Neumann neighborhood in the adjacency matrix. After CSD computation, we bandpass-filtered the CSD signals [128] (1-30 Hz, fourth order Butterworth filter) to improve signal to noise ratio.

We embedded CSD signals and subsampled the embedded time series. We used an iterative manual procedure to optimize embedding parameters (Fig. 10). Since the fastest oscillation is (30 Hz) in the signals, a fixed value with one fourth period ( $2048/120 \approx 17$  samples) were used as embedding delay. We inspected the average space-time separation plots of CSD signals to determine a proper subsampling, (with embedding dimension of  $D=2$  (Fig. 27 A). We found, that the first local maximum of the space-time separation was at around 5 ms: 9 – 10, 10 – 11, 11 – 12 samples for the 1%, 25%, 50% percentile contour-

curves respectively. Therefore, we divided the embedded time series into 10 subsets to ensure the required subsampling. Then, we embedded the CSD signal up to  $D = 12$  and measured the intrinsic dimensionality for each embeddings (Fig. 27 B C). We found that intrinsic dimension estimates started to show saturation at  $D \geq 3$ , therefore we chose  $D = 7$  as a sufficiently high embedding dimension (averaged over  $k = 10 - 20$  neighborhood sizes).

We measured the intrinsic dimensionality of the embedded CSD signals using the mFSA method during interictal and epileptic episodes (Fig. 27). We selected the neighborhood size between  $k = 10$  and  $k = 20$  and averaged the resulting estimates over the neighborhoods and subsampling realizations. We investigated the dimension values (Fig. 27 A B) and differences (Fig. 27 C) in interictal and in epileptic periods.

We found characteristic changes in the pattern of intrinsic dimensions during seizures, which may help to localize seizure onset zone.

## 3.4 Causality analysis between LFP and IOS

### 3.4.1 Experimental procedures

Experiments were performed on adult, male Wistar rats weighing 100-200 g (Toxicoop, Budapest, Hungary). Experimental design conformed to the rules of European Communities Council Directive of 24 November 1986 (86/609/EEC), and the study was approved by the Animal Care and Use Committee of Eötvös Loránd University and Budapest Animal Health Care Authority (p.n.: 22.1/829/003/2007). Efforts were made to minimize the number of animals used. Rats were kept under a 12:12 h LD cycle (lights on at 8:00 a.m.) in a temperature-controlled room at  $22 \pm 2$  °C. Standard food-pellets and tap water were available ad libitum.

**Slice preparation.** In vitro experiments were performed on rat cortical slices (13 slices from 13 rats) using standard procedures. Animals were decapitated in deep chloral-hydrate (Hunгарopharma, Budapest, Hungary) anesthesia and the brain was quickly removed from the skull. A block was dissected from the somatosensory cortex and 400  $\mu\text{m}$  thick coronal slices were prepared with a vibratome (EMS-4000, Electron Microscopy Sciences, Fort Washington, PA, USA) in ice-cold artificial cerebrospinal fluid (ACSF). Slices were incubated at room temperature for an hour in oxygenated ACSF (pH 7.01-7.12), the composition of which was (in mM): 126  $\text{NaCl}$ ; 1.8  $\text{KCl}$ ; 1.25  $\text{KH}_2\text{PO}_4$ ; 1.3  $\text{MgSO}_4$ ; 26  $\text{NaHCO}_3$ ; 2.4  $\text{CaCl}_2$ ; and 10 glucose.

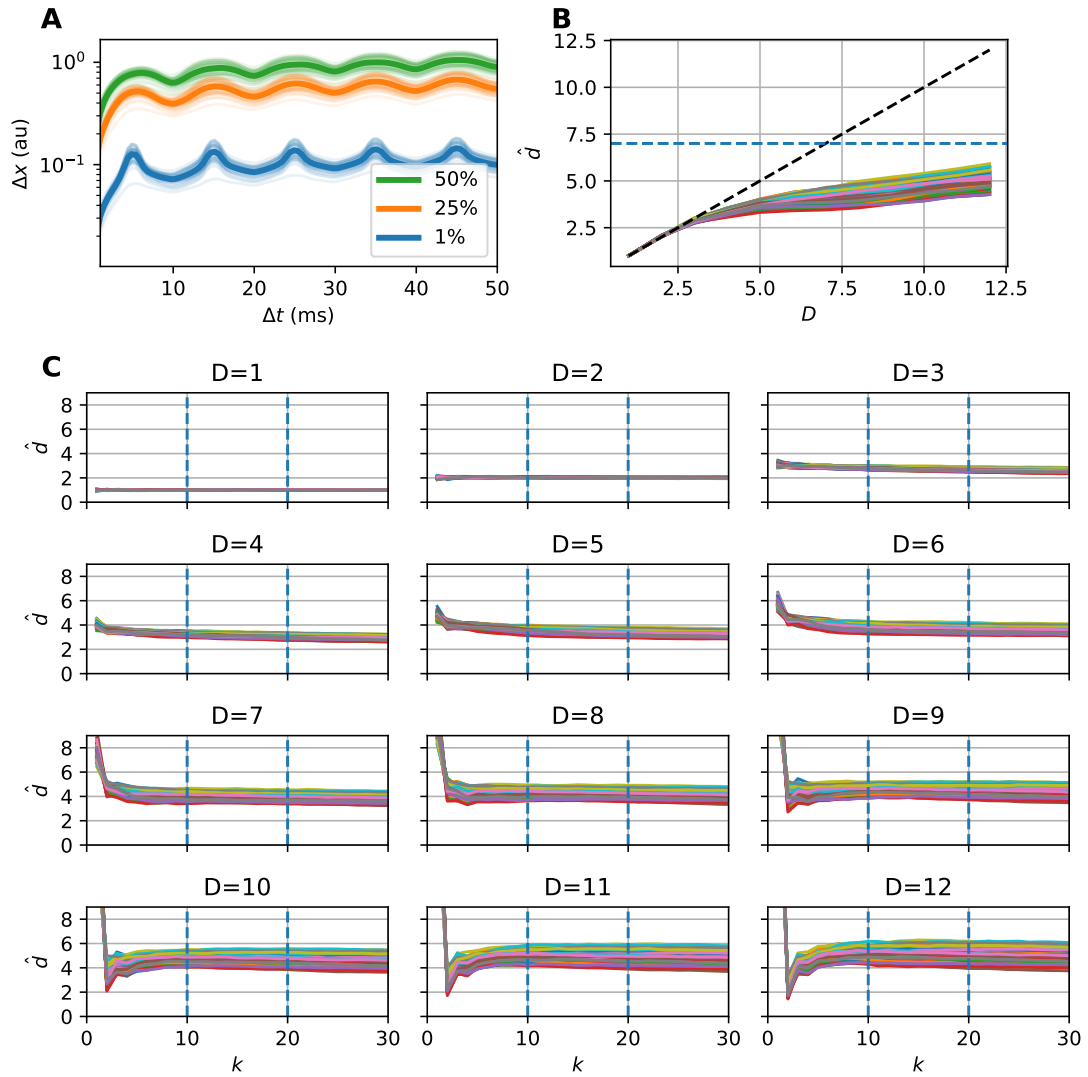


Figure 10: **Subsampling and embedding of the CSD signals.** **A** Mean space-time separation plot of the CSD recordings, the lines show the contours of the 1% (blue), 25% (orange), and 50% (green) percentiles for the 34 - 16 interictal and 18 seizures - recordings (thin lines) and their average (thick line,  $D = 2$ ). The first local maximum is at around 5 ms (10 time steps), which appoints the proper subsampling to avoid the effect of temporal correlations during the dimension estimation. **B** Intrinsic dimension in the function of the embedding dimension for the 88 recording-channels (averaged between  $k = 5 - 10$ , for the first seizure). Dimension-estimates deviate from the diagonal above  $D = 3$ , thus we chose  $D = 2 * 3 + 1 = 7$  as embedding dimension. **C** Intrinsic dimension in the function of neighborhood size for various embedding dimensions (88 channels, for the first seizure). The dimension estimates are settled at the neighborhood size between  $k=10 - 20$  (dashed blue). The knee because of the autocorrelation becomes pronounced for  $D \geq 8$ .

**Induction and recording of seizure activity – interface conditions.** A single slice was placed into an interface-type recording chamber, which was perfused continuously (3 ml/min) with ACSF. In the recording chamber, slices were maintained at  $32 \pm 0.5$  °C in humidified, carbogenated (95% $O_2$ , 5% $CO_2$ ) gas atmosphere. A total number of 12 recording sites in 12 slices were included in the final analysis. To test the change in the LFP, glass extracellular electrode (5 – 10  $M\Omega$ ) filled with 1 M NaCl was positioned into layer 3 of the somatosensory cortex. For stimulation a bipolar tungsten electrode was placed at the border of the white and gray matter below the recording electrode (Fig 28). Electrophysiological signals were amplified by an Axoclamp 2B amplifier (Axon Instruments Inc., Union City, CA), filtered and further amplified (0.16 – 1000 Hz, 1000x) by a Supertech Signal Conditioner (Supertech Ltd., Pécs, Hungary) and digitized by an NI-6023E A/D card (National Instruments, Austin, Texas) for off-line analysis. Intrinsic optical signals (IOS) were recorded also from the beginning of treatment with convulsant solution, simultaneously with local field potential (LFP). The slice was illuminated with unfiltered white light, using a voltage-stabilized cold light source (Fiber-Lite MI-150, Dolan-Jenner, Boxborough, UK). Alteration of reflected light was recorded by a monochrome 12-bit CCD camera (FOculus FO-432B, NET GmbH, Lerchenberg, Germany) attached to an upright 3-way Olympus SZX-9 (Olympus, Tokyo, Japan) stereomicroscope. Digital images were taken at a resolution of 1024x768 pixels at 2 fps sampling rate, and stored in uncompressed format on an x86 based personal computer for off-line analysis. Epileptiform discharges were provoked either by high frequency electric stimulation or by convulsant application into the perfusion solution. Evoked seizures developed as afterdischarges, which immediately followed the high frequency electric stimulation (50 Hz, 5 s). Spontaneous epileptiform activity developed after exchanging the perfusion solution in the recording chamber from ACSF to  $Mg^{2+}$ -free- or 4-aminopyridine (4-AP, 50  $\mu M$ ) containing solution. These types of activity usually appeared in 10-25 min in following the perfusion of the convulsant.

Data acquisition of IOS and LFP was made simultaneously by a custom Matlab (The MathWorks Inc., Natick, MA, USA) based software, which made snapshots of continuous video signal from the CCD camera at a pre-defined sampling rate, based on the timing process of NI-6023E A/D card. For the analysis of the optical changes a region of interests (ROI) was manually defined in the slice beside the site of electrophysiological recording, optical alterations in a small box was determined (Fig. 28).

**Recording of seizure activity – submerged conditions.** Under submerged conditions the recording of LFP was carried on a MEA USB-1060 INV (Multichannel Systems, Reutlingen, Germany) system. Slices were transferred to a 60 channel 200/30 3D multielec-

trode array (MEA) chip (Qwane Biosciences, Lausanne, Switzerland), where 30  $\mu\text{m}$  diameter electrodes are positioned in a 8x8 grid of 200  $\mu\text{m}$  distances. The slice is positioned directly on the bottom of MEA chip using a net, electrodes with the height of 50-70  $\mu\text{m}$  penetrate into the lower surface of slice. Continuous ACSF perfusion was carried out at a 5-6 ml/min rate, temperature is maintained at  $33\pm 1$   $^{\circ}\text{C}$  using TC02 Temperature Controller (Multichannel Systems, Reutlingen, Germany) with PH01 perfusion heater (Multichannel Systems, Reutlingen, Germany) and the built-in heating pad of MEA 1060 Amplifier (Multichannel Systems, Reutlingen, Germany). The slice was trans illuminated with unfiltered white light, using a Rebel Star LED (Ledium Ltd, Szeged, Hungary) light source, placed under the MEA chip. Alteration of transmitted light was recorded by a 10-bit CCD camera (Qimaging Micropublisher 3.3, Qimaging, Surrey, Canada) attached to an upright 3-way Nikon SMZ 800 (Nikon Instruments Europe BV, Amsterdam, Netherlands) stereomicroscope. Digital images were taken at a resolution of 1024x768 pixels at 1 fps sampling rate, and stored in uncompressed format on an x86 based personal computer for off-line analysis. Data acquisition of IOS and LFP was also made simultaneously in the case of submerged slice experiments. The STG4002 stimulator (Multichannel Systems, Reutlingen, Germany) provided continuous triggering for a custom Matlab (The MathWorks Inc., Natick, MA, USA) based framegrabber software during data acquisition made by MEA 1060 amplifier. Epileptic activity was provoked by  $Mg^{2+}$ -free perfusion solution application.

**The intrinsic optical signals.** Image series of interface and submerged slice experiments were analyzed with the same method, using a custom Mathworks Matlab based software. Since the first 2-3 min of video data acquisition was made in normal ACSF, the first 10 frames of each image series were averaged and served as control  $F_{cont}$ , and then it was subtracted from each subsequent images according to the following formula:

$$IOS = \frac{\Delta F_t}{F_{cont}} \cdot 100 = \frac{F_t - F_{cont}}{F_{cont}} \cdot 100 \quad (50)$$

where  $F_{cont}$  is the luminance of control image (the average of first 10 frames) at a given pixel,  $F_t$  is the luminance of each subsequent experimental image,  $\Delta F$  is the change of reflectance or transmittance, depending on experimental conditions.  $F_{cont}$  in the denominator serves to normalize the data across regions differing in luminance. The images were converted to 256-scale pseudocolour images for further off-line analysis. For causality analysis a region of interests (ROI) was defined in the somatosensory cortical region of the slice around the site of electrophysiological recording. The mean IOS value was calculated for the ROI. This data was used to characterize the IOS changes of the slice during 1 h seizure induction and correlate with single-channel field potential recordings.

## 4 Results

### 4.1 Detecting clusters in slices of retinal cell pedicles

To obtain more information on the variability of subpedicle Cx36 conglomerates we determined pedicle area sizes ( $n = 379$ ), subpedicle Cx36 convex hull area sizes ( $n = 379$ ) and the number of Cx36 plaques in subpedicle conglomerates. The probability density distributions of all three measures showed the marks of multimodality. Thus, we performed a mathematical model selection process to determine the optimal number of components of the observed distributions (see Methods). Since the Gaussian distribution can take both positive and negative values, but all three examined measures here (pedicle area, convex hull area and number of Cx36 plaques/pedicle) are restricted to positive values by definition, we chose lognormal distributions to describe the form of each component.

The selection process resulted in two components (minimum BIC value occurred at 2 log-normal components) for the optimal model of the pedicle area distribution. This suggested the presence of two pedicle populations, including a less frequent population with smaller area sizes of  $42.848\mu\text{m}^2$  ( $\pm 18.479\mu\text{m}^2$  SD) and a more numerous one with area sizes of  $54.802\mu\text{m}^2$  ( $\pm 10.804\mu\text{m}^2$  SD; Fig. 11 A). Interestingly, a three components solution was the optimal choice when convex hull area size values were analyzed. The modes were at  $0.166\mu\text{m}^2$  ( $\pm 1.226\mu\text{m}^2$  SD),  $19.62\mu\text{m}^2$  ( $\pm 15.667\mu\text{m}^2$  SD) and  $31.678\mu\text{m}^2$  ( $\pm 5.811\mu\text{m}^2$  SD). However, the first component was confined to small values that most likely corresponded to convex hull fragments, and the majority of the distribution was well described by two components (Fig. 11 B). Thus, we concluded that two populations of subpedicle Cx36 conglomerates existed. Similarly, the optimal choice for the number of Cx36 plaques/pedicle dataset occurred for the three-components calculation with modes at 1.731 ( $\pm 2.065$  SD), 9.048 ( $\pm 4.242$  SD) and 17.455 ( $\pm 4.374$  SD) (Fig. 11 C). Again, the first component was too small and likely corresponded to conglomerate fragments. This latter analysis further supported the existence of two Cx36 conglomerate populations.

### 4.2 An algorithm to detect unique events in time series

#### 4.2.1 Temporal Outlier Factor

We present a new model-free unsupervised anomaly detection algorithm to detect unicorns (unique events), that builds on nonlinear time series analysis techniques, such as time delay embedding [15] and upgrades time-recurrence based non-stationarity detection methods [39] by defining a local measure of uniqueness for each point.

The key question in unicorn search is how to measure the uniqueness of a state, as this

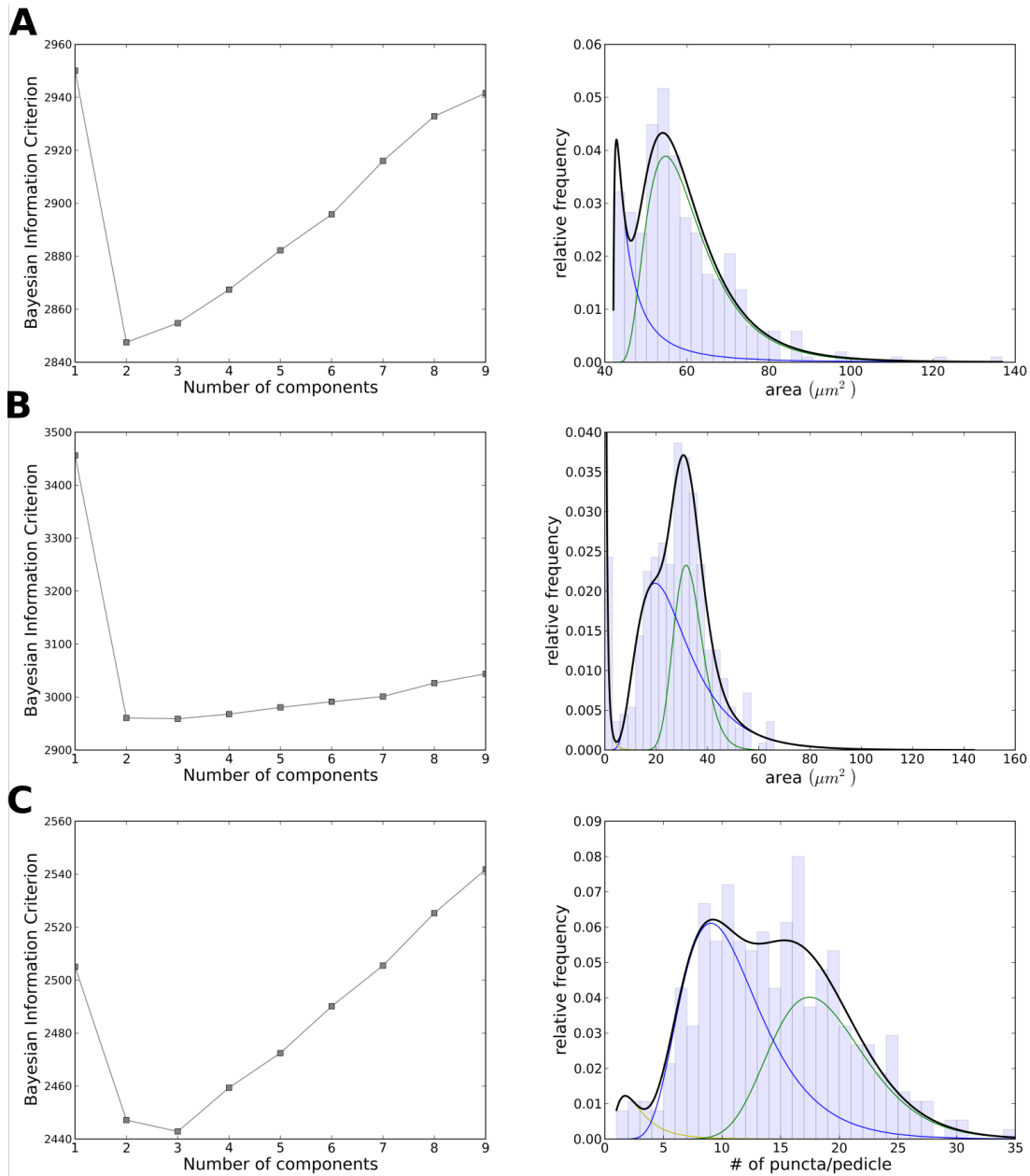


Figure 11: Clusterings of retinal gap junction based on morphological features

is the only attribute of a unique event. The simplest possible definition would be, that a unique state is one visited only once in the time series. A problem with this definition arises in the case of continuous valued observations, where almost every state is visited only once. Thus, a different strategy should be applied to find the unicorns. Our approach is based on measuring the temporal dispersion of the state-space neighbors. If state space neighbors are separated by large time intervals, then the system returned to the same state time-to-time. In contrast, if all the state space neighbors are temporal neighbors as well, then the system never returned to that state again. This concept is shown on an example

ECG data series from a patient with Wolff-Parkinson-White (WPW) Syndrome (Fig. 3). The WPW syndrome is due to an aberrant atrio-ventricular connection in the heart. Its diagnostic signs are shortened PR-interval and appearance of the delta wave, a slurred upstroke of the QRS complex. However, for our representational purpose, we have chosen a data segment, which contained one strange T-wave with uniquely high amplitude (Fig. 3 a).

To quantify the uniqueness on a given time series, the Temporal Outlier Factor (TOF) is calculated in the following steps (Fig. 4):

Firstly, we reconstruct the system's state by time delay embedding (Eq. 5), resulting in a manifold, topologically equivalent to the attractor of the system (Fig. 3 c-d and Fig. 4 b).

Secondly, we search for the kNNs in the state space at each time instance on the attractor. Two examples are shown on Fig. 3 c: a red and a blue diamond and their 6 nearest neighbors marked by orange and green diamonds respectively.

Thirdly, the Temporal Outlier Factor ( $TOF$ ) is computed from the time indices of the kNN points (Fig. 4 c):

$$TOF(t) = \sqrt[q]{\frac{\sum_{i=1}^k |t - t_i|^q}{k}}. \quad (51)$$

Where  $t$  is the time index of the sample point ( $X(t)$ ) and  $t_i$  is the time index of the  $i$ -th nearest neighbor in reconstructed state-space. Where  $q \in \mathcal{R}^+$ , in our case we use  $q = 2$  (Fig. 3 e).

As a final step for identifying unicorns, a proper threshold  $\theta$  should be defined for TOF (Fig. 3 e, dashed red line), to mark unique events (orange dots, Fig. 3 f).

TOF measures an expected temporal distance of the kNN neighbors in reconstructed state-space (Eq. 51) and has time dimension. A high or medium value of TOF implies that neighboring points in state-space were not close in time, therefore the investigated part of state-space was visited on several different occasions by the system. In our example, green diamonds on (Fig. 3 c) mark states which were the closest points to the blue diamond in the state space, but were evenly distributed in time, on Fig. 3 a. Thus the state marked by the blue diamond was not a unique state, the system returned there several times.

However a small value of TOF implies that neighboring points in state-space were also close in time, therefore this part of the space was visited only once by the system. On Fig. 3 c and d orange diamonds mark the closest states to the red diamond and they are also close to the red diamond in time, on the (Fig. 3 b). This results in low value of TOF in the state marked by the red diamond and means that it was a unique state never visited again. Thus, small TOF values feature the uniqueness of sample points in state-space, and can be interpreted as an outlier factor. Correspondingly, TOF values exhibit a clear breakdown

at time interval of the anomalous T-wave (Fig. 3 f).

The number of neighbors ( $k$ ) used during the estimation procedure sets the possible minimal TOF value:

$$\text{TOF}_{\min} = \sqrt{\frac{\sum_{i=-\lfloor k/2 \rfloor}^{\lfloor k/2 \rfloor + k \bmod 2} i^2}{k}} \Delta t, \quad (52)$$

Where  $\lfloor k/2 \rfloor$  is the integer part of  $k/2$ ,  $\bmod$  is the modulo operator and  $\Delta t$  is the sampling period.

The approximate possible maximum of TOF is determined by the length ( $T$ ) and neighborhood size ( $k$ ) of the embedded time series:

$$\text{TOF}_{\max} = \sqrt{\frac{\sum_{i=0}^{k-1} (T - i\Delta t)^2}{k}} \quad (53)$$

TOF shows a time-dependent mean baseline and variance (Fig. 3 e, Fig. 13) which can be computed if the time indices of the nearest points are evenly distributed along the whole time series. The approximate mean baseline is a square-root-quadratic expression, it has the lowest value in the middle and highest value at the edges (Fig. 13-14):

$$\sqrt{\langle \text{TOF}_{\text{noise}}^2(t) \rangle} = \sqrt{t^2 - tT + \frac{T^2}{3}} \quad (54)$$

$$\text{VAR}(\text{TOF}_{\text{noise}}^2(t)) = \frac{1}{k} \left( \frac{t^5 + (T-t)^5}{5T} - \left( t^2 - tT + \frac{T^2}{3} \right)^2 \right) \quad (55)$$

Based on the above considerations, imposing a threshold  $\theta$  on  $\text{TOF}_k$  has a straightforward meaning: it sets a maximum detectable event length ( $M$ ) or vice versa:

$$\theta = \sqrt{\frac{\sum_{i=0}^{k-1} (M - i\Delta t)^2}{k}} \quad \Bigg| \quad k\Delta t \stackrel{!}{\leq} M \quad (56)$$

Where in the continuous limit, the threshold and the event length becomes equivalent:

$$\lim_{\Delta t \rightarrow 0} \theta(M) = M \quad (57)$$

Also, the parameter  $k$  sets a necessary detection-criteria on the minimal length of the detectable events: only events longer than  $k\Delta t$  may be detected. This property comes from the requirement, that there must be at least  $k$  neighbors within the unique dynamic regime of the anomaly.

We compare our method to the standard Local Outlier Factor (LOF) metrics (see Methods). The main purpose of the comparison is not to show that our method is superior to

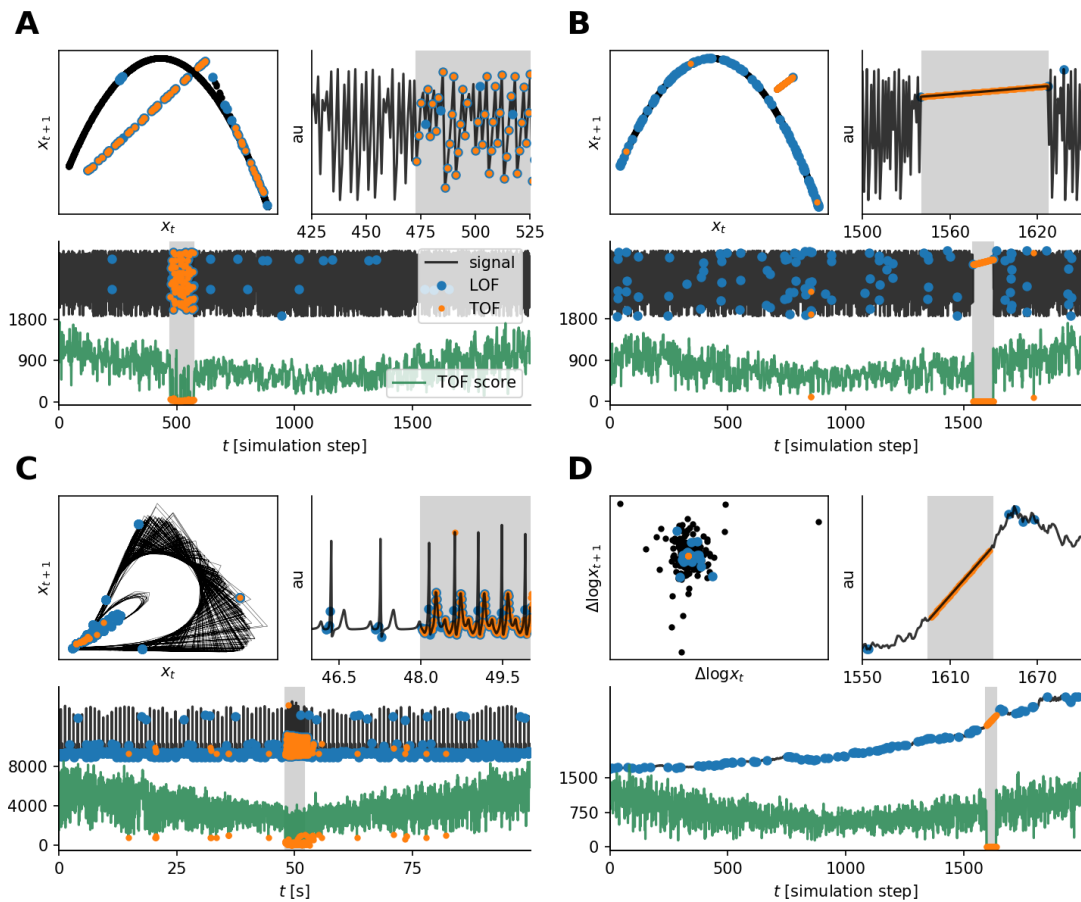


Figure 12: **Simulated time series with anomalies of different kinds.** **a** Logistic map time series with tent-map anomaly. **b** Logistic map time series with linear anomaly. **c** Simulated ECG time series with tachycardia. **d** Random walk time series with linear anomaly, where the TOF was measured on the discrete time derivative ( $\Delta \log x_t$ ). Each subplot shows an example time series of the simulations (black) in arbitrary units and in three forms: Top left the return map, which is the results of the 2D time delay embedding, and defines the dynamics of the system or its the 2D projection. Bottom: Full length of the simulated time series (black) and the corresponding TOF values (green) shaded areas show anomalous sections. Top right: Zoom to the onset of the anomaly. In all graphs outliers detected by TOF and LOF are marked by orange and blue dots respectively. While in **a** and **b** cases the anomalies form clear collective outliers, **d** shows an example where the unique event is clearly not an outlier neither pointwise nor collectively, it is in the centre of the distribution. Both LOF and TOF detected well the anomalies in cases **a** and **c**, but only TOF was able to detect the anomalies in **b** and **d** cases.

the LOF in outlier detection, but to present the fundamental differences between the traditional outlier concept and the unicorns. The difference between the anomaly-concepts are further emphasized by the fact that the first steps of the LOF and TOF algorithms are parallel: The LOF uses time-delay embedding as well as a preprocessing step to define a state-space and it also searches for the kNNs in the state-space for each time instance. As

a key difference, LOF calculates the distance of the actual points in state-space from their nearest neighbors and normalizes it with the mean distance of those nearest neighbors from their nearest neighbors. LOF values around 1 are considered the signs of normal behavior, while higher LOF values mark the outliers. LOF concentrates on the spatial distances in the state-space, while TOF considers the temporal distance of the state-space neighbors (Fig. 3).

#### 4.2.2 Mean and variance for $q = 1$

The mean and the variance of TOF can be computed for uncorrelated noise in the continuous-time limit, where the typical properties of the metrics can be introduced. The expectation of the first neighbor is easy to compute (Eq. 58), if we take the probability density function ( $p(\tau)$ ) as uniform, this is the assumption of white noise. Also, the pdf is independent of the rank of the neighbor ( $k$ ), thus the mean is same for all neighborhood sizes. By the previous assumptions the mean is simply a quadratic expression:

$$\langle TOF_{q=1} \rangle = \int_0^T |t - \tau| p(\tau) d\tau = \frac{1}{T} \int_0^T |t - \tau| d\tau = \frac{t^2}{T} - t + \frac{T}{2} \quad (58)$$

with the method of moments, we calculate the variance for  $k = 1$ :

$$\langle TOF_{q=1}^2 \rangle = \int_0^T (t - \tau)^2 p(\tau) d\tau = \frac{1}{T} \int_0^T (t - \tau)^2 d\tau = t^2 - tT + \frac{T^2}{3} \quad (59)$$

$$\sigma_{q=1}^2 = \langle TOF_{q=1}^2 \rangle - \langle TOF_{q=1} \rangle^2 = -\frac{t^4}{T^2} + \frac{2t^3}{T} - t^2 + \frac{T^2}{12} \quad (60)$$

if we have  $k$  neighbors, then the variance is reduced by a  $1/k$  factor:

$$\sigma_{q=1,k}^2 = \langle TOF_{q=1}^2 \rangle - \langle TOF_{q=1} \rangle^2 = \frac{1}{k} \left( -\frac{t^4}{T^2} + \frac{2t^3}{T} - t^2 + \frac{T^2}{12} \right) \quad (61)$$

To test whether these theoretical arguments fits to data, we simulated random noise time series ( $n = 100, T = 1000$ ) and computed mean TOF score and standard deviation (Fig. 13). We found, that theoretical formulas described perfectly the behavior of TOF.

#### 4.2.3 Mean and variance for $q = 2$

The exact statistics is hard to calculate, when the value of the  $q$  exponent is not equal to one, here we compute a vague approximation for  $q = 2$ . By computing the mean and variance for squared TOF, and taking the square-root of these values can give a feeling

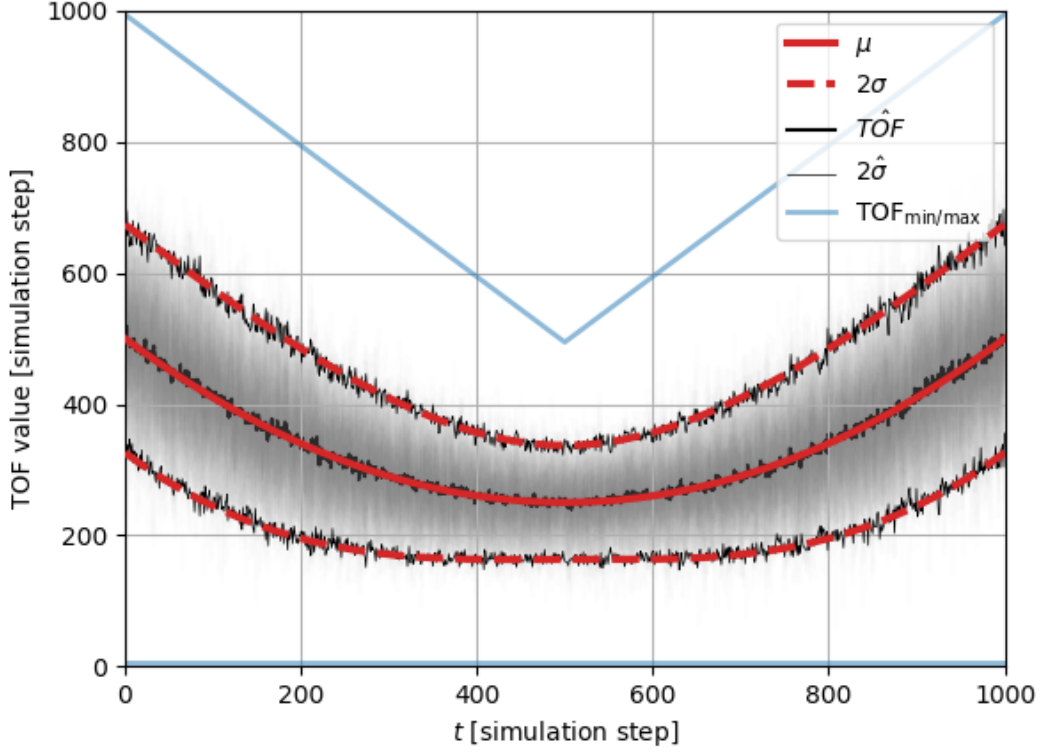


Figure 13: **Properties of TOF for white noise data: theory and simulations.** The expectation of TOF is computed as a function of temporal position in the time series ( $q = 1$ , thick red line), also the standard deviation was calculated (dashed red line). The average (thick black line) and standard deviation (thin black line) of  $n = 100$  instances (grey shading). The minimal and maximal possible TOF vales are also charted (blue lines).

about the properties of  $\text{TOF}_{q=2}$  respectively.

$$\langle \text{TOF}_{\text{noise},q=2}^2 \rangle = \int_0^T (t - \tau)^2 p(\tau) d\tau = \frac{1}{T} \int_0^T (t - \tau)^2 d\tau = t^2 - tT + \frac{T^2}{3} \quad (62)$$

the second moment is as follows:

$$\langle \text{TOF}_{\text{noise},q=2}^4 \rangle = \int_0^T (t - \tau)^4 p(\tau) d\tau = \frac{1}{T} \int_0^T (t - \tau)^4 d\tau = \frac{t^5 + (T-t)^5}{5T} \quad (63)$$

Thus using the method of moments we can get the variance of the  $\text{TOF}_{q=2}^2$ :

$$\text{Var} (\text{TOF}_{\text{noise},q=2}^2) = \frac{t^5 + (T-t)^5}{5T} - \left( t^2 - tT + \frac{T^2}{3} \right)^2 \quad (64)$$

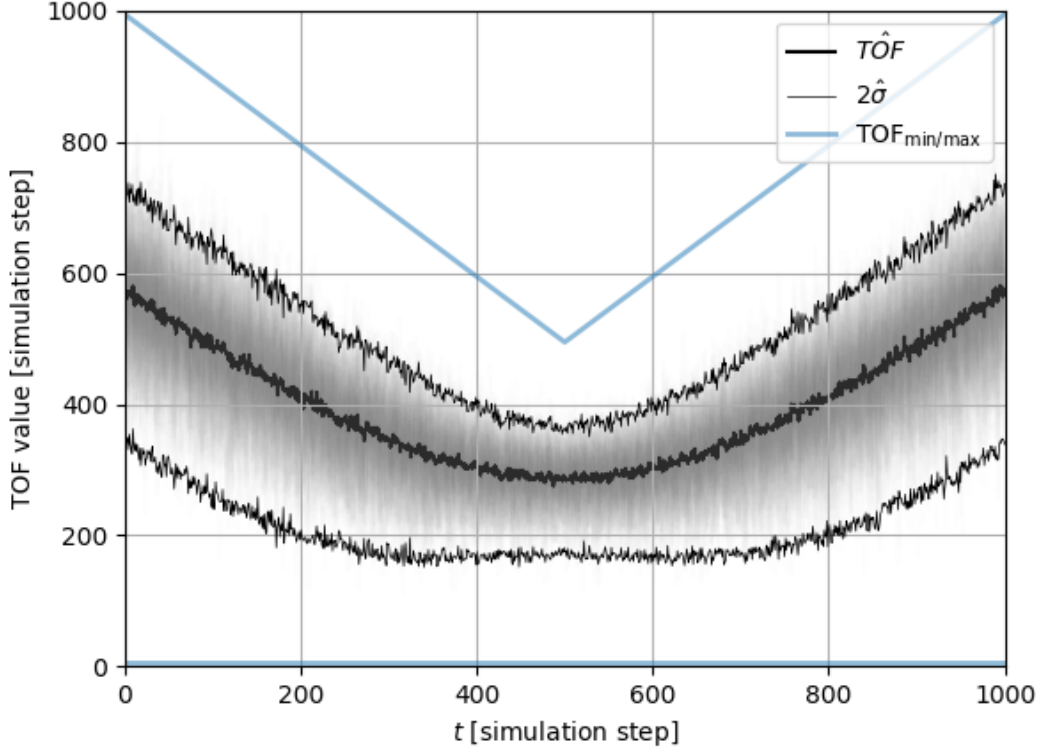


Figure 14: **Properties of TOF for white noise data 2: simulations** The baseline of TOF with  $q = 2$ . The average (thick black line) and standard deviation (thin black line) of  $n = 100$  instances (grey shading).

#### 4.2.4 Evaluation of performance on simulated data series

**Simulated data series with discrete temporal dynamics.** We simulated two datasets with deterministic chaotic discrete-time dynamics generated by a logistic map [12] ( $N = 2000$ , 100 – 100 instances each) and inserted variable-length ( $l = 20 - 200$  step) outlier-segments into the time series at random times (Fig. 12 a-b). Two types of outliers were used in these simulations, the first type was generated from a tent-map dynamics (Fig. 12 a) and the second type was simply a linear segment with low gradient (Fig. 12 b) for simulation details see Methods. The tent map demonstrates the case, where the underlying dynamics is changed for a short interval, but it generates a very similar periodic or chaotic oscillatory activity (depending on the parameters) to the original dynamics. This type of anomaly is hard to distinguish by naked eye. In contrast, a linear outlier is easy to identify for a human observer but not for many traditional outlier detecting algorithms. The linear segment is a collective outlier and all of its points represent a state that was visited only once during the whole data sequence, therefore they are unique events as well.

**Simulated ECG datasets with tachycardia.** As a continuous deterministic dynam-

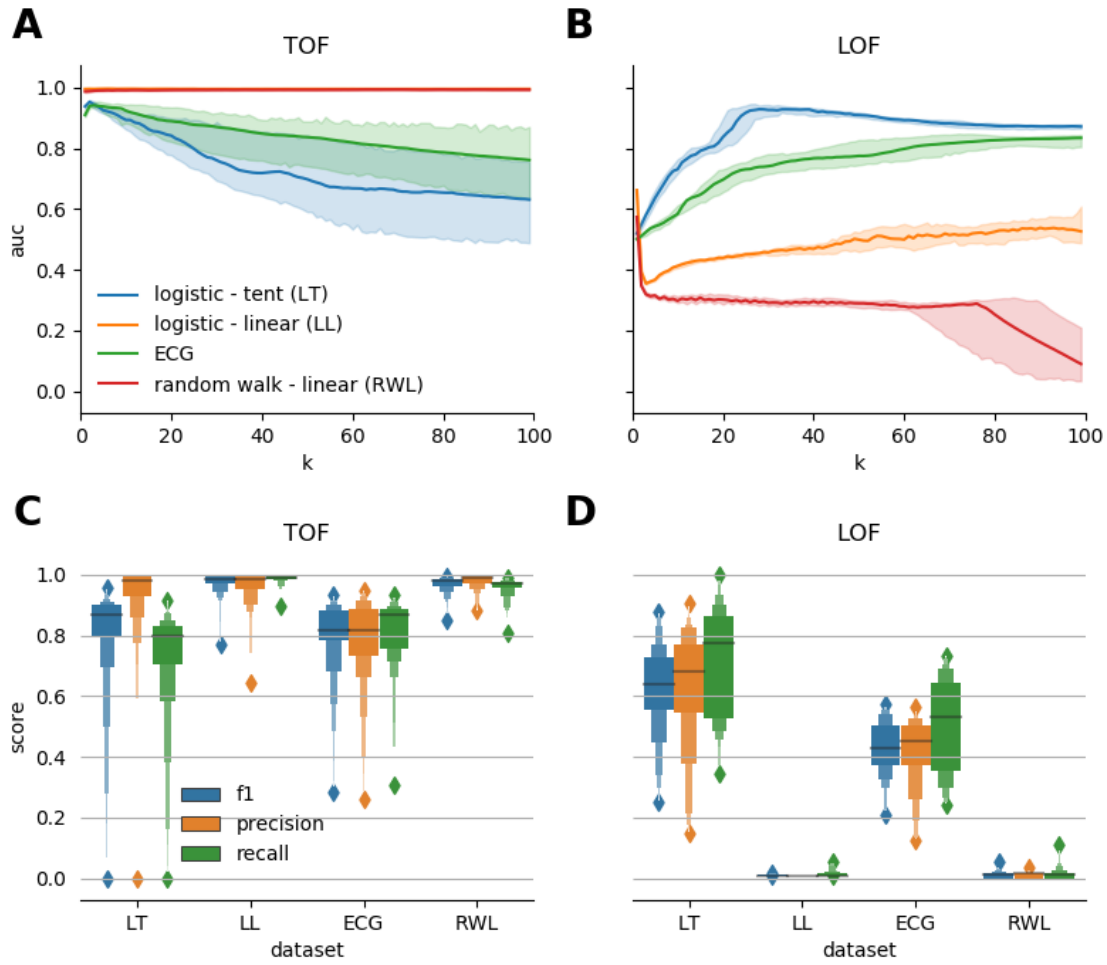


Figure 15: **Performance evaluation of TOF and LOF on simulated datasets.** **a** and **b**: Median ROC AUC score and the median absolute difference for TOF (**a**) and LOF (**b**) are shown in the function of neighborhood size ( $k$ ). TOF showed the best results for small neighborhoods. In contrast, LOF showed better results for larger neighborhoods in the case of logistic map and ECG datasets, but did not reach reasonable performance on linear outliers. **c** TOF: Median  $F_1$  score, precision and recall values showed very good precision scores on all datasets. The recall was very high for the linear anomalies and slightly lower for logistic map - tent map anomaly dataset. **d** LOF: Median  $F_1$  shows very low-valued metrics on datasets with linear anomaly and mediocre values on tent-map anomaly and simulated ECG time series.

ics with realistic features, we simulated electrocorticograms with short tachycardic periods where beating frequency was higher (Fig. 12 c). The simulations were carried out according to the model of Rhythii & Rhythii [118], where the three heart pacemakers and muscle responses were modeled as a system of nonlinear differential equations (see Methods). We generated 100 seconds of ECG and randomly inserted 2 – 20 seconds long faster heart-rate segments, corresponding to tachycardia ( $n = 100$  realizations).

**Deterministic anomaly on stochastic background dynamics.** Takens time delay

Table 1: **Detection performance on simulations in terms of maximal ROC AUC scores and the optimal neighborhood parameter  $k$ .** Maximal median ROC AUC values and the corresponding median absolute difference ranges are shown. LOF detected tent map outliers and tachycardia with reasonable reliability but TOF outperformed LOF for all data series. Linear outliers can not be detected by the LOF method at all, while TOF detected them almost perfectly. TOF reached its maximal performance mostly for low  $k$  values, only random walk with linear outlier required larger neighborhood to compute, while LOF required larger  $k$  for optimal performance on those two data series, on which it worked reasonably.

dataset	TOF		LOF	
	$k$	AUC	$k$	AUC
logmap tent	2	$0.953 \pm 0.027$	28	$0.928 \pm 0.075$
logmap linear	6	$0.996 \pm 0.004$	1	$0.662 \pm 0.016$
sim ECG tachy	3	$0.941 \pm 0.030$	99	$0.834 \pm 0.053$
randwalk linear	70	$0.993 \pm 0.007$	1	$0.573 \pm 0.012$

embedding theorem is valid for time series generated by deterministic dynamical systems, but not for stochastic ones. In spite of this, we investigated the applicability of time delay embedded temporal and spatial outlier detection on stochastic signals with deterministic dynamics as outliers. We established a dataset of multiplicative random walks ( $n = 100$  instances,  $T = 2000$  steps each) with randomly inserted variable length linear outlier segments ( $l = 20 - 200$ , see Methods). As a preprocessing step, to make the random walk data series stationary, we took the log-difference of time series as is usually the case with economic data series. (Fig. 12 d).

**Performance measures and dependency on neighborhood size.** To detect anomalies we applied TOF and LOF on the datasets ( $E = 3$ ,  $\tau = 1$ ) and measured detection-performance by area under receiver operating characteristic curve (ROC AUC),  $F_1$  score, precision and recall metrics. (Fig. 15 and Table 1).  $F_1$  score is especially useful to evaluate detection performance in case of highly unbalanced datasets as in our case.

Fig. 15 a and b show, the performance of the two methods in terms of median ROC AUC for ( $n = 100$ ) realizations and its dependency on the neighborhood size ( $k = 1 - 100$ ) that was used for the calculations.

Two types of behavior were observed among the four experimental setup: First, the linear anomalies were almost perfectly detected by the TOF, with no significant dependency on the  $k$  neighborhood, while LOF was not able to detect these anomalies at all (ROC AUC was close to 0.5) again independently from the  $k$  neighborhood. The second group is formed by the logistic-tent map data series and the simulated ECG with

Table 2: **Performance evaluation by  $F_1$ , precision and recall scores on simulations.** Median scores and median absolute differences are shown. In case of TOF,  $k = 4$  is used, while for LOF, the  $k$  resulted the best ROC AUC were used. TOF is characterized by high precision and recall for all datasets. As a result, very high  $F_1$  scores were reached for all datasets. In comparison, LOF produced mediocre  $F_1$  scores for tent and tachycardia and very low  $F_1$  scores for linear outliers.

dataset	TOF			LOF		
	$F_1$	precision	recall	$F_1$	precision	recall
logmap tent	$0.869 \pm 0.055$	$0.979 \pm 0.031$	$0.797 \pm 0.069$	$0.640 \pm 0.130$	$0.681 \pm 0.158$	$0.777 \pm 0.175$
logmap linear	$0.986 \pm 0.014$	$0.985 \pm 0.022$	$0.991 \pm 0.004$	$0.009 \pm 0.002$	$0.009 \pm 0.000$	$0.009 \pm 0.004$
sim ECG tachy	$0.816 \pm 0.095$	$0.818 \pm 0.129$	$0.868 \pm 0.052$	$0.431 \pm 0.107$	$0.452 \pm 0.079$	$0.533 \pm 0.205$
randwalk linear	$0.980 \pm 0.011$	$0.991 \pm 0.013$	$0.973 \pm 0.009$	$0.014 \pm 0.010$	$0.019 \pm 0.000$	$0.012 \pm 0.013$

tachycardia. Both TOF and LOF resulted in reasonably high ROC AUC values on these anomalies, however with different  $k$  dependency. TOF reached the highest scores for low neighborhoods while LOF required higher  $k$  for its optimal performance. As we compared the achieved ROC AUC scores of the two methods for each cases at their optimal neighborhood size, we can conclude, that TOF slightly outperformed LOF even in this second group of data series as well (Table 1).

To further evaluate the components of the performances and the type of errors of these algorithms,  $F_1$  score, precision and recall were computed for both TOF and LOF (Fig. 15 c, d and Table 2). As the TOF showed best performance with lower  $k$  neighborhood sizes on logmap-tent and simulated ECG-tachycardia values and showed no significant dependency with linear anomalies, the  $F_1$  scores were calculated at a fixed  $k = 4$  neighborhood forming a simplex in the 3 dimensional embedding space [21]. In contrast, as LOF showed stronger dependency on neighborhood size, the optimal neighborhood sizes were used for  $F_1$  score calculations. Finally, thresholds corresponding to  $M = 110$  time-steps and the top 5.5% percentile were used for TOF and LOF respectively, which is the expected simulated anomaly length.

For the linear outlier datasets, TOF performed almost perfectly with high precision and recall, hence with high  $F_1$  score as well. In contrast LOF performed poorly in all these measures. On the logmap-tent dataset TOF showed good  $F_1$  score due to very high precision and slightly lower recall score, while LOF reached a mediocre  $F_1$ -score. On the simulated ECG-tachycardia data series, TOF produced reasonably high precision, recall and  $F_1$  score, while LOF produced low quality measures in all means.

Based on these simulations, we can conclude that there are anomalous events such as tent map logistic background or high frequency tachycardic events, which can be found by both TOF and LOF based methods. However, other types of unique events, such as linear sequences can only be found by TOF methods. Table 3 shows, that the tent map and the tachycardia produce lower density, thus more dispersed points in the state space, presumably making them detectable by the LOF. In contrast, linear segments resulted in similar density of points to the normal logistic activity or higher density of points compared to the random walk background. Detrending via differentiation of the logarithm was applied as a preprocessing step in the latter case, making the data series stationary and drastically increasing the state space density of the anomaly. While LOF counted only the low density sets as outliers, TOF was able to find the unique events independently of their density. To sum it up, TOF has reached better performance to detect anomalies in all the investigated cases.

Table 3: **State space densities and LOF values within normal and anomalous activity.** Median and median absolute difference of the points density and LOF values in the reconstructed state space are shown, calculated from the distance of the 20 nearest neighbors. The density of the anomaly was significantly lower than the density generated by normal activity in two cases: the tent map anomaly in logistic background and the tachycardia within the normal heart rhythm and resulted in higher LOF values of anomalies in these two cases too. While the density of the linear anomaly segments were not significantly different from the logistic background, the linear anomalies generated much higher density than the normal random walk time series after detrending. Correspondingly, LOF values were not significantly higher in these two cases within the anomaly than the normal activity.

dataset	Density		LOF	
	<i>Normal</i>	Anomaly	<i>Normal</i>	Anomaly
logmap tent	95.759 ± 12.070	11.606 ± 1.146	1.039 ± 0.010	3.424 ± 1.990
logmap linear	95.190 ± 9.305	97.413 ± 51.289	1.040 ± 0.012	1.398 ± 0.451
sim ECG tachy	10146 ± 2227	168.370 ± 38.699	1.106 ± 0.022	1.264 ± 0.227
randwalk linear	197.919 ± 3.866	52590 ± 61527	1.623 ± 0.661	1.872 ± 0.920

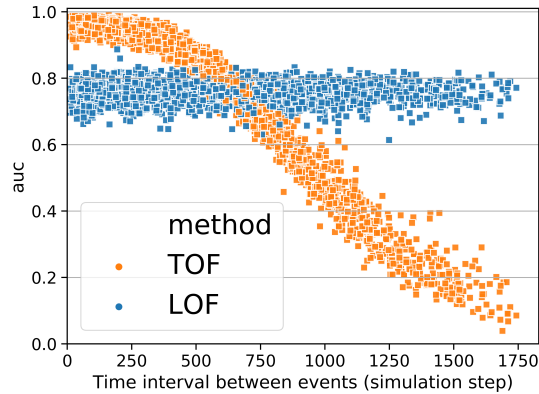


Figure 16: **TOF detects unique events.** Detection performance measured by ROC AUC as a function of the minimum inter event interval between two inserted tent-map outlier segments. Below 300 step inter event intervals, TOF found outliers with good performance, however for greater than 300 steps the algorithm found fewer outliers. In contrast, LOF’s performance remained constant over the whole IEI range.

#### 4.2.5 TOF detects unicorns

To show that TOF enables detection of only unique events, additional simulations were carried out, where two, instead of one, tent-map outlier segments were inserted into the logistic map simulations. We detected outliers by TOF and LOF and subsequently ROC AUC values were analyzed as a function of the inter event interval (IEI, Fig. 16) of the outlier segments. LOF performed independent of IEI, but TOF’s performance showed

strong IEI-dependence. Highest TOF ROC AUC values were found at small IEI-s and AUC was decreasing with higher IEI. Also the variance of ROC AUC values was increasing with IEI. This result showed, that the TOF algorithm can detect only unique events: if two outlier events are close enough to each other, they can be considered as one unique event together. In this case, the TOF can detect it with higher precision, compared to LOF. However if they are farther away than the time limit determined by the detection threshold, then the detection performance decreases rapidly.

The results also showed, that anomalies can be found by the TOF only if they are alone, a second appearance decreases the detection rate significantly. Based on these results we can conclude, that the TOF method can be applied to real world datasets to reveal unicorns in them.

#### 4.2.6 Application examples on real-world data series

**Detecting hypopnea events on ECG time series.** We applied TOF to the MIT-BIH Polysomnographic Database’s [120, 121] ECG measurements to detect hypopnea events. Multichannel recordings were taken on 250 Hz sampling frequency, and the ECG and respiratory signal of the first recording was selected for further analysis ( $n = 40000$  data points 1600 secs).

While the respiratory signal clearly showed the hypopnea, there were no observable changes on the parallel ECG signal.

We applied time delay embedding with  $E_{\text{TOF}} = 3$ ,  $E_{\text{LOF}} = 7$  and  $\tau = 0.02$  s according to the first zero-crossing of the autocorrelation function (Fig. 6). TOF successfully detected hypopnea events in ECG time series, interestingly, the unique behavior was found mostly during T-waves when the breathing activity was almost shut down (Fig. 17,  $k = 11$ ,  $M = 5$  s). In contrast, LOF was sensitive to the increased and irregular breathing before hypopnea ( $k = 200$ , threshold= 0.5 %). This example shows that this new method could be useful for biomedical signal processing and sensor data analysis.

**Detecting gravitational waves.** As a second example of real world datasets, we analyzed gravitational wave detector time series around the GW150914 merger event [36] (Fig. 18). The LIGO Hanford detector’s signal (4096 Hz) was downloaded from the GWOSC database [129].

A 12 s long segment of strain data around the GW150914 merger event was selected for further analysis. As a preprocessing, the signal was bandpass-filtered (50-300 Hz). Time delay embedding was carried out with embedding delay of 8 time-steps (1.953 ms) and embedding dimension of  $E = 6$  and  $E = 11$  for TOF and LOF respectively We set the parameters of the algorithms as follows:  $k = 12$ ,  $M = 146.484$  ms for TOF and  $k = 100$ ,

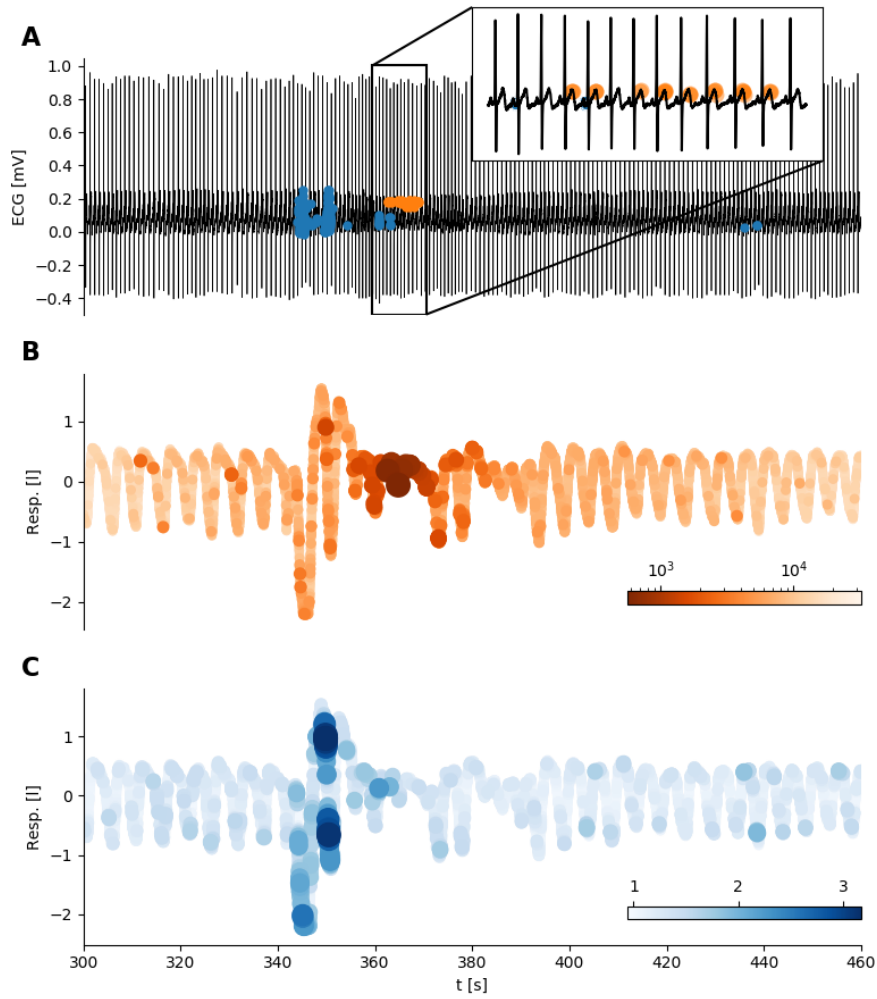


Figure 17: **Detecting hypopnea with arousal on ECG by TOF and LOF.** **a** ECG time series with unique events detected by TOF (orange,  $E = 3, \tau = 0.02 \text{ s}, k = 11, M = 5 \text{ s}$ ) and outliers detected by LOF (blue,  $E = 7, \tau = 0.02 \text{ s}, k = 100, \text{threshold} = 0.5\%$ ). The inset shows a more detailed pattern of detections: unique behavior mainly appears on the T waves. **b** Air-flow time series with coloring corresponds to the TOF score at each sample. Low values mark the anomaly. After a normal period, the breathing gets irregular and almost stops, then after arousal the breathing pattern becomes normal again. TOF finds the period, when the breathing activity almost stops. **c** Air-flow time series with coloring corresponds to the LOF score at each sample. Higher LOF values mark the outliers. LOF finds irregular breathing preceding the hypopnea.

threshold= 0.5% for LOF (Fig. 7).

Both TOF and LOF detected the merger event, however TOF selectively detected the period when the chirp of the spiraling mergers was the loudest (Fig. 18 b, c).

**London InterBank Offer Rate dataset** We also applied TOF and LOF on the London InterBank Offer Rate (LIBOR) dataset. As a preprocessing, discrete time derivative was

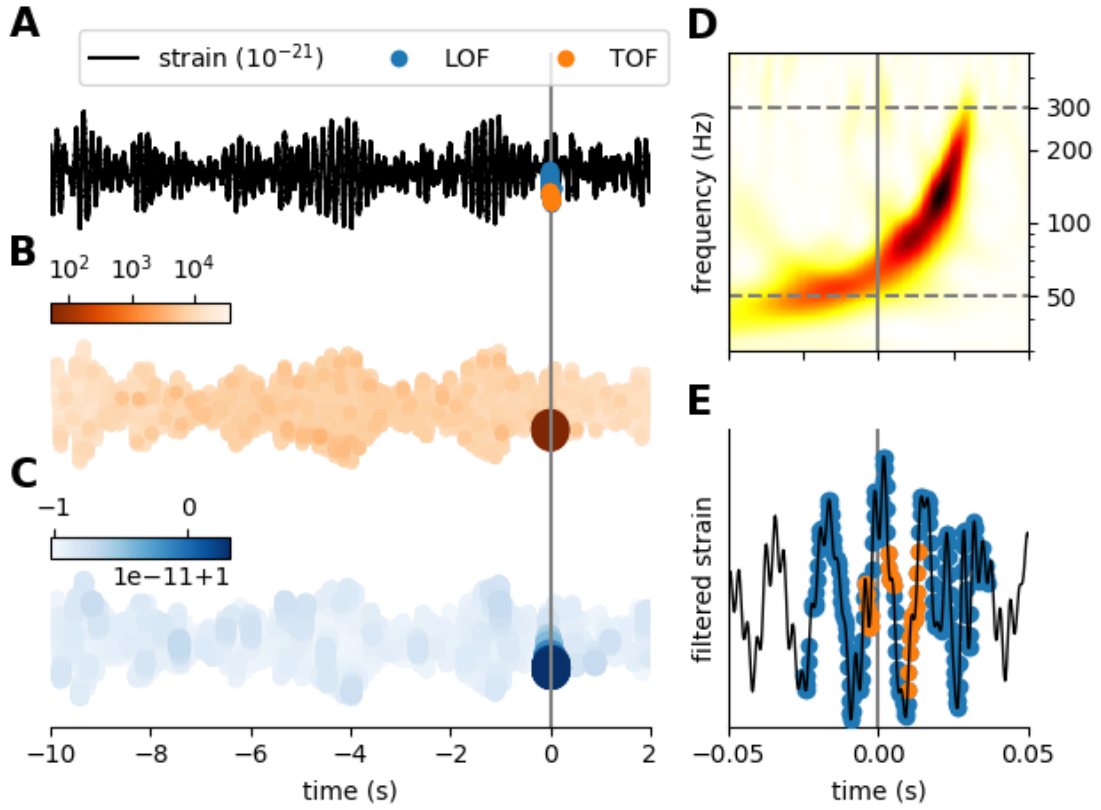


Figure 18: **Detection of the GW150914 event on LIGO open data with LOF and TOF.** **a** Strain time series (black) from Hanford detector around GW150914 event (grey) with LOF (blue) and TOF (orange) detections. TOF score values (**b**) and LOF scores (**c**) are mapped to the time series (orange and blue respectively), the most strong colors shows the detected event around 0 seconds. **d** The Q-transform of the event shows a rapidly increasing frequency bump in the power spectra right before the merger event (grey). The grey dashed lines show the lower (50 Hz) and upper (300 Hz) cutoff frequencies of the band-pass filter, which was applied on the time series as a preprocessing step before anomaly detection. **e** Filtered strain data at 0.1 second neighborhood around the event. LOF and TOF detected the merger event with different sensitivity, LOF detected more points of the event, while TOF found the period which has the highest power in the power spectra. ( $E_{\text{TOF}} = 6$ ,  $\tau_{\text{TOF}} = 1.953$  ms,  $k_{\text{TOF}} = 12$ ,  $M = 146.484$  ms,  $w = 7$ ;  $E_{\text{LOF}} = 11$ ,  $\tau_{\text{LOF}} = 1.953$  ms,  $k_{\text{LOF}} = 100$ , threshold= 0.5%)

calculated to eliminate global trends, then TOF ( $E = 3$ ,  $\tau = 1$ ,  $k = 5$ ,  $M = 30$  month) and LOF ( $E = 3$ ,  $\tau = 1$ ,  $k = 30$ , threshold= 18.86 %) was applied on the derivative (Fig. 8-9). TOF found the uprising period prior to the 2008 crisis and the slowly rising period from 2012 onwards as outlier segments. LOF detected several points, but no informative pattern emerges from the detections (Fig. 19). While in this case the ground-truth was not known, the two highlighted periods show specific patterns of monotonous growth. Moreover, the fact that both two periods were detected by the TOF shows that both dynamics are unique,

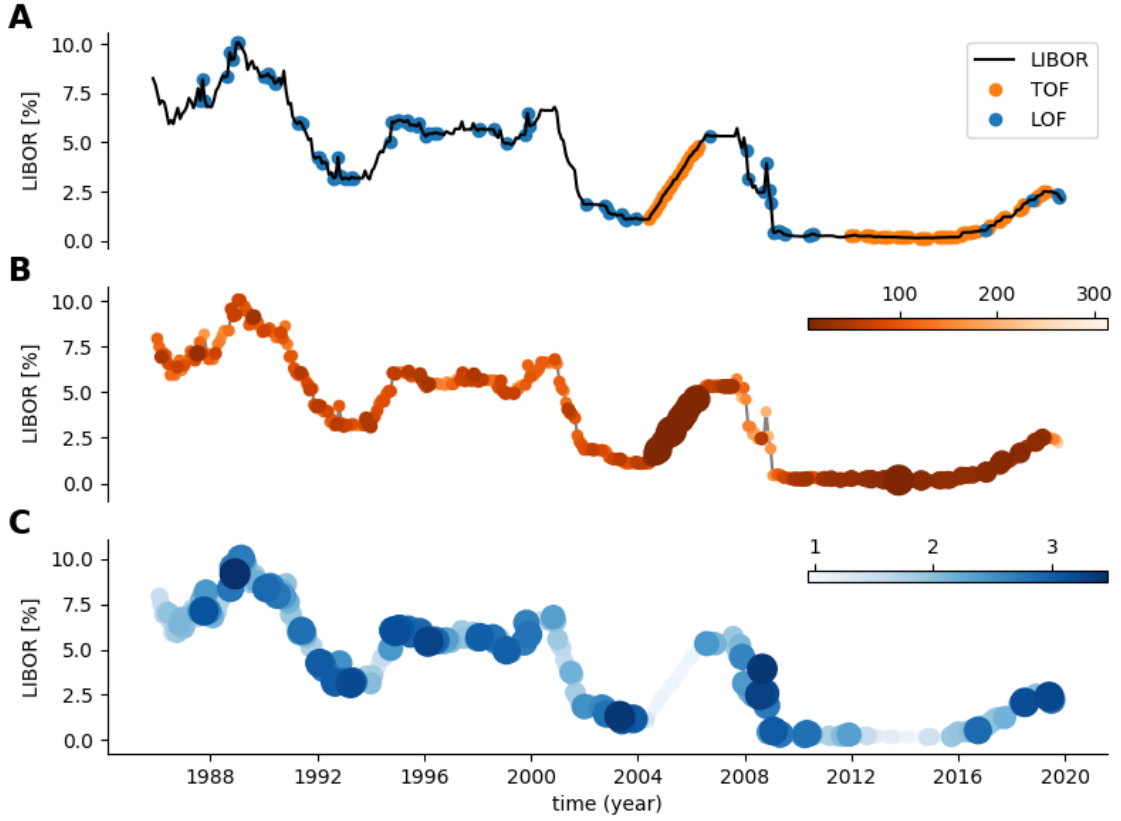


Figure 19: **Analysis of LIBOR dataset.** The detections were run on the temporal derivative of the LIBOR time series. **a** time series with detections. **b** TOF score values. **c** LOF score values. TOF detected two rising periods: the first between 2005 and 2007 and a second, started in 2012 and lasts until now. While both periods exhibit unique dynamics, they differ from each other as well.

therefore different from each other during the two periods.

### 4.3 Estimating intrinsic dimensionality to explore seizure dynamics

#### 4.3.1 Manifold adaptive dimension estimator revisited

**The probability density of Farahmand-Szepesvári-Audibert estimator** We compute the probability density function of Farahmand-Szepesvári-Audibert (FSA) intrinsic dimension estimator based on normalized distances.

The normalized distance density of the  $k$ NN can be computed in the context of a  $K$ -neighborhood, where the normalized distance of  $K - 1$  points follows a specific form:

$$p(r|k, K - 1, D) = \frac{D}{B(k, K - k)} r^{Dk-1} (1 - r^D)^{K-k-1} \quad (65)$$

where  $r$  is the normalized distance of the  $k$ th neighbor by the distance of  $K$ th neighbor

( $r_k = R_k/R_K$ ,  $k < K$ ) and  $B$  is the Euler-beta function. The formula in Eq. 65 can be derived from the uniform local density and independent sampling assumptions [130]. A maximum likelihood estimator based on Eq. 65 leads to the formula of the classical Levina-Bickel estimator [56, 130].

We realize that the inverse of normalized distance appears in the formula of FSA estimator, so we can express it as a function of  $r$ :

$$d_k = \frac{\log 2}{\log (R_{2k}/R_k)} = -\frac{\log 2}{\log (R_k/R_{2k})} = -\frac{\log 2}{\log r_k} \quad (66)$$

Where  $r_k = R_k/R_{2k}$ .

Thus, we can compute the pdf of the estimated values as plugging in  $K = 2k$  into Eq. 65 followed by change of variables:

$$q(d_k) \equiv p(r|k, 2k-1, D) \left| \frac{dr}{dd_k} \right| = \frac{D \log(2)}{B(k, k)} \frac{2^{-\frac{Dk}{d_k}} \left(1 - 2^{-\frac{D}{d_k}}\right)^{k-1}}{d_k^2} \quad (67)$$

**Theorem 2.** *The median of  $q(d_k)$  is at  $D$ .*

*Proof.* We apply the substitution  $a = 2^{-D/d_k}$  in Eq. 67 (Eq. 70):

$$p(a) = q(d_k) \left| \frac{dd_k}{da} \right| = \quad (68)$$

$$= \frac{D \log(2)}{B(k, k)} \frac{a^k (1-a)^{k-1} \log^2 a}{D^2 \log^2 2} \frac{D \log 2}{a \log^2 a} \quad (69)$$

$$= \frac{1}{B(k, k)} a^{k-1} (1-a)^{k-1} \quad (70)$$

The pdf in Eq.70 belongs to a beta distribution. The cumulative distribution function of this density is the regularized incomplete Beta function with  $k$  as both parameters symmetrically.

$$P(a) = I_a(k, k) \quad (71)$$

The median of this distribution is at  $a = \frac{1}{2}$ , thus at  $d_k = D$  since:

$$a = 2^{-\frac{D}{d_k}} = \frac{1}{2} \quad (72)$$

$$D = d_k \quad (73)$$

□

This means that the median of the FSA estimator is equal to the intrinsic dimension

independent of neighborhood size, if the locally uniform point density assumption holds. The sample median is a robust statistic, therefore we propose to use the sample median of local estimates as a global dimension estimate. We will call this modified method the median Farahmand-Szepesvári-Audibert (mFSA) estimator.

Let's see the form for the smallest possible neighborhood size:  $k = 1$  (Fig. 20). The pdf for the estimator takes a simpler form (Eq. 74).

$$q(d|k = 1, D) = D \log(2) \frac{2^{-\frac{D}{d_1}}}{d_1^2} \quad (74)$$

Also, we can calculate the cumulative distribution function analytically (Eq. 75).

$$Q(d|k = 1, D) = \int_0^{d_1} q(t|k = 1, D) dt = 2^{-D/d_1} \quad (75)$$

The expectation of  $d_k$  diverges for  $k = 1$  – but not for  $k > 1$  – although the median exists.

From Eq. 75 the median is at  $D$  (Eq. 76).

$$Q(d_1 = D) = 0.5 \quad (76)$$

**Sampling distribution of the median.** We can easily compute the pdf of the sample median if an odd sample size is given ( $n = 2l + 1$ ) and if sample points are drawn independently according to Eq. 67. Roughly half of the points have to be smaller, half of the points have to be bigger and one point has to be exactly at  $m$  (Eq. 77).

$$p(m|k, D, n) = \frac{1}{B(l+1, l+1)} [P(a = 2^{-D/m}) (1 - P(a = 2^{-D/m}))]^l q(m) \quad (77)$$

Where  $p(a)$  and  $P(a)$  are the pdf and cdf of  $a$  (Eq. 70, 71) and  $q$  is the pdf of the FSA estimator (Fig. 21).

**Maximum Likelihood solution for the manifold-adaptive estimator** If the samples are independent and identically distributed, we can formulate the likelihood function as the product of sample-likelihoods (Eq. 78). We seek for the maximum of the log likelihood function, but the derivative is transcendental for  $k > 1$ . Therefore, we can compute the place of the maximum numerically (Eq. 81).

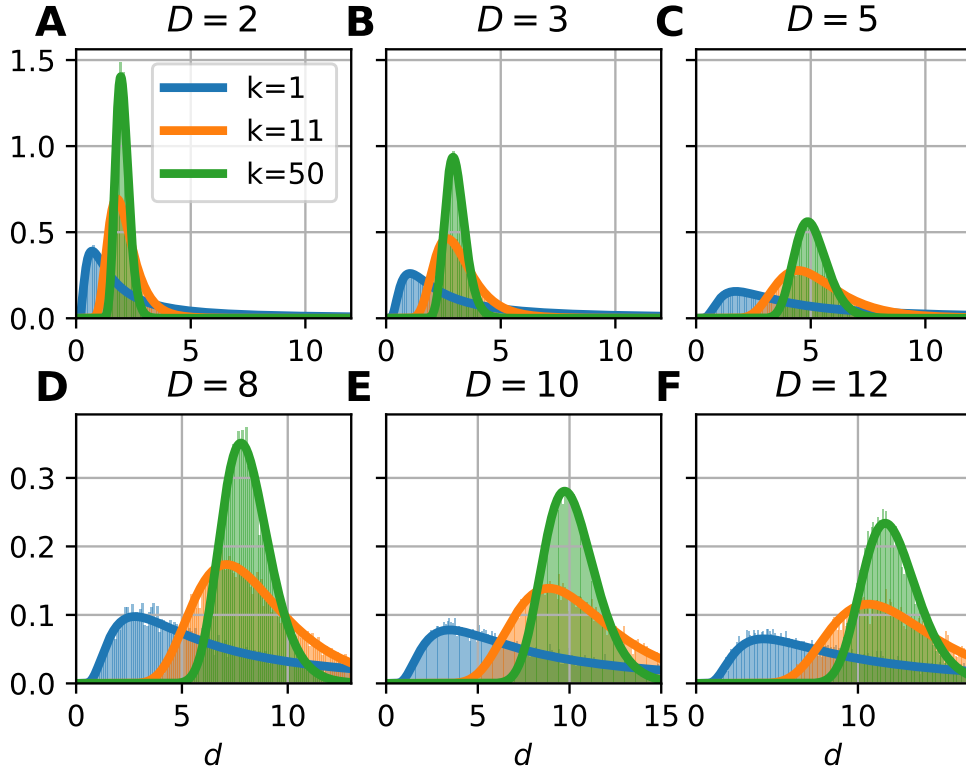


Figure 20: **Probability density function of the Farahmand-Szepesvári-Audibert estimator ( $d$ ) for various dimensions ( $D$ ) and neighborhood sizes ( $k$ ).** A-F The subplots show that theoretical pdfs (continuous lines) fits to the histograms ( $n = 10000$ ) of local estimates calculated on uniformly sampled hypercubes ( $D = 2, 3, 5, 8, 10, 12$ ). The three colors denote three presented neighborhood sizes:  $k = 1$  (blue),  $k = 11$  (orange) and  $k = 50$  (green).

$$\mathcal{L} = \prod_{i=1}^n \frac{D \log(2) 2^{-Dk/d_k^{(i)}} (1 - 2^{-D/d_k^{(i)}})^{k-1}}{B(k, k) (d_k^{(i)})^2} \quad (78)$$

$$\begin{aligned} \log \mathcal{L} &= n \log \frac{\log(2)}{B(k, k)} + n \log D - Dk \log(2) \sum \frac{1}{d_k^{(i)}} \\ &\quad + (k-1) \sum \log(1 - 2^{-D/d_k^{(i)}}) - 2 \sum \log(d_k^{(i)}) \end{aligned} \quad (79)$$

$$\frac{\partial \log \mathcal{L}}{\partial D} = \frac{n}{D} - \log(2)k \sum \frac{1}{d_k^{(i)}} \quad (80)$$

$$+ \log(2)(k-1) \sum \frac{1}{d_k^{(i)}(2^{D/d_k^{(i)}} - 1)} \stackrel{!}{=} 0 \quad (81)$$

For  $k = 1$ , the ML formula is equal to the Levina-Bickel ( $k = 1$ ) and  $\text{MIND}_{\text{IML}}$  formulas.

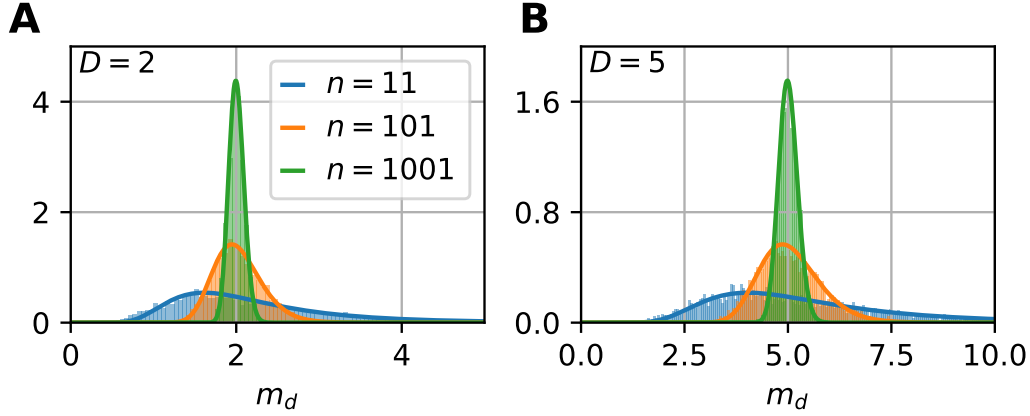


Figure 21: **The sampling distribution of the median for the FSA estimator ( $k = 1$ ) on uniformly sampled hypercubes.** The figure shows the pdf of median-FSA estimator of points uniformly sampled from a square (A) and from a 5D hypercube (B) for three sample sizes:  $n = 11$  (blue),  $n = 101$  (orange) and  $n = 1001$  (green) respectively. The solid lines represent the theoretical pdf-s of the median and the shaded histograms are the results of simulations ( $N = 5000$  realizations).

**Results on randomly sampled hypercube datasets** Theoretical probability density function of the local FSA estimator fits to empirical observations (Eq. 67, Fig. 20). We simulated hypercube datasets with fixed sample size ( $n = 10000$ ) and of various intrinsic dimensions ( $D = 2, 3, 5, 8, 10, 12$ ). We measured the local FSA estimator at each sample point with 3 different  $k$  parameter values ( $k = 1, 11, 50$ ). We visually confirmed that the theoretical pdf fits perfectly to the empirical histograms.

The empirical sampling distribution of mFSA fits to the theoretical curves for small intrinsic dimension values (Fig. 21). To demonstrate the fit, we drew the density of mFSA on two hypersphere datasets  $D = 2$  and  $D = 5$  with the smallest possible neighborhood ( $k = 1$ ), for different sample sizes ( $n = 11, 101, 1001$ ). At big sample sizes the pdf is approximately a Gaussian [131], but for small samples the pdf is non-Gaussian and skewed.

The mFSA estimator underestimates intrinsic dimensionality in high dimensions. This phenomena is partially a finite sample effect (Fig. 22), but edge effects make this underestimation even more severe. We graphically showed that mFSA estimator asymptotically converged to the real dimension values for hypercube-datasets, when we applied periodic boundary conditions (Fig. 23). We found, that the convergence is much slower for hard boundary conditions, where edge effects make estimation errors higher.

We could estimate the logarithm of relative error with an  $s$ -order polynomial:

$$\log(E_{rel}) = \log\left(\frac{D}{d}\right) = \sum_{i=1}^s \alpha_i d^i \quad (82)$$

The order of the polynomial was different for the two types of boundary conditions. When we applied hard boundary, the order was  $s = 1$ , however in the periodic case higher order polynomials fit the data. Thus, in the case of hard-boundary, we could make the empirical correction formula:

$$D \approx C(\hat{d}) = de^{\alpha_n d} \quad (83)$$

where  $\alpha_n$  is a sample size dependent coefficient that we could fit with the least squares method.

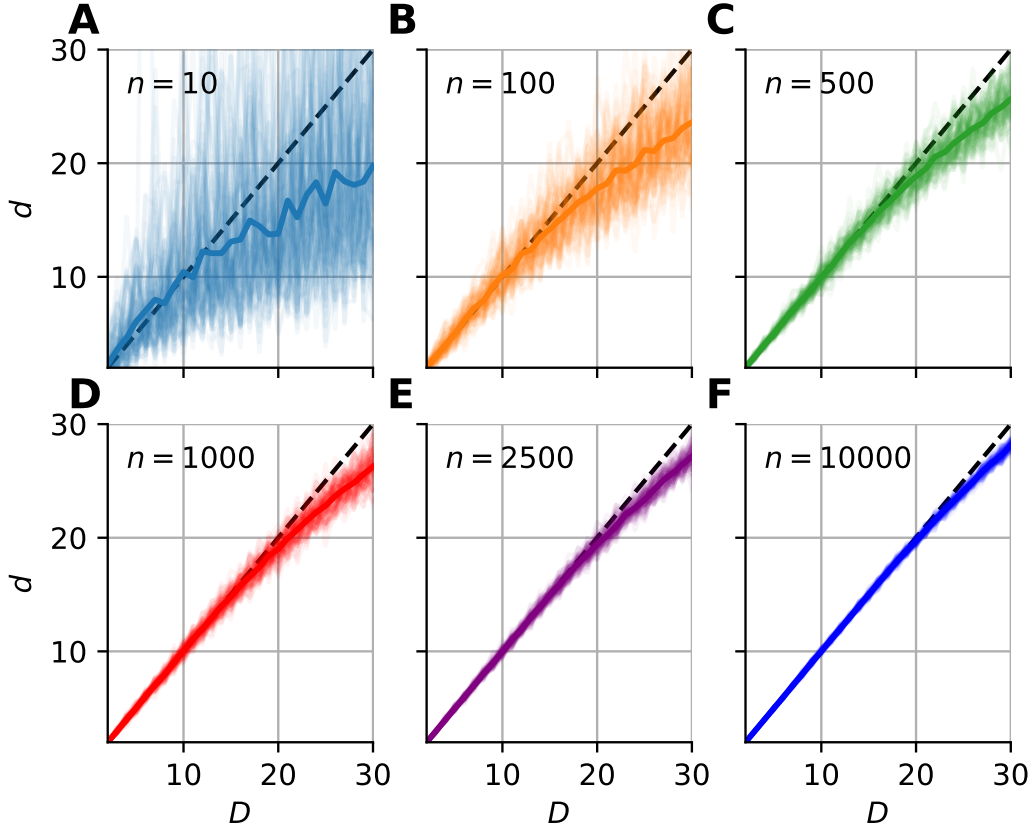


Figure 22: **Intrinsic dimension dependence of the median-FSA estimator for uniformly sampled unit hypercubes with various sample sizes ( $k = 1$ ).** Subplots A-F show the mean of median-FSA estimator (thick line) values from  $N = 100$  realizations (shading) of uniformly sampled unit hypercubes with periodic boundary.

### 4.3.2 Results on synthetic benchmarks

We tested the mFSA estimator and its corrected version on synthetic benchmark datasets [55, 132]. We simulated  $N = 100$  instances of 15 manifolds ( $M_i, n = 2500$ ) with various intrinsic dimensions (see Table 1, 2, 4 in Campadelli et al. [55], <http://www.mL.uni-saarland.de/code/IntDim/IntDim.htm>).

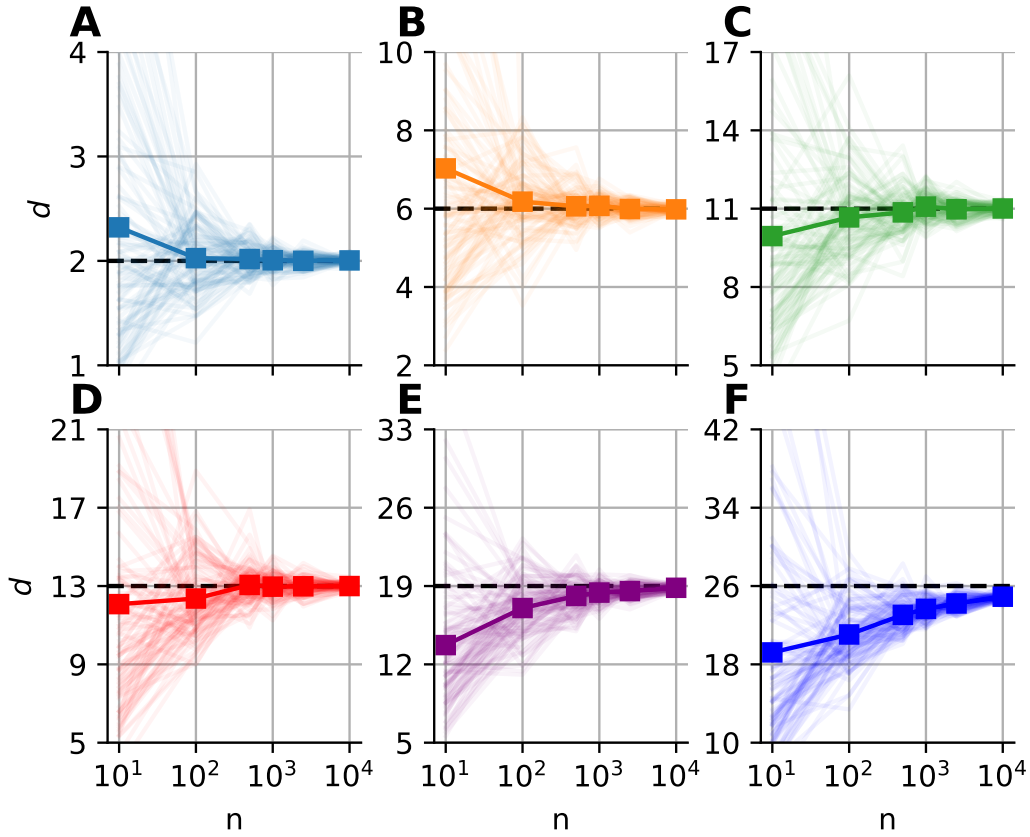


Figure 23: **Sample size dependence of the median-FSA estimator for uniformly sampled unit hypercubes with varied intrinsic dimension value ( $k = 1$ ).** Subplots A-F show the mean of median-FSA estimator (thick line) values from  $N = 100$  realizations (shading).

We estimated the intrinsic dimensionality of each sample and computed the mean, the error rate and Mean Percentage Error (MPE) for the estimators. We compared the mFS, cmFS, the R and the matlab implementation of DANCo, and the Levina-Bickel estimator (Table 4). cmFSA and DANCo was evaluated in two modes, in a fractal-dimension mode and in an integer dimension mode.

The mFSA and the Levina-Bickel estimator underestimated intrinsic dimensionality, especially in the cases when the data had high dimensionality.

In contrast, the cmFSA (cmFSA) estimator found the true intrinsic dimensionality of the datasets, it reached the best overall error rate (0.277) and 2nd best MPE (Fig. 25, Table 4). In some cases, it slightly over-estimated the dimension of test datasets. Interestingly, DANCo showed implementation-dependent performance, the MATLAB algorithm showed the 2nd best error rate (0.323) and the best MPE value (Table 4). The R version overestimated the dimensionality of datasets in most cases.

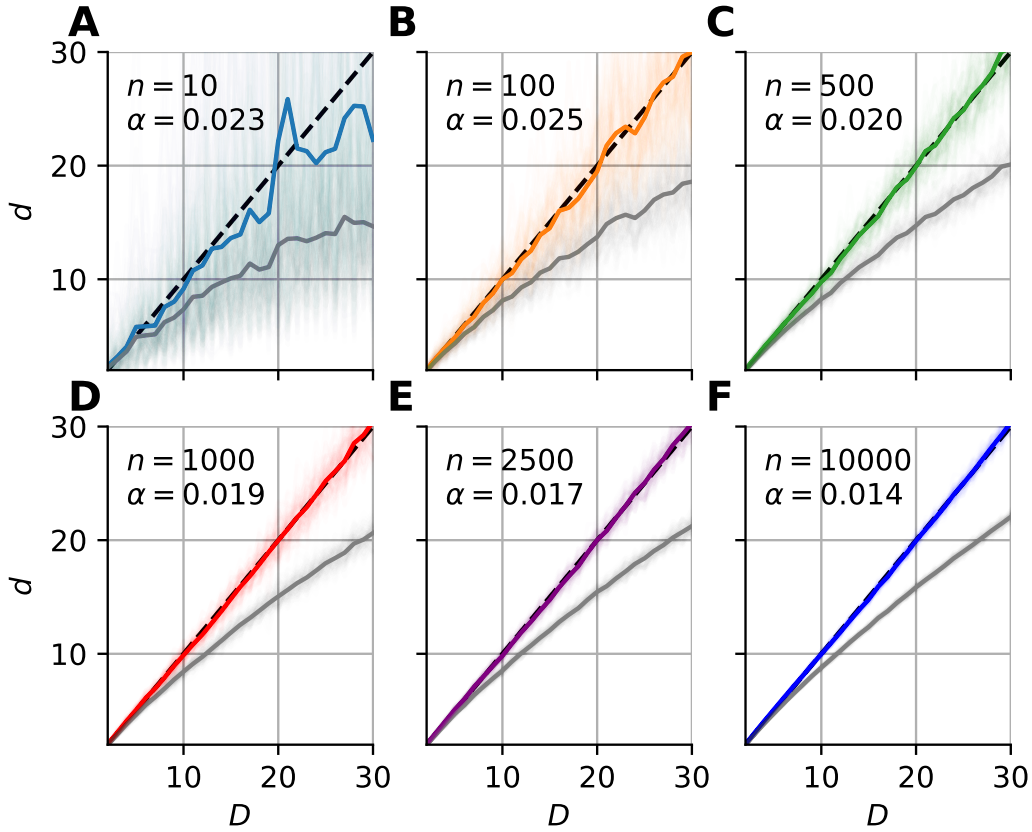


Figure 24: **Bias-correction of the median-FSA estimator for uniformly sampled unit hypercubes with various sample sizes ( $k = 1$ ).** Subplots A-F show the mean of median-FSA estimator (grey line) values from  $N = 100$  realizations (shading) of uniformly sampled unit hypercubes. The boundary condition is hard, so the edge effect makes underestimation more severe. The colored lines show the corrected estimates according to the  $\hat{w}_c = \hat{w} \exp(\alpha \hat{w})$ .

### 4.3.3 Analysing epileptic seizures

To show how mFSA works on real-world noisy data, we applied it to human neural recordings of epileptic seizures.

We acquired field potential measurements from a patient with drug-resistant epilepsy by 2 electrode grids and 3 electrode strips. We analyzed the neural recordings during interictal periods and during epileptic activity to map possible seizure onset zones (see Methods, Fig. 10).

We found several characteristic differences in the dimension patterns between normal and control conditions. In interictal periods (Fig. 27 A), we found the lowest average dimension value at the FbB2 position on the fronto-basal grid. Also, we observed a diagonal gradient of intrinsic dimensions on the cortical grid (Gr). In contrast, we observed the lowest dimension values at the hippocampal electrode strip (JT), and the gradient on the cortical grid disappeared during seizures (Fig. 27 B). Curiously, the intrinsic dimen-

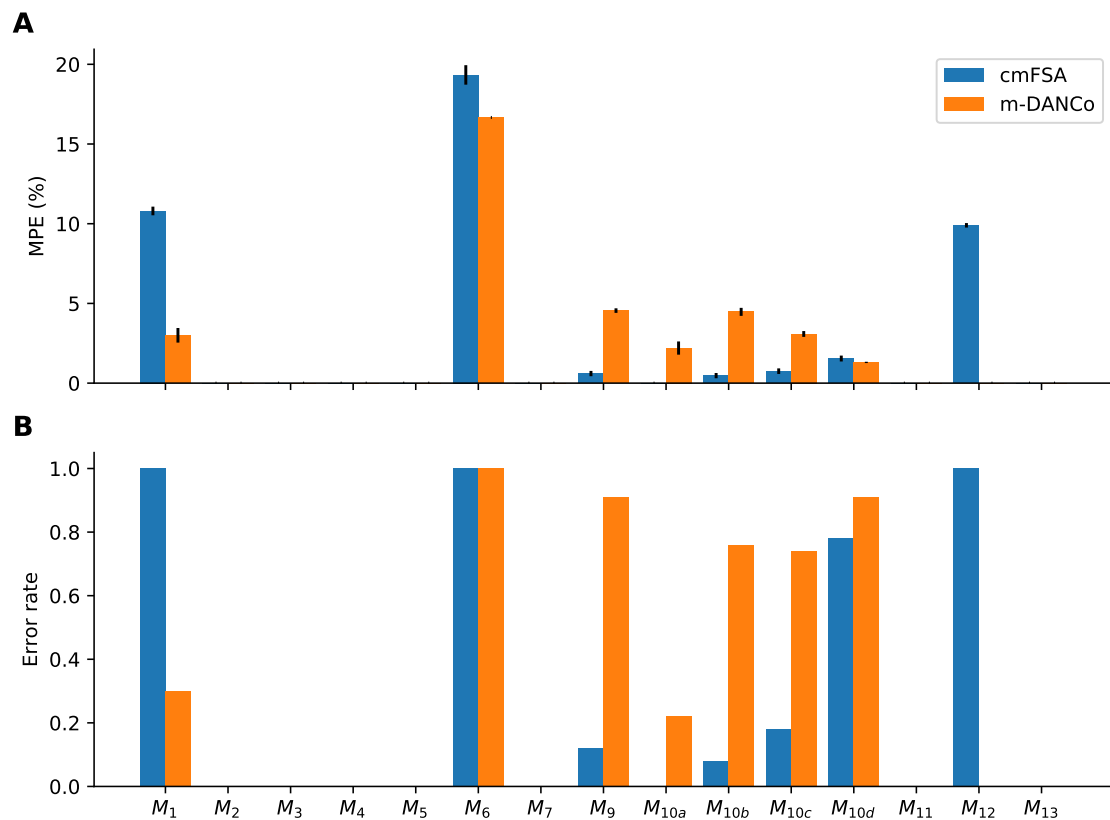


Figure 25: **Performance-comparison between cmFSA and DANCo on synthetic benchmark datasets.** **A** Dataset-wise Mean Percentage Error (MPE) on benchmark data. cmFSA (blue) shows smaller MPE in 4 cases and bigger MPE in 4 cases compared with DANCo (matlab). **B** Dataset-wise error rate for cmFSA and DANCo. cmFSA shows smaller error rates in 5 cases and bigger error rates in 2 cases compared with DANCo.

sionality became higher at fronto-basal recording sites during seizure (Fig. 27 C).

#### 4.4 Investigating the causal relation between Local Field Potential and Intrinsic Optical Signal

Three methods have been applied to evoke the epileptiform activity in rat neocortical slice preparations: electric stimulation (STIM, 5 slices), application of  $Mg^{2+}$ -free artificial cerebrospinal fluid (4 slices) and 4-aminopyridine (4AP) treatment (4 slices). All the three methods evoked epileptiform activity by means of recurrent population burst discharges in the slices. There were specific differences between the burst discharges which were characteristic for the method of induction and there were large variation among slices as well. The induction-specific characteristic properties include the amplitude, the intraburst and interburst frequencies as well as the temporal development of the activity during the 1 hour long measurements [133]. The IOS was measured parallel, by quantifying the rel-

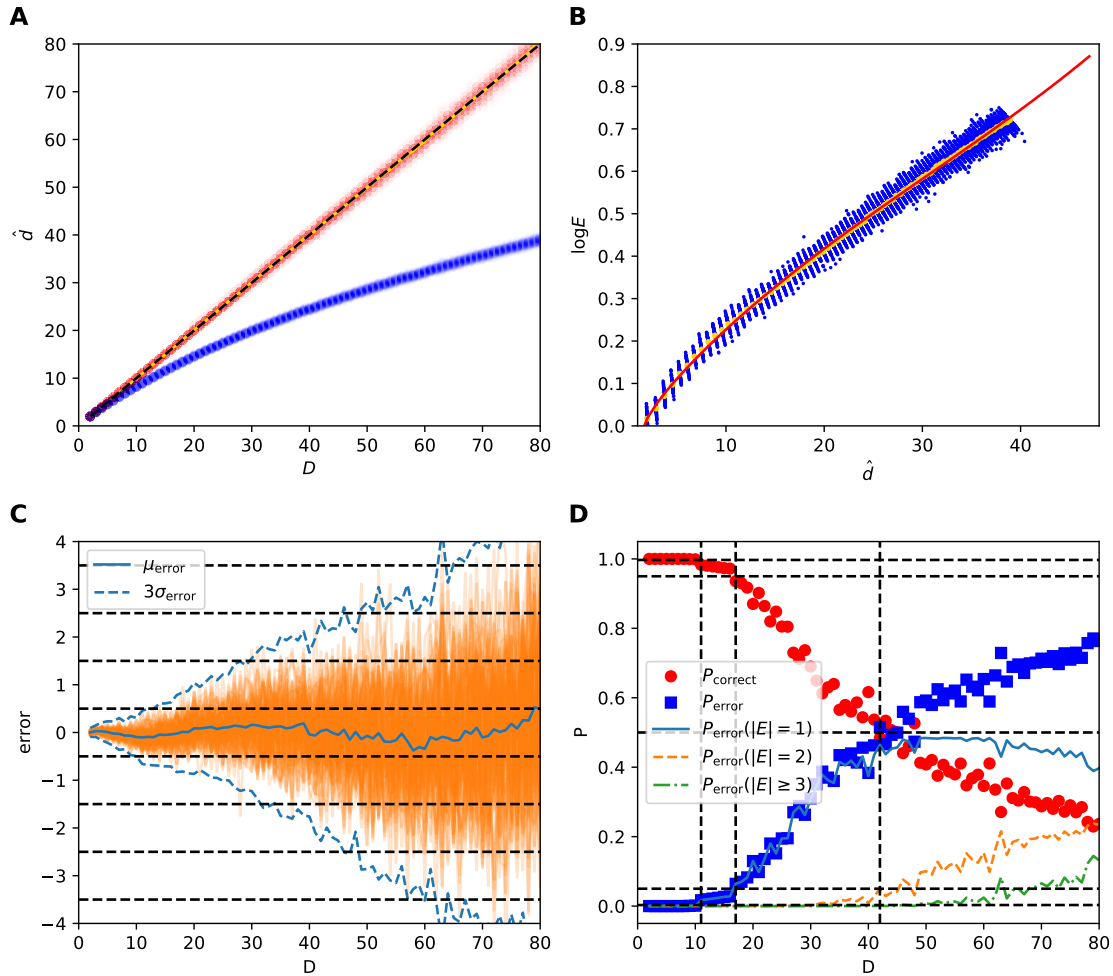


Figure 26: **Calibration procedure for the  $n = 2500$  datasets up to  $D = 80$  ( $k = 5$ ).** The figure shows the calibration procedure on 100 instances of uniformly sampled hypercubes. **A** Dimension estimates in the function of intrinsic dimensionality for the calibration hypercubes. The diagonal (dashed) is the ideal value, however the mFSA estimates (blue) show saturation because of finite sample and edge effects. cmFSA estimates (red) are also shown, with the mean (yellow) almost aligned with the diagonal. **B** The relative error ( $E$ ) in the function of uncorrected mFSA dimension on semilogarithmic scale. The error-mFSA pairs (blue) lie on a short stripe for each intrinsic dimension value. The subplot also shows id-wise average points (yellow) and the polynomial fitting curve (red). **C** The error of cmFSA estimates in the function of intrinsic dimension on the calibration datasets. The mean error (blue line) oscillates around zero and the 99.7% confidence interval (blue dashed) widens as ID grows. The rounding switch-points are also shown. **D** The probability that cmFSA hits the real ID of data, or misses by one, two or more as a function of ID on the calibration dataset.

Table 4: **Dimension estimates on synthetic benchmark datasets.**

The table shows true dimension values, median-Farahmand-Szepesvári-Audibert, Maximum Likelihood, corrected median Farahmand-Szepesvári-Audibert and DANCo mean estimates from  $N = 100$  realizations. The MPE values can be seen in the bottom line, the matlab version of DANCo estimator produced the smallest error followed by the cmFSA estimator.

	dataset	d	mFSA	cmFSA <sub>fr</sub>	cmFSA	R-DANCo	M-DANCo <sub>fr</sub>	M-DANCo	Levina
1	$M_1$	10	9.09	11.19	11.08	12.00	10.42	<b>10.30</b>	9.40
2	$M_2$	3	2.87	3.02	3.00	3.00	2.90	3.00	2.93
3	$M_3$	4	3.83	4.14	4.00	5.00	3.84	4.00	3.86
4	$M_4$	4	3.95	4.29	4.00	5.00	3.92	4.00	3.92
5	$M_5$	2	1.97	2.00	2.00	2.00	1.98	2.00	1.99
6	$M_6$	6	6.38	7.38	7.16	9.00	6.72	7.00	<b>5.93</b>
7	$M_7$	2	1.95	1.98	2.00	2.00	1.96	2.00	1.98
8	$M_9$	20	14.58	<b>20.07</b>	20.10	19.13	19.24	19.09	15.56
9	$M_{10a}$	10	8.21	9.90	<b>10.00</b>	10.00	9.56	9.78	8.64
10	$M_{10b}$	17	12.76	16.95	<b>16.96</b>	16.01	16.39	16.24	13.60
11	$M_{10c}$	24	16.80	24.10	<b>24.06</b>	23.15	23.39	23.26	18.05
12	$M_{10d}$	70	35.64	69.84	<b>69.84</b>	71.52	71.00	70.91	40.12
13	$M_{11}$	2	1.97	2.00	2.00	2.00	1.97	2.00	1.98
14	$M_{12}$	20	15.64	21.96	21.98	21.03	20.88	<b>20.00</b>	17.26
15	$M_{13}$	1	1.00	0.96	1.00	1.00	1.00	1.00	1.00
	MPE		13.58	4.73	2.89	10.07	3.39	2.35	10.81

ative changes in the reflected or transmitted light flux over the somatosensory cortex. In 12 slices, the IOS signal was measured in interface setup, which allowed the measurement of the reflected light, but in one slice, the  $Mg^{2+}$ -free induced activity was measured in submerged setup, which made possible the measurement of the transmitted light. An example of the  $Mg^{2+}$ -free evoked epileptiform activity, the parallel recorded LFP and reflected IOS are shown in Fig. 28 B.

#### 4.4.1 The slow and the fast components of the IOS signal

The general temporal development of the reflected IOS signal during the epileptic activity induction is consists of two components: The first component is a slow and slowly saturating negative shift in the baseline, while the second, faster component takes shape in negative waves descending after each epileptic discharge and slowly converging back to the baseline during the discharge-free periods (Fig. 28). Comparing the IOS time courses in transmitted and reflected light, we found that the slow component is negative in both cases, while the faster component changed its sign: negative in reflected, but positive

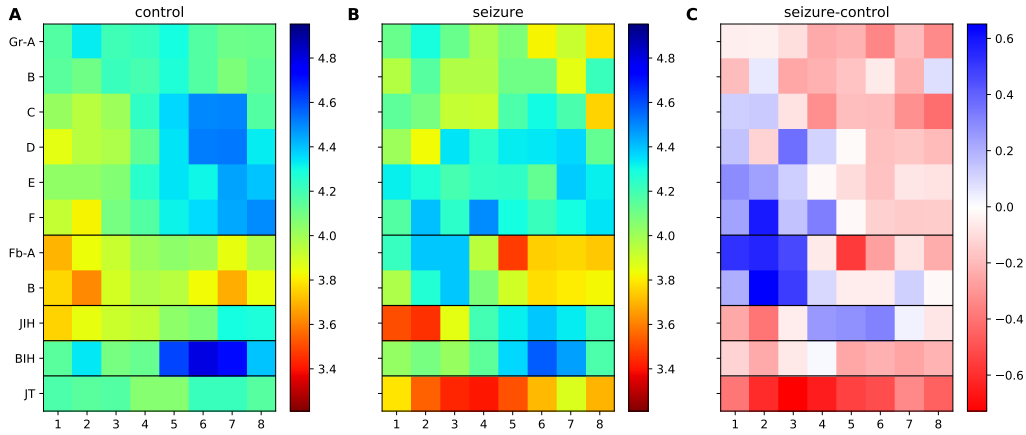


**Figure 27: mFSA Dimension estimates on intracranial Brain-LFP measurements during interictal activity and epileptic seizures.** The figure shows the dimension estimates on an intracranial cortical grid (Gr A-F), a smaller Frontobasal grid (Fb A, B) and 3 electrode strips with hippocampal and temporal localization (JIH, BIH, JT). The areas with lower-dimensional dynamics are marked by stronger colors. **A** Average of mFSA dimension values from interictal LFP activity (N=16, k=10-20). **B** Average of mFSA dimension values from seizure LFP activity (N=18, k=10-20). **C** Difference of dimension values. Stronger red color marks areas, where the dynamics during seizure was smaller-dimensional than its interictal counterpart. However, stronger blue indicates electrodes, where the during-seizure dynamics was higher dimensional than the interictal dynamics.

in the transmitted light (Fig. 29 A and C). Considering, that scattering decreases the flux of the transmitted light but increases the amount of the reflected light, while absorption decreases both the transmitted and the reflected components, we concluded, that the two components differ not only in their time scale, but also in the underlying mechanisms. The slow component is a result of the absorption of the tissue, while the faster component corresponds to the changes in the scattering or reflectance of the neural tissue. Thus, we divided the two signals by subtracting a 100 s long moving window average from the raw IOS, resulting in a slower, low frequency component IOSl and a faster, high frequency component IOSh signal (Fig. 29 B and D).

#### 4.4.2 Time delayed causality between LFP power and the fast component of IOS

The sampling frequency of the LFP signal was 1 kHz, while the sampling rate of the parallel IOS recordings were only 2 Hz. As the dynamics of IOS is much slower than the LFP, this low sampling rate was enough to track the temporal changes of the IOS. However, the causality analysis requires fully synchronous time series. To reach this, the LFP signal was undersampled, by calculating the sum of the squared LFP amplitudes (the LFP power) within each 0.5 s long sampling interval.

The CCM method of Sugihara [88], extended for delayed effects by Ye et al. [91], was

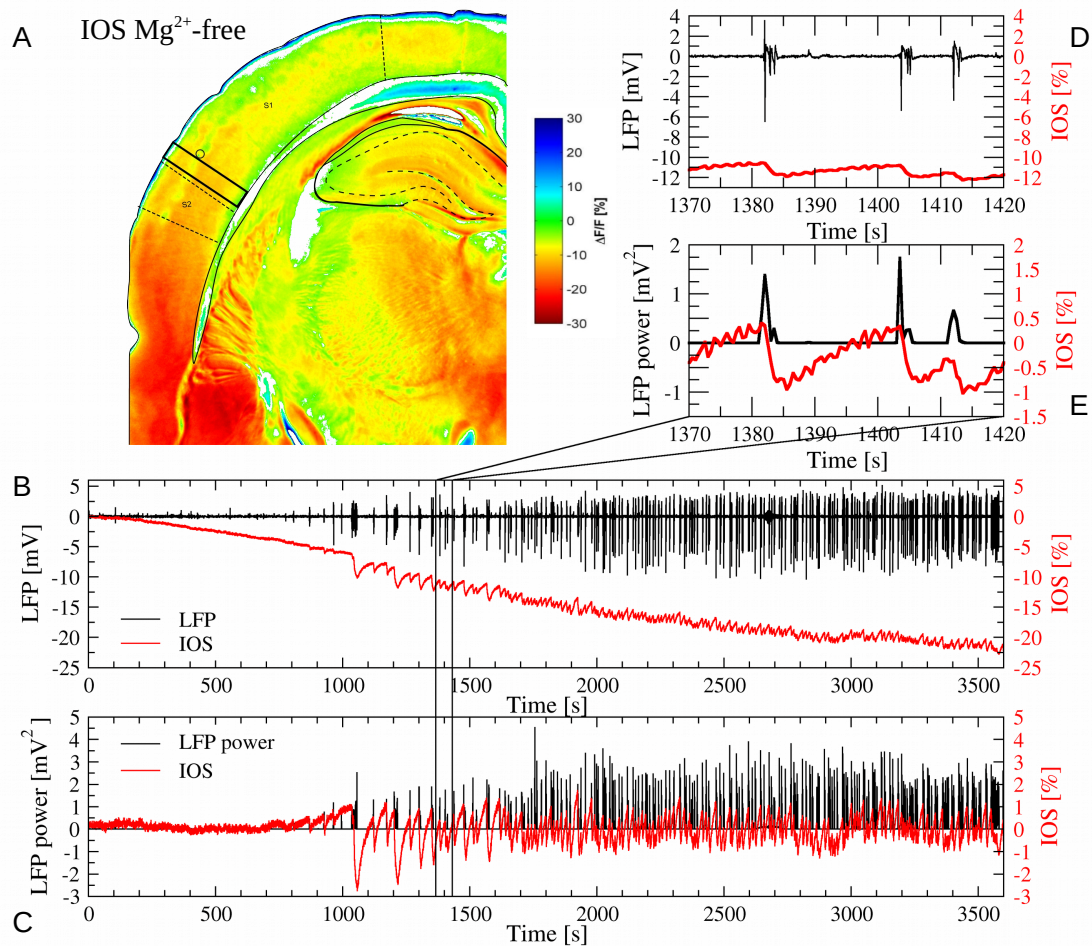


Figure 28: **The spatial distribution and temporal evolution of the IOS.** A: Pseudo color plot of the relative reflectance changes (IOS) of the coronal brain slice. The temporal evolution of the IOS was tracked by calculating the mean IOS within the ROI in the somatosensory cortex (rectangle with solid black line) close to the electrode position (open circle) in which the LFP was recorded. B and D: Parallel recorded LFP (black) and the IOS (red) during epileptiform activity induced by  $Mg^{2+}$ -free artificial cerebrospinal fluid. C and E: Downsampled LFP power (black) and detrended IOSh (red) are the variables for which the causality was analyzed.

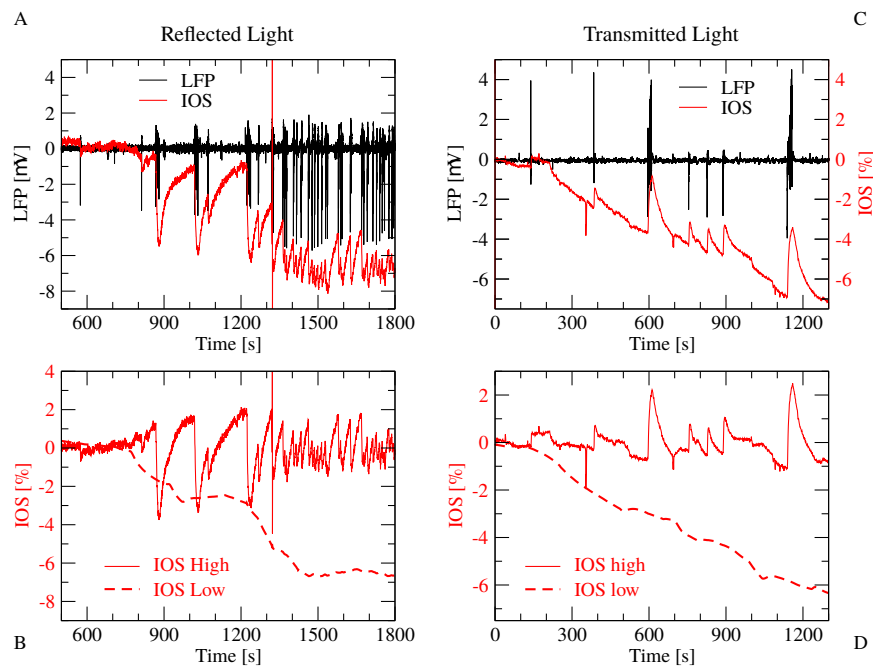
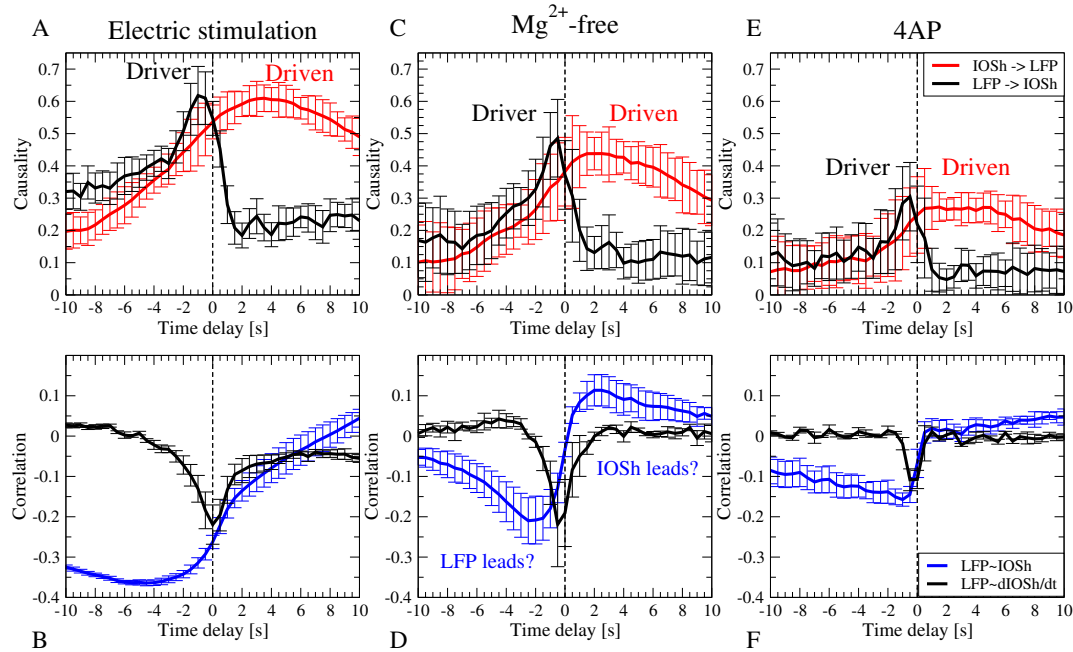


Figure 29: **Comparison of the IOS activity in reflected and transmitted light during epileptic activity evoked by  $Mg^{2+}$ -free solution** A: LFP (black) and IOS (red) signal in reflected light. B: High (IOSh, solid line) and low (IOSl, dashed line) frequency components of the IOS signal. IOSl was calculated by moving window averaging the IOS time series, while IOSh is a result of the subtraction of IOSl from IOS. C: LFP (black) and IOS (red) signal in transmitted light. D: IOSh and IOSl in transmitted light. Note, that IOSl were negative in both the reflected and the transmitted measurements, while the negative IOSh changed its sign in the transmitted setup.



**Figure 30: Causality as a function of time delay during epileptiform activity evoked by three different forms of evoked activity.** A: Epileptiform activity is evoked by electrical stimulation. The mean cross-map function and the SE over the slices ( $n=5$ ) are shown. The LFP clearly drives the IOS with short time delay: the causality peak is observed at 1 s delay (black line). The causality peak in the IOSh→LFP direction with positive (anti-causal) time delay shows delayed correlation: the IOSh follows the LFP with 3 s delay (red line). B: Cross-correlation function between LFP and IOSh (blue line) and between the LFP and the time derivative of the IOSh (black line). The peaks of the LFP-IOSh cross-correlation function does not corresponds to the causality peaks, while the derivative of the IOSh correlates with the LFP at 0 time lag, which is closer to time lag of the causality. C and D: Same as in A and B, but in epileptic activity was evoked by  $Mg^{2+}$ -free artificial cerebrospinal fluid, mean and SE ( $n=3$ ). Similarly, the causality analysis implies unidirectional effect: the LFP causes the IOSh, but with only 0.5 s time delay, which corresponds to the negative peak of the cross-correlation function between the derivative of the IOSh and the LFP power (D black line). E and F: Same as A and B, but epilepsy was evoked by 4-aminopyridyn (4AP) mean and SE ( $n=4$ ). Both the causality and the correlation peaks are smaller but their temporal relations are the same. The causality peak coincides with the correlation peak between the LFP and the derivative of the IOSh.

implemented in Scilab and applied to reveal the causality between the 1 hour long LFP and the IOSh recordings. Applying the time-delayed CCM analysis to the downsampled LFP power and to the IOSh recordings from each slice in the reflected light setup, we constructed the cross-map functions, which express the strength of the causal connections in both directions, as a function of the time delay between the two time series (Fig. 30). The resulting cross-map functions were averaged for slices sharing the same induction process: electric stimulation,  $Mg^{2+}$ -free solution and 4AP treatment.

The causality analysis revealed similar structure in all the three cases. The cross-map functions have two significant peaks: a sharper peak for the LFP→IOSh causal direction, where the LFP precedes the IOSh with 1 s in case of electric stimulation and with 0.5 s in  $Mg^{2+}$ -free and 4AP cases (Fig. 30 A, C, E black lines, peaks on the negative half of the x axis) and a wider peak in the IOS→LFP direction, where IOSh follows LFP with 2.5 s time delay in the electric stimulation case and 1.5 s delay in the  $Mg^{2+}$ -free and 4AP cases (Fig. 30 A, C, E red lines, peaks on the positive half of the x axis).

In all cases, the peaks of the IOSh→LFP causality function are located at an anti-causal time delay, which means, that the presumed cause, the IOSh, in these cases, follows the presumed effect (the LFP) in time. Assuming that there is no difference in the observational delay, this is clearly impossible if the causal premise is correct. But, how can these anti-causal peaks be interpreted? Sugihara's CCM search for the fingerprints of the cause in the caused time series, thus a delayed CCM peak, means that the past cause can be reconstructed best from a later section of the caused time series. In our case, the real cause, the past LFP, can be reconstructed from the IOSh 0.5-1 s later. In the reverse (IOSh→LFP) direction, the algorithm checks, if the IOSh can be determined from the LFP. Thus the anti-causal peaks in the IOSh→LFP direction mean that the future of the IOSh can be determined based on the earlier LFP. We expect the appearance of such an anti-causal peak if the caused dynamics are more deterministic and non-chaotic, thus their future can be determined from the cause for a long time.

Thus, the conclusion of the causality analysis is that the LFP drives the IOSh activity, which follows quite predictably the LFP dynamics. There were no significant peaks on the negative half axis of the cross-map functions in the IOSh→LFP direction, which means that we did not find evidence for a feedback effect from the IOSh to the LFP in the examined range of time delays.

As the cross-map functions showed similar structures in all the three cases, we can assume that although the mechanisms generating the epileptic activity are different in the three cases, the causal link, thus the underlying mechanism, connecting the LFP to the IOSh may be similar.

Theoretically, the cross-map between two fully deterministic systems should reach the

amplitude 1 for data series long enough. Thus, maxima smaller than 1 could be the effect of noise (which is non-deterministic) and that the recordings are not long enough. We found, that the amplitude of the causality peak was highest for the electrical stimulation case (mean  $0.62 \pm 0.09$  SE), smaller for the  $Mg^{2+}$ -free (mean  $0.44 \pm 0.16$  SE) and smallest for the 4AP evoked activity (mean  $0.3 \pm 0.11$  SE). The difference within the amplitudes could be the result of the different activity level (less discharges) within the cases as well as the different signal to noise ratio.

#### 4.4.3 Causality versus correlation

We have compared the cross-map function to the traditional cross-correlation function. The cross-correlation function between LFP power and IOSh also showed similar structure in all cases, albeit with some differences (Fig. 30 B, D, F blue lines). All the three correlation functions had a significant negative peak on the negative half axis (corresponding to the LFP lead) although at different delays: at -4.5 s in case of electric stimulation (mean  $-0.36 \pm 0.007$  SE), at -2.5 s in the  $Mg^{2+}$ -free case (mean  $-0.21 \pm 0.06$  SE) and at -1 s in the 4AP case (mean  $-0.16 \pm 0.016$  SE). The cross-correlation function showed a second significant but positive peak on the positive half axis only at the  $Mg^{2+}$ -free case (mean  $0.11 \pm 0.004$  SE), but increased monotonically in the two other cases. Considering, that for very large time delays, the two data series become independent, thus the cross-correlation function should decay to zero, this monotonic increase implies the existence of a second even wider positive peak shifted far into the positive direction in these cases as well.

Comparison of the cross-correlation functions (Fig. 30 B, D, F blue lines) to the LFP - IOSh causality function (Fig. 30 A, C, E black lines) shows, that none of peaks of the cross-correlation functions corresponds to the real delay of the causal effect represented by the peaks of the cross-map functions. We concluded that the real causal effect is not clearly reflected in the peaks of the cross-correlation functions in these cases.

As the short delay ( $\delta < 0.5$  s-1 s) causal effect from the LFP to the IOSh is not accompanied by high correlation with similar short delay, the effect from the LFP to the IOSh should take a form, which can not be well approximated with the linear dependence. One possibility is that, instead of the IOSh, the derivative of the IOSh depends on the LFP power. This assumption is supported by the shape of the cross-correlogram: highest steepness is close to zero time delay.

Thus, we also calculated the cross-correlation function between the LFP power and the time derivative of the IOSh signal. We found, that the peaks of the causality (Fig. 30 A, C, E black lines) well matches to the negative peaks of the LFP-dIOSh/dt cross-correlation function (Fig. 30 B, D, F black lines) in all the three cases. This implies the possibility, that the temporal derivative of the IOSh depends on the LFP power during the epileptiform

discharges in the tissue.

#### 4.4.4 Autonomous dynamics of IOSh without discharges

According to the above results, a causal link clearly exists between LFP and IOSh. However, between the burst discharges, the IOSh decays towards the baseline, which, in lack of observable electric activity, seems to be a result of autonomous dynamics (Figs. 28 E and 29). In order to determine the form of the decay functions, we collected the IOSh time series during those interburst periods which were longer than 25 s from all slices. The amplitude of the IOSh was normalized to 1 for each period and averaged over all bursts within a slice. The logarithm of the absolute value of the IOSh showed clear linear temporal dependence, during large part of these interburst periods in all cases, which is the hallmark of exponential decay dynamics. Thus, a linear function was fitted to the logarithm of the mean IOSh values between 2.5 and 25 s for each slices. Finally the mean and the SD of the decay time constant were calculated for the three forms of the epileptic activity. The mean decay time constant was the shortest in the  $Mg^{2+}$ -free evoked activity with  $\tau_1 = 30.3 \pm 3.2$  s (11, 9 and 11 intervals from 3 slices); the decay was longer in the 4AP treated slices:  $\tau_1 = 54.9 \pm 18.7$  s (15, 7, 7, 11 intervals from 4 slices) and the longest for the electrically stimulated slices:  $\tau_1 = 73 \pm 19.2$  s (25, 25, 6, 15, 6 intervals from 5 slices). Three examples of the exponential fits are shown in Fig. 31, one for each of the three forms of evoked epileptic activity.

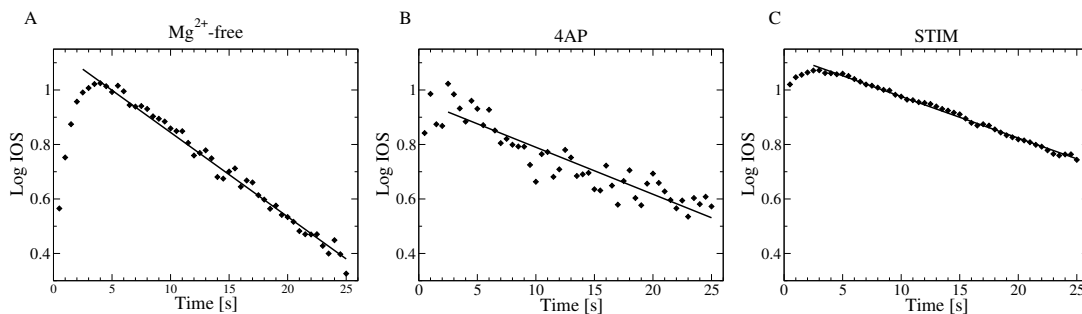


**Figure 31: Three examples of the exponential decay of IOSh mean absolute value between discharges.** The mean normalized IOSh amplitudes after initiation of epileptiform bursts at 0 s on Lin-Log plots (diamonds) and the fitted exponentials (solid lines) are shown. In all the three cases the decay closely followed the exponential rule between 2.5 and 25 s. The characteristic decay time of the fitted exponentials in these examples were (A) 32.3 s in the  $Mg^{2+}$ -free case; (B) 58 s in the 4AP case and (C) 65.62 s in the electrically stimulated case.

#### 4.4.5 Reconstruction of IOSh based on LFP

By combining these observations, a simple formula is inferred, approximately describing the dependency of the IOSh on the LFP power in the form of a differential equation:

$$\frac{dIOSh}{dt} = W(t) * LFP^2(t) - \frac{IOSh}{\tau_1} \quad (84)$$

where  $W(t)$  scales the causal effect from LFP to IOSh. Here we assumed, that the decay constant  $\tau_1$  is constant through whole recordings. This simple model has been used to estimating the IOSh signal based on the known LFP power in the  $Mg^{2+}$ -free and 4AP elicited cases, where the epileptiform activity has developed autonomously, without external stimulation. The reconstructed IOSh were filtered similarly by subtracting the moving window average as the real observed signal and were compared to it. The optimal model parameters were determined by numerical optimization, minimizing the Root Mean Square Error (RMSE) of the IOSh reconstruction.

First,  $W(t)$  was set to a constant value according to the negative peak of the correlation between LFP power and the time derivative of the IOSh, but we found, that the residual error of the IOSh reconstruction showed clear temporal tendency in majority of the recordings. Thus we introduced a time dependent weight factor  $W(t)$  in form of an exponential decay:

$$W(t) = W_0 e^{-\frac{t}{\tau_2}} \quad (85)$$

The optimal  $W_0$  and the  $\tau_2$  time constant was determined by a grid search. The optimization converged to a minimum of the RMSE in 6 cases out of the 7 slices (2 out of 3  $Mg^{2+}$ -free and all the 4 4AP slices). Thus we concluded, that the exponentially decaying effective connection strength was a reasonable description of the long term temporal development in the majority of the cases. The optimal time constant were found to be  $\tau_2 = 2839 \pm 582$  s (mean and SD) for the  $Mg^{2+}$ -free cases and  $\tau_2 = 2061 \pm 1121$  s (mean and SD) for the 4AP cases.

The comparisons between the reconstructed and the observed IOSh show that reconstruction follows closely the actual observations during the 1 h long experiment, through several dynamical changes in both the  $Mg^{2+}$ -free and the 4AP cases. An example for  $Mg^{2+}$ -free elicited activity is shown in Fig. 32 and another for 4AP in Fig. 33. Note, the large difference between the two dynamics and waveshape.

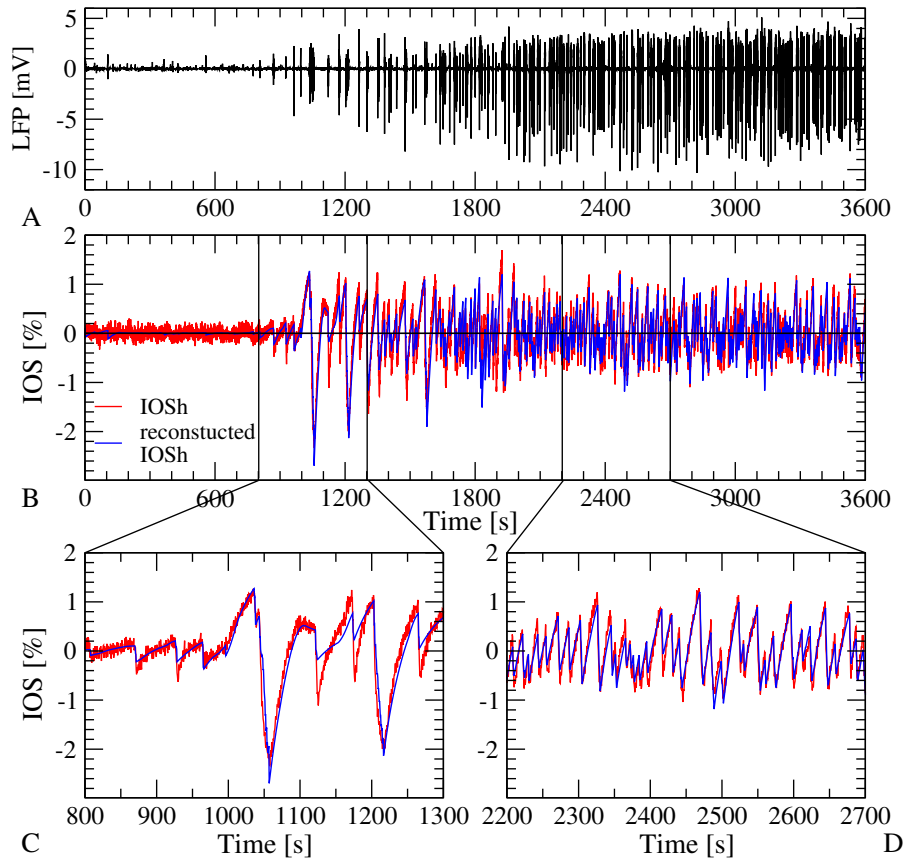


Figure 32: **Reconstruction of IOSh based on LFP in  $Mg^{2+}$ -free case.** A: The recorded LFP signal showing the epileptiform activity induced by  $Mg^{2+}$ -free solution (black). B: Comparison of the high pass filtered IOSh (red) and the reconstructed IOSh (blue) based on the LFP signal. C and D: Zoom of the original and reconstructed IOSh signal in the early and late phase of the epileptic activity. Our simple model reconstructs the IOSh signal based on the LFP with high precision, through the 1 hour long experiment.

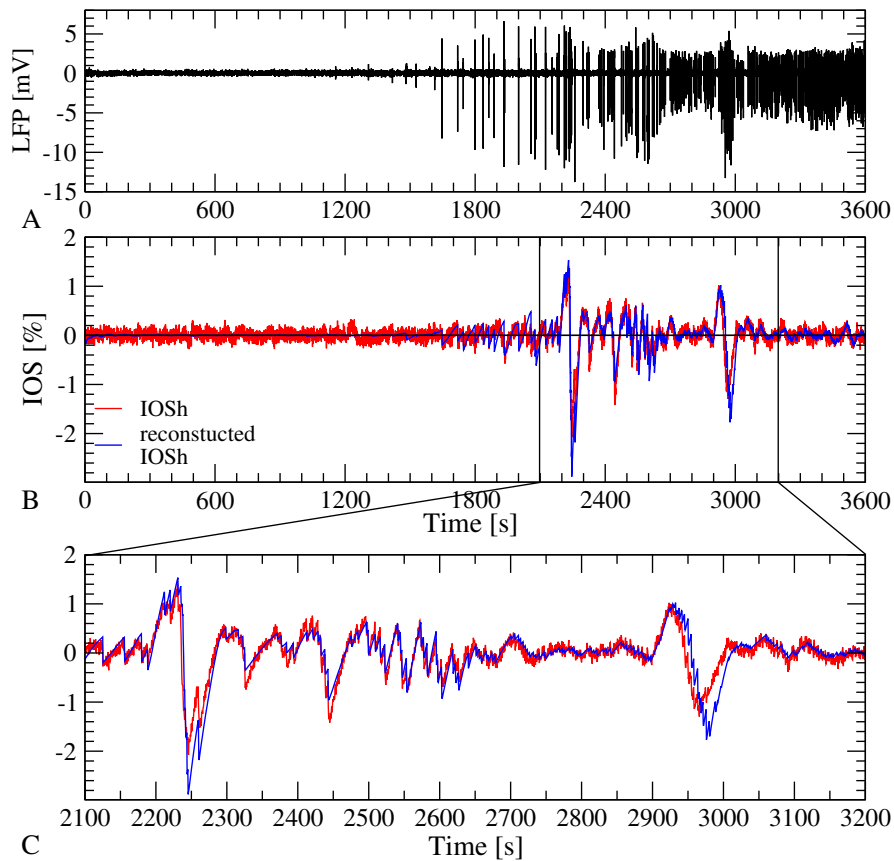


Figure 33: **Reconstruction of IOSh based on LFP in 4AP case.** A: The recorded LFP signal showing the epileptiform activity induced by 4AP treatment (black). B: Comparison of the high pass filtered IOS (red) and the reconstruction (blue) based on the LFP signal. C: Zoom of the original and reconstructed IOSh signal shows clear dynamical changes, but our simple model reconstructs the IOSh signal based on the LFP with high precision, through the 1 hour long experiment.

#### 4.4.6 Simulations

Based on the derived formula for the LFP→IOSh dependence, simulations have been run in order to cross-validate the causality analysis results.

The simulations consist of a driving variable ( $X$ ), a logistic chaotic oscillator, from which a spike-like discharge activity is derived, by raising it to the 4<sup>th</sup> power, and a second driven variable exhibiting linear dynamics and exponential decay corresponding to the inferred model of the IOSh:

$$X(t + 1) = 3.8X(t)(1 - X(t)) \quad (86)$$

$$IOSh(t + 1) = (1 - dt/\tau_1)IOSh(t) - X^4(t - \delta) \quad (87)$$

The time delay  $\delta$  of the driver effect have been varied and the causal relationship have been measured by the cross-map function. These simulations showed, that the exact value of the time delay between the two variables was inferred precisely by the peaks of the cross-map function, and even the shape of the cross-map function and the anti causal peak in the IOSh→LFP direction resembles very much to the observed one (Fig. 34). Based on these simulations, we can conclude that the time delay of the causal effect can be determined precisely by this method, in this case.

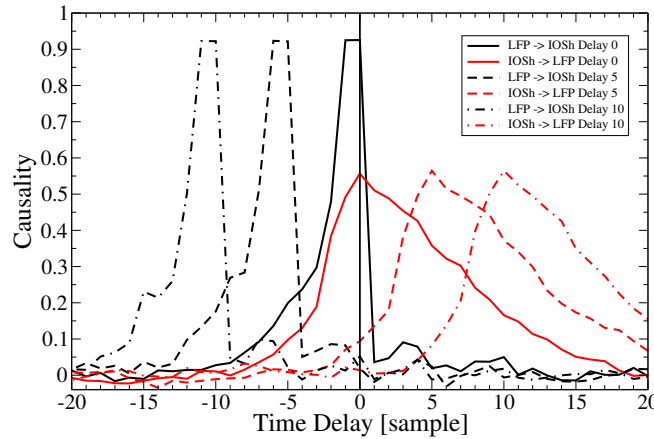


Figure 34: **Test of causality analysis on simulated test data.** Simulated IOSh have been driven by the simulated LFP with three different time delays in the three cases:  $\delta = 0$ , 5 and 10 time samples. The positions of the peaks of the black lines (solid, dashed and dash-dot) on the negative half of the x axis clearly mark both the direction and the delays of the driving force. The peaks of the red lines at positive delay values show, that the IOSh follows predictably the LFP.

## 5 Discussion

### 5.1 About the clusters of cell pedicules in the OPL of the human retina

We clustered retinal cone pedicules according to pedicule area size, pedicule convex hull area size and connexin36 plaque number by fitting a lognormal mixture model on the data. The optimization was carried out by the EM algorithm and we utilized the Bayesian information criteria to select the optimal number of clusters.

The results were that two clusters were the optimal number of components for pedicule sizes and three clusters were the optimal for the convex hull area and the plaque number data. From the latter cases, one of the three clusters contained very small values, hinting that they consist of small fragments, not morphologically distinct groups. This means that in general, two meaningful clusters were found by the mixture model on all features respectively. Also, one can speculate that the two groups can be mapped to the distinct S and M/L cone population of the retina.

### 5.2 About unicorns and the Temporal Outlier Factor

We introduced a new concept of anomalous event called unicorn and we have defined the Temporal Outlier Factor to quantify this concept. Unicorns are the unique states of the system, which were visited only once. A new anomaly concept can be valid only if a proper detection algorithm is provided. We demonstrated that TOF is a model-free, non-parametric, domain independent anomaly detection tool, which can detect unicorns. TOF measures the temporal dispersion of state space neighbors for each point. If state space neighbors are temporal neighbors as well, then the system has never returned to that state, therefore it is a unique event ie. a unicorn.

The unicorns are not just outliers in the usual sense, they are conceptually different. As an example of their inherently different behavior, one can consider a simple linear data series: As all of its points are visited only once and the system never returned to either one of them, all of the points of that line will be unique events. Whilst this property may seem counter-intuitive, it ensures that our algorithm finds unique events regardless of their other properties, such as amplitude or frequency. This example also shows, that the occurrences of unique events are not necessarily rare: actually, all the points of a time series can be unique. This property clearly differs from other anomaly concepts: most of them assume that there is a normal background behavior which generates the majority of the measurements and outliers form only a small minority.

Detection performance comparison of TOF and LOF on different simulated datasets highlighted the conceptual difference between the traditional outliers and the unique events

as well. LOF detected classic outliers based on the drop in the local density, therefore it detected those anomalies well, which generated low density sets in the state space. The short segment of tent map within a logistic map background and the higher frequency beating of tachycardia within the background of the normal heart rhythm generated such low density sets. However, depending on the parameters, linear segment anomalies can form higher, lower or equal density sets compared to the background. In our simulations the linear anomaly formed similar density sets to the logistic background and much higher density states than the random walk background, which made them invisible for the LOF. As our simulations showed, TOF with the same parameter settings was able to find both higher and lower density anomalies, based on the sole property that they were unique events. As a striking difference to the outlier concept, in the case of the detrended random walk dataset with linear anomaly, the anomalous points not only formed a higher density set, but were located right in the center of the normal data distribution. In our tests, TOF showed good precision and recall on simulated dynamical and stochastic anomaly datasets, as well as on simulated ECG time series. The algorithm has very low false detection rate, but not all the outlier points were found or not all the points of the event were unique. As an example, QRS waves of ECG simulations do not appear to be different from normal waves, hence the algorithms did not find them.

It was also shown in the simulations with multiple events that TOF only detects unique events or unicorns. However when two outliers were so close to each other that the elapsed time was in the same order of magnitude as the threshold event length, then TOF identified both events as outliers, since the two events formed one longer one. On the contrary, when the elapsed time between outlier segments is much greater than the threshold event length, TOF detected none of the events. In this latter case, ROC AUC values were much smaller than by-chance meaning, that TOF score during the events was higher than average score over the whole time period.

On the polysomnographic dataset, the anomaly was known from the parallel respiratory signal, but there was no evident change on the ECG signal. It was shown that TOF and LOF can both detect parts of the apnoe event from an ECG measurement. TOF found the actual stalling period of respiration, but LOF detected the preceding irregular breaths. While ECG analysis mostly concentrates on the temporal relations of the identified wave components, here we apply the detection methods to the continuous ECG data. Interestingly, TOF marked mainly the T waves of the heart cycle as anomalous points. T-waves are signs of the ventricular repolarization and are known to be largely variable, thus they are often omitted from the ECG analysis. This example showed, that they can carry relevant information as well.

On the gravitational wave dataset both TOF and LOF was able to detect the merger

GW150914 event, however TOF needed lower embedding dimension ( $E = 6$ ) and neighbor number ( $k = 11$ ) than LOF ( $E = 11, k = 100$ ). Clearly, the specific, model-based detectors that were originally used to recognize gravitational waves are much more sensitive to the actual waveforms of merger black holes or neutron stars than the model-free method that we implemented [36]. However, model-free methods can have a role in finding signs of events with unpredicted waveforms such as gravitational waves of supernovas.

Whilst LOF showed no specific detection pattern, TOF detected two rising periods on the temporal derivative of the USD LIBOR dataset: one preceding the 2008 crisis and another one from 2012 onwards. Both detected periods showed unique dynamics that differ from each other as well. The period between 2005-2007 can be considered unique in many ways; not only was there an upswing of the global market, but investigations revealed that several banks colluded in manipulation and rigging of LIBOR rates in what came to be known as the infamous LIBOR scandal. [134]. Note, that this was not the only case, when LIBOR was manipulated: During the economic breakdown in 2008 the Barclays Bank submitted artificially low rates to show healthier appearance [135–137]. As a consequence of these scandals, significant reorganization took place in controlling LIBOR calculation, starting from 2012.

To sum it up, gravitational waves of the merger black-holes on the filtered dataset formed a traditional outlier which was well detectable by both the TOF and LOF, while LIBOR exhibited longer periods of unique events only detectable by the TOF. Hypopnoe generated a mixed event on ECG, where the period of irregular breathing formed outliers and was detectable by LOF, while the apnoe generated a unique event on the ECG during failed respiration detectable only by the TOF.

Comparing TOF and LOF proved that temporal scoring has advantageous properties and adds a new aspect to anomaly detection. One advantage of TOF can be experienced when it comes to threshold selection. Since the TOF score has time dimension, an actual threshold value means the maximal expected length of the event to be found. Also, on the flip-side the neighborhood size  $k$  parameter sets the minimal event length. Because of these properties, domain knowledge about possible event lengths renders threshold selection to a simple task. An other advantage of TOF is from the computational point of view: the method performs optimally on small embedding dimensions and neighborhood sizes, which makes computations faster and less memory hungry.

Time indices of  $k$  nearest neighbors have been previously utilized differently in non-linear time series analysis to diagnose nonstationary time series [39, 40, 138], measure intrinsic dimensionality of system's attractors [41–43], monitor changes in dynamics [44] and even for fault detection [45]. Rieke et al. utilized very resembling statistics to TOF: the average absolute temporal distances of  $k$  nearest neighbors from the points. However

they analyzed the distribution of temporal distances to determine nonstationarity and did not interpret the resulting distance scores locally. Gao & Hu and Martinez-Rego et al. used recurrence times ( $T_1$  and  $T_2$ ) to monitor dynamical changes in time series locally, but these statistics are not specialized for detecting extremely rare unique events. TOF utilizes the temporal distance of  $k$  nearest neighbors at each point, thus provides a locally interpretable outlier score. This score takes small values when the system visits an undiscovered territory of state-space for a short time period, therefore it is suitable to detect unicorns.

Future directions to develop TOF would be to form a model which is able to represent uncertainty over detections by creating temporal outlier probabilities just like Local Outlier Probabilities [139] created from LOF. Moreover, an interesting possibility would be to make TOF applicable also on different classes of data, for example on point processes like spike-trains, network traffic time-stamps or earthquake dates.

### 5.3 About the cmFSA algorithm

We revisited and improved the manifold adaptive FSA dimension estimator. We computed the probability density function of local estimates if the local density was uniform. From the pdf, we derive the maximum likelihood formula for intrinsic dimensionality.

We proposed to use the median of local estimates as a global measure of intrinsic dimensionality, and demonstrated that this measure is asymptotically unbiased.

We tackled edge effects with a correction formula calibrated on hypercube datasets. We showed that the coefficients are sample-size dependent. Camastra and Vinciarelli [63] took a resembling empirical approach, where they corrected correlation dimension estimates with a perceptron, calibrated on  $d$ -dimensional datasets. Our approach is different, because we tried to grasp the connection between underestimation and intrinsic dimensionality more directly, by showing that the dimension-dependence of the relative error is exponential. The calibration procedure of DANCo may generalize better, because it compares the full distribution of local estimates rather than just a centrality measure [61]. Also, we are aware that our simple correction formula overlooks the effect of curvature and noise. We tried to address the former with the choice of minimal neighborhood size ( $k = 1$ ), thus the overestimation effect due to curvature is minimal. Additionally, the effect of noise on the estimates is yet to be investigated. There are several strategies to alleviate noise effects such as undersample the data while keeping the neighborhood fixed [62], or using a bigger neighborhood size, while keeping the sample size fixed. Both of these procedures make the effect of curvature more severe, which makes the dimension estimation of noisy curved data a challenging task.

We benchmarked the new mFSA and corrected-mFSA method against Levina-Bickel

estimator and DANCo on synthetic benchmark datasets and found that cmFSA showed comparable performance to DANCo. For many datasets, R-DANCo overestimated the intrinsic dimensionality, which is most probably due to rough default calibration [64]; the matlab implementation showed the best overall results in agreement with Campadelli et al [55]. This superiority was however dataset-specific: cmFSA performed genuinely the best in 4, DANCo in 2 out of the 15 benchmark datasets (with 7 ties, Table 4). Also, cmFSA showed better overall error rate than DANCo. Combining the performance measured by different metrics, we recognise that cmFSA found the true intrinsic dimension of the data in more cases, but when mistaken, it makes relatively bigger errors compared with DANCo.

The mFSA algorithm revealed diverse changes in the neural dynamics during epileptic seizures. In normal condition, the gradient of dimension values on the cortical grid reflects the hierarchical organization of neocortical information processing [140]. During seizures, this pattern becomes disrupted pointing to the breakdown of normal activation routes. Some channels showed lower dimensional dynamics during seizures; that behaviour is far from the exception: the decrease in dimensionality is due to widespread synchronization events between neural populations [141], a phenomenon reported by various authors [49, 142, 143]. These lower-dimensional areas are possible causal sources [24, 52, 54] and candidates for being the seizure onset zone. Interestingly, Esteller et al found, that the Higuchi fractal dimension values were higher at seizure onset and decreased to lower values as the seizures evolved over time [144]. We found, that most areas showed decreased dimensionality, but few areas also showed increased dimension values as seizure takes place. This may suggest that new - so far unused - neural circuits are activated at seizure onset; whether this circuitry contributes to or counteracts epileptic seizure is unclear.

## 5.4 About IOS and its relation to LFP

Two components of the IOS signal have been distinguished during induced epileptic activity in *in vitro* cortical slices. They were different not only in their time scale, but presumably the underlying mechanisms as well. The faster, activity-dependent component (IOSh) was positive in transmitted light and negative in reflected light measurements. It can be interpreted as the decrease of the scattering of the tissue, caused by swelling of the cells due to the activation and underlying movement of ions across the membranes followed by water [145]. In this processes not only the neurons but also the glial cell might play significant role [146, 147]. The later types of cells are more prone to swell, but the glial reaction is preceded by neuronal activation [148]. During this activation, an abundance of excitatory transmitters are released and intensive ionic movements take

place increasing significantly the extracellular  $K^+$  concentration, which is then buffered in glial cell and causes its swelling [149].

The slower component (IOSI), however was negative in both transmitted and reflected experiments, thus it can be attributed to the increase of the absorption of the tissue. While different components of the in vitro, blood-free IOS signal were distinguished previously [101, 105, 150] all of them were attributed to the change of the scattering of the tissue, thus none of them corresponds to the observed increase of the absorption. Cell death could be one of the possible reasons of this phenomena, however, as the electrical responsiveness of the slices haven't changed significantly during the recording, we can suppose, that cellular destruction is not necessarily substantial. In order to verify the possible role of the cell death in the IOSI component, its irreversibility should be checked.

A candidate mechanism, showing that absorption plays role in IOS generation, was presented by Mané and Müller [151]: Multispectral analysis of the IOS showed a significant dip in the IOS spectrum at 440 nm wavelength during spreading depression. This absorption line, referred to as Soret band, is a mark of the absorption of porphyrins. The changes of the light absorption by cytochromes appear at this wavelength, thus, reduction of cytochromes as well as its unpacking from the mitochondria could increase the absorption of the tissue.

The directed causal relationships were examined between the LFP and the IOSh by Sugihara's causality analysis method, the convergent cross mapping. We have found a strong, unidirectional, delayed causal effect from LFP to IOSh with 0.5-1 s delay, without signs of feedback from the IOSh to the LFP. However, it is also showed, that a "shadow peak" in the IOSh→LFP direction appeared at anticausal time delays.

In general, we found, that the delay of the causality peaks significantly affects the interpretation of the results. Assuming no observational delay, two different cases should be distinguished: the peak of the cross-map functions, located on the negative half of the time axis, should be considered as a sign of the real causal effect, since the cause preceded the consequence. However, the peaks on the positive half-axis should be interpreted, as a sign of the delayed prediction, ie. the caused time series follows the effect of the cause faithfully with some delay, thus not only the cause can be reconstructed from the caused time series (this corresponds to the peaks on the negative axis), but the caused time series can be predicted from the cause as well. While the peaks on the negative half of the delay axis are signs of the causality in terms of the Sugihara et al. [88], the peaks on the positive half-axis correspond more to the predictive causality according to the Wiener-Granger principle [79, 81].

In our case, due to the relatively smooth and continuous nature of the IOSh signal, the IOSh→LFP causality peak on the anti causal half-axis become wider, and the "shoulder"

of that peak produced relatively high causality values at the negative half of the time lag axis as well. If only the instantaneous CCM were calculated, the IOSh→LFP causality coefficients would have similar values to the LFP→IOSh drive, thus one would erroneously conclude, that a significant feedback exists in the IOSh→LFP direction as well. Observation of the full, time dependent, cross-map function reveals, that the relatively high causality at zero time lag in the IOSh→LFP direction is only a side effect of a peak in the anti-causal regime. We concluded, that the delay dependent calculation of the CCM is important not only to determine the delays of the causal effects, but to find the correct causal directions and strengths as well.

The causality structure was very similar in all the three induction methods of the epileptic activity: electrical stimulation,  $Mg^{2+}$ -free solution or 4AP induction, although the causal connection strength was stronger in the stimulated and weaker in the presence of 4AP than in  $Mg^{2+}$ -free solution. The similarity of the causal structures may imply similar underlying mechanisms in all three cases, meaning, that the generation of the IOSh component is independent of the method of induction.

It was demonstrated, that although the cross-correlation functions showed peaks, those peaks did not reflect the actual causal dependency in these cases. Instead, the temporal derivative of the IOSh was correlated with the LFP power at the time delay of the actual causal peak.

During the interdischarge intervals, the IOSh signal decays towards the baseline exponentially, without significant causal influence from the LFP, which implies a linear autonomous dynamics.

To sum up our observations on the dynamics of IOSh, a simple model has been set up to describe the dependency of the IOSh on the LFP power. The model allowed the reconstruction of the IOSh based on the LFP signal. Model fitting showed, that during the slow development of the epileptiform activity, the effective causal connection strength slowly decreased. This decrease could be well approximated by an exponential decay. Quantitatively good reconstruction of IOSh, based on the LFP signal by our model during the 1 h long recordings, supports the results of the causality analysis as well.

The model provided us the possibility to cross-validate the causality analysis, with known causal dependency and effect delays. The causality analysis on the simulated data series resulted in very similar cross-map functions on the model as it was found on the measurements: the peaks on the negative half of the time delay axis precisely marked the direction and the delay of the simulated causal effects, while “shadow peaks” were generated on the positive, anti-causal half of the delay axis. The only slight difference was that in case of simulated data series, the shadow peaks position was always symmetric to the main peak on the delay axis, while in case of the measurements, the “shadow peak”

showed larger lags.

Our results on LFP→IOSh unidirectional causality do not exclude the possible presence of causal connections on a slower time scale either in the reverse direction or in the same direction but between the observable epileptic bursts, where we now observe only the autonomous dynamics of the IOSh. Inference of possible interactions on slower time scale now excluded by filtering out the slower component (IOSl) which was necessary to make the IOSh available for the causal analysis. The causal relation between the LFP and the slower, IOSl component could not be determined based on these measurements, because the IOSl does not satisfy the necessary conditions. The application of the CCM method requires, that the system went through multiple times on its attractor. This condition is satisfied for the IOSh component, but not for the IOSl, which exhibits only one sweep through the state space, during these experiments. We can suppose that IOSh is determined by relatively quick cellular processes, while IOSl is determined by slow extracellular space processes [152].

The application of CCM for LFP and IOSh demonstrates, that the significantly different inherent speed and sampling rate of the signals, and the necessary downsampling does not preclude the determination of the causal relationships, thus raises the possibility of application of the new method to other signal modalities with different speed, such as fMRI and EEG as well.

## **6 Conclusions**

### **6.1 Determination of clusters based on cell pedicule-features**

As part of characterization of the connexin36 gap junctions in the human outer retina I have determined the optimal number of cone pedicule clusters by fitting lognormal mixture models supplemented with model selection based on Bayesian information criterion. I showed, that two main subpopulaton of cell-pedicules can be differentiated based on either pedicule area size, subpedicule convex hull area size and connexin36 plaque numbers per subpedicules.

### **6.2 Temporal Outlier Factor to detect unique events**

Recognition of anomalous events is a challenging but critical task in many scientific and industrial fields, especially when the properties of anomalies are unknown. I introduced a new anomaly concept called “unicorn” or unique event and presented a new, model-independent, unsupervised detection algorithm to detect unicorns. I created the Temporal Outlier Factor (TOF) to measure the uniqueness of events in continuous data sets from dynamic systems. The concept of unique events differs significantly from traditional outliers in many aspects: while repetitive outliers are no longer unique events, a unique event is not necessarily outlier in either pointwise or collective sense; it does not necessarily fall out from the distribution of normal activity. I examined the performance of the algorithm by recognizing unique events on different types of simulated data sets with anomalies and I compared the results with the standard Local Outlier Factor (LOF). TOF had superior performance compared to LOF even in recognizing traditional outliers and it also recognized unique events that LOF did not. I illustrated the benefits of the unicorn concept and the new detection method by example data sets from very different scientific fields. The TOF algorithm successfully recognized unique events in those cases where they were already known such as the gravitational waves of a black hole merger on LIGO detector data and the signs of respiratory failure on ECG data series. Furthermore, unique events were found on the LIBOR data set of the last 30 years.

### **6.3 The corrected median Farahmand-Szepesvari-Audibert intrinsic dimensionality estimator**

Data dimensionality informs us about data complexity and sets limit on the structure of successful signal processing pipelines. I revisited and improved the manifold adaptive Farahmand-Szepesvari-Audibert dimension estimator, making it one of the best nearest

neighbor-based dimension estimators available. I computed the probability density function of local dimension estimates, if the local density was taken uniform. Based on the probability density function, I proposed to use the median of local estimates as a basic global measure of intrinsic dimensionality, and I demonstrated the advantages of this asymptotically unbiased estimator over the previously proposed statistics: the mode and the mean. Additionally, from the probability density function, I derived the maximum likelihood formula for global intrinsic dimensionality, if the sampling is independent and identically distributed. I tackled edge and finite-sample effects with an exponential correction formula, calibrated on hypercube datasets. I compared the performance of the corrected median Farahmand-Szepesvari-Audibert estimator with kNN estimators: the Levina-Bickel estimator and two implementations of DANCo (R and MATLAB). I showed that the corrected median-Farahmand-Szepesvari-Audibert estimator beats the Levina-Bickel estimator and it is on equal footing with DANCo for standard synthetic benchmarks according to mean percentage error and error rate metrics. With the median-FS algorithm, I revealed diverse changes in the neural dynamics while resting state and during epileptic seizures. I identified brain areas with lower-dimensional dynamics that are possible causal sources and candidates for being seizure onset zone.

#### **6.4 Causal relationship between local field potential and intrinsic optical signal**

We examined the relationship between the local field potential (LFP) and the intrinsic optical signal (IOS) during induced epileptiform activity in *in vitro* cortical slices by the convergent cross-mapping causality analysis method. During the examinations, we have distinguished two components of the IOS signal: a faster, activity dependent component (IOSh) which changes its sign between transmitted and reflected measurement, thus it is related to the reflectance or the scattering of the tissue and a slower component (IOSl), which is negative in both cases, thus it is resulted by the increase of the absorption of the tissue. We have found a strong, unidirectional, delayed causal effect from LFP to IOSh with 0.5-1s delay, without signs of feedback from the IOSh to the LFP, while the correlation was small and the peaks of the cross correlation function did not reflect the actual causal dependency. Based on these observations, we set up a model to describe the dependency of the IOSh on the LFP power and IOSh was reconstructed, based on the LFP signal. By this study we demonstrated that causality analysis could lead to better understanding of the physiological interactions, even in case of two data series with drastically different time scales.

## 7 Summary

This work takes the reader into rock hard data analysis. First, we present an unsupervised investigation of static neuroanatomical structures in the human outer retina. Second, we turn to nonlinear time series analysis to detect anomalies and estimate intrinsic dimensions on various datasets. Finally, we investigate the relationship of the Local Field Potential and the Intrinsic Optical Signal measured on *ex vivo* mouse brain slices.

The human retina is an intricately organized structure, where photo-reception and the first steps of visual processing takes place. Gap junction-forming connexin36 plays a not straightforward role in this signalprocessing and anatomical description helps to explore this function. We applied unsupervised lognormal mixture models on connexin36-related features and determined two main clusters of cone pedicles in the OPL of the human retina.

Anomalies are rare and abnormal patterns and it is often critical to detect them. This is especially difficult when we do not know how the anomaly differs from normal activity. We developed a detection method that finds unique patterns that we have named “unicorns”. We showed that in addition to finding the anomalies that traditional methods do, it also recognizes anomalies that they do not. This is demonstrated on various data sets, from gravitational waves through ECG to economic indicators.

Data intrinsic dimensionality bears information about the redundancies and interactions between observed features. To access such information, we improved the manifold-adaptive FSA dimension estimator. We calculated the pdf of local estimates and proposed the median as an estimate of global intrinsic dimension. We corrected finite-sample and edge effects to increase the performance of the corrected mean FSA estimator to the level of DANCo, one of the most reliable state-of-the-art estimators. We investigated the intrinsic dimension of intracranial LFP measurements of a human subject with drug resistant epilepsy. During seizures, the right temporal cortex showed the most low-dimensional dynamics, which hints that it is a seizure onset zone.

We characterized the relation of LFP and IOS in *ex vivo* brain slices from mice during induced epileptic seizures. We found that the reflected IOS signal during epileptic activity consists of a slow trend and a fast component which showed association with the electric discharges of the LFP signal. We applied the delayed Convergent Cross Mapping method to reveal the causal relations between the recordings. We revealed that the LFP drives the IOSh activity, the time delay of the effect is half second. Finally, we inferred an empirical model to describe the the effect of the LFP power on the IOSh.

## 8. Összefoglalás

Ez a dolgozat statikus neuroanatómiai adatok nem-felügyelt analizisétől indulva, a nem-lineáris dinamikai rendszerek elméletének idősorokon való alkalmazásán keresztül jut el, agy-szeleteken mért optikai és elektromos jelek kapcsolatának feltárásáig.

Az emberi retina egy rendkívül jól szervezett anatómiai struktúra, mely a fényérzékelésért felelős és a vizuális feldolgozás első lépéseit is elvégzi. E jelfeldolgozásban játszanak nem teljes egészében feltárt szerepet a rés-kapcsolat-alkotó konnexinek, például a connexin36. Az anatómiai vizsgálat részeként lognormális keverék eloszlások illesztésével klasztereztük a konnexin-hordó csap szinaptikus talpak méret-eloszlását az OPL-ben készült metszeteken és ez alapján két fő csoportot tudtunk elkülöníteni.

Az anomáliák ritka és a szokványostól eltérő mintázatok, melyek észlelése nagy gyakorlati jelentőséggel bírhat. A dolgozat ezen részében kifejlesztettünk egy anomália detektáló módszert, ami extrém ritka egyedi események – úgynevezett unikornisok – megtalálását teszi lehetővé. Megmutattuk, hogy az algoritmus és unikornis-konceptió többlet értéket ad a tradicionális anomália-detekció irodalmához és demonstráltuk a módszer potenciális gyakorlati hasznát EKG, gravitációs hullám és LIBOR adatsorokon.

A dimenzió az adatok komplexitásának mértéke, utal a megfigyelt változók közötti redundanciákra és kapcsolatokra. Hogy ezen információhoz hozzáférjünk, a dolgozatban az FSA dimenzióbecslő algoritmust vizsgáltuk meg és fejlesztettük tovább. Kiszámoltuk a lokális becslések valószínűség-sűrűségfüggvényét és megállapítottuk, hogy az eloszlás mediánja megegyezik a dimenzióval. A véges mintaszám és a szél-hatás okozta torzítást kalibrációval korigáltuk, ez pedig egy szintre emelte az algoritmus teljesítményét DANCo-éval, mely az egyik legmegbízhatóbb dimenzióbecslő algoritmus. A medián FSA módszert ezután epilepsziás betegből származó intrakraniális potenciál adatokon alkalmaztuk és azt találtuk, hogy a rohamok alatt a jobb temporális kéreg mutatta a legalacsonyabb dimenziójú dinamikát, mely sejteti, hogy a terület rohamindulásért felelős zóna része.

Egér ex vivo agyszeleteken vizsgáltuk az extracelluláris potenciál és a saját optikai jel közti kapcsolatot indukált epilepsziás rohamok során. Megállapítottuk, hogy az epilepsziás aktivitás alatt reflektált optikai jel egy lassú trendből és egy gyors, az elektromos potenciálhoz kapcsolódó komponensből áll. A késleltetett konvergens keresztleképezési módszert alkalmazva kiderült, hogy az elektromos jel hajtja meg az optikait, és a hatás fél másodperc időkésséssel jelenik meg. A megfigyelések alapján egy empirikus differenciálegyenletben modelleztük a mezőpotenciál és az optikai jel kapcsolatát.

## 9 Bibliographies

- [1] Furshpan EJ, Potter DD. (1957) Mechanism of Nerve-Impulse Transmission at a Crayfish Synapse. *Nature*, 180: 342–343.
- [2] Watanabe A. (1958) The interaction of electrical activity among neurons of lobster cardiac ganglion. *Jpn J Physiol*, 8: 305–318.
- [3] Cruciani V, Mikalsen SO. (2006) The vertebrate connexin family. *Cell Mol Life Sci*, 63: 1125–1140.
- [4] Söhl G, Willecke K. (2003) An Update on Connexin Genes and their Nomenclature in Mouse and Man. *Cell Commun Adhes*, 10: 173–180.
- [5] Bloomfield SA, Völgyi B. (2009) The diverse functional roles and regulation of neuronal gap junctions in the retina. *Nat Rev Neurosci*, 10: 495–506.
- [6] Güldenagel M, Söhl G, Plum A, Traub O, Teubner B, Weiler R, Willecke K. (2000) Expression patterns of connexin genes in mouse retina. *J Comp Neurol*, 425: 193–201.
- [7] Petrasch-Parwez E, Habbes HW, Weickert S, Löbbecke-Schumacher M, Striedinger K, Wieczorek S, Dermietzel R, Epplen JT. (2004) Fine-structural analysis and connexin expression in the retina of a transgenic model of Huntington’s disease. *J Comp Neurol*, 479: 181–197.
- [8] Söhl G, Jousen A, Kociok N, Willecke K. (2010) Expression of connexin genes in the human retina. *BMC Ophthalmol*, 10: 27.
- [9] Bowmaker JK, Dartnall HJ. (1980) Visual pigments of rods and cones in a human retina. *J Physiol*, 298: 501–511.
- [10] Gray H, Lewis WH. *Anatomy of the human body*. Lea & Febiger, Philadelphia, PA, 1918.
- [11] Meiss J. (2007) Dynamical systems. *Scholarpedia J*, 2: 1629.
- [12] May RM. (1976) Simple mathematical models with very complicated dynamics. *Nature*, 261: 459–467.
- [13] Jakobson MV. (1981) Absolutely continuous invariant measures for one-parameter families of one-dimensional maps. *Commun Math Phys*, 81: 39–88.

- [14] Packard NH, Crutchfield JP, Farmer JD, Shaw RS. (1980) Geometry from a Time Series. *Phys Rev Lett*, 45: 712–716.
- [15] Takens F. Detecting strange attractors in turbulence. In: Rand D, Young LS (eds.), *Dynamical Systems and Turbulence*, 366–381. Springer Berlin Heidelberg, Berlin, Heidelberg, 1981.
- [16] Huke J. (2006) Embedding Nonlinear Dynamical Systems: A Guide to Takens’ Theorem. MIMS Preprint.
- [17] Hegger R, Kantz H, Matassini L, Schreiber T. (2000) Coping with nonstationarity by overembedding. *Phys Rev Lett*, 84: 4092–4095.
- [18] Ye H, Deyle ER, Gilarranz LJ, Sugihara G. (2015) Distinguishing time-delayed causal interactions using convergent cross mapping. *Sci Rep*, 5: 14750.
- [19] Schreiber T, Kaplan DT. (1996) Nonlinear noise reduction for electrocardiograms. *Chaos*, 6: 87–92.
- [20] Hamilton F, Berry T, Sauer T. (2016) Ensemble Kalman filtering without a model. *Phys Rev X*, 6: 011021.
- [21] Sugihara G, May R, Ye H, Hsieh Ch, Deyle E, Fogarty M, Munch S. (2012) Detecting causality in complex ecosystems. *Science*, 338: 496–500.
- [22] Benkő Z, Moldován K, Szádeczky-Kardoss K, Zalányi L, Borbély S, Világi I, Somogyvári Z. (2019) Causal relationship between local field potential and intrinsic optical signal in epileptiform activity in vitro. *Sci Rep*, 9: 1–12.
- [23] Selmeczy GB, Abonyi A, Krienitz L, Kasprzak P, Casper P, Telcs A, Somogyvári Z, Padisák J. (2019) Old sins have long shadows: climate change weakens efficiency of trophic coupling of phyto- and zooplankton in a deep oligo-mesotrophic lowland lake (Stechlin, Germany)—a causality analysis. *Hydrobiologia*, 831: 101–117.
- [24] Benkő Z, Zlatniczki Á, Stippinger M, Fabó D, Sólyom A, Eröss L, Telcs A, Somogyvári Z. (2018) Complete Inference of Causal Relations between Dynamical Systems. ArXiv.
- [25] Lorenz EN. (1963) Deterministic Nonperiodic Flow. *J Atmos Sci*, 20: 130–141.
- [26] Tucker W. (2002) A Rigorous ODE Solver and Smale’s 14th Problem. *Found Comut Math*, 2: 53–117.

- [27] Chandola V, Banerjee A, Kumar V. (2009) Anomaly detection: A survey. *ACM Comput Surv*, 41: 1–58.
- [28] Taleb NN. *The Black Swan: The Impact of the Highly Improbable*. Random House, New York, 2007.
- [29] Sornette D. (2009) Dragon-Kings, Black Swans and the Prediction of Crises. *International Journal of Terraspace Science and Engineering*, 2: 1–18.
- [30] Hodge VJ, Austin J. (2004) A Survey of Outlier Detection Methodologies. *Artificial Intelligence Review*, 22: 85–126.
- [31] Pimentel MAF, Clifton DA, Clifton L, Tarassenko L. (2014) A review of novelty detection. *Signal Process*, 99: 215–249.
- [32] Chalapathy R, Chawla S. (2019) Deep Learning for Anomaly Detection: A Survey. *ArXiv*, 1–50.
- [33] Kwon D, Kim H, Kim J, Suh SC, Kim I, Kim KJ. (2019) A survey of deep learning-based network anomaly detection. *Cluster Comput*, 22: 949–961.
- [34] Braei M, Wagner S. (2020) Anomaly Detection in Univariate Time-series: A Survey on the State-of-the-Art. *ArXiv*.
- [35] Qi D, Majda AJ. (2020) Using machine learning to predict extreme events in complex systems. *Proc Natl Acad Sci U S A*, 117: 52–59.
- [36] Abbott BP, et al. (2016) Observation of Gravitational Waves from a Binary Black Hole Merger. *Phys Rev Lett*, 116: 061102.
- [37] Breunig M, Kriegel HPH, Ng RR, Sander J, Breunig M, Kriegel HPH, Ng RR, Sander J. (2000) LOF: identifying density-based local outliers. *ACM sigmod record*, 29: 93–104.
- [38] Oehmcke S, Zielinski O, Kramer O. Event detection in marine time series data. In: Holldobler S Krotzsch M RSPR (ed.), *Lecture Notes in Computer Science*, volume 9324. Springer Verlag, 2015: 279–286.
- [39] Kennel MB. (1997) Statistical test for dynamical nonstationarity in observed time-series data. *Phys Rev E*, 56: 316–321.
- [40] Rieke C, Sternickel K, Andrzejak RG, Elger CE, David P, Lehnertz K. (2002) Measuring Nonstationarity by Analyzing the Loss of Recurrence in Dynamical Systems. *Phys Rev Lett*, 88: 244102.

- [41] Gao JB. (1999) Recurrence time statistics for chaotic systems and their applications. *Phys Rev Lett*, 83: 3178–3181.
- [42] Carletti T, Galatolo S. (2006) Numerical estimates of local dimension by waiting time and quantitative recurrence. *Physica A*, 364: 120–128.
- [43] Marwan N, Carmenromano M, Thiel M, Kurths J. (2007) Recurrence plots for the analysis of complex systems. *Phys Rep*, 438: 237–329.
- [44] Gao J, Hu J. (2013) Fast monitoring of epileptic seizures using recurrence time statistics of electroencephalography. *Front Comput Neurosci*, 7: 1–8.
- [45] Martínez-Rego D, Fontenla-Romero O, Alonso-Betanzos A, Principe JC. (2016) Fault detection via recurrence time statistics and one-class classification. *Pattern Recognit Lett*, 84: 8–14.
- [46] Grassberger P, Procaccia I. (1983) Measuring the strangeness of strange attractors. *Physica D*, 9: 189 – 208.
- [47] Houle ME, Schubert E, Zimek A. On the correlation between local intrinsic dimensionality and outlieriness. In: Marchand-Maillet S, Silva YN, Chávez E (eds.), *Similarity Search and Applications*. Springer International Publishing, Cham, 2018: 177–191.
- [48] Dlask M, Kukal J. Correlation Dimension Estimation from EEG Time Series for Alzheimer Disease Diagnostics. In: *Proceedings of the International Conference on Bioinformatics Research and Applications 2017 - ICBRA 2017*. ACM Press, 2017: 62–65.
- [49] Polychronaki GE, Ktonas PY, Gatzonis S, Siatouni A, Asvestas PA, Tsekou H, Sakas D, Nikita KS. (2010) Comparison of fractal dimension estimation algorithms for epileptic seizure onset detection. *J Neural Eng*, 7: 046007.
- [50] Sharma M, Pachori RB, Rajendra Acharya U. (2017) A new approach to characterize epileptic seizures using analytic time-frequency flexible wavelet transform and fractal dimension. *Pattern Recognit Lett*, 94: 172–179.
- [51] Acharya UR, Sree SV, Swapna G, Martis RJ, Suri JS. (2013) Automated EEG analysis of epilepsy: A review. *Know Based Syst*, 45: 147–165.
- [52] Sugiyama M, Borgwardt KM. Measuring statistical dependence via the mutual information dimension. In: *IJCAI International Joint Conference on Artificial Intelligence*. IEEE, 2013: 1692–1698.

- [53] Romano S, Chelly O, Nguyen V, Bailey J, Houle ME. Measuring dependency via intrinsic dimensionality. In: 2016 23rd International Conference on Pattern Recognition (ICPR), 4. IEEE, 2016: 1207–1212.
- [54] Krakovská A. (2019) Correlation dimension detects causal links in coupled dynamical systems. *Entropy*, 21: 818.
- [55] Campadelli P, Casiraghi E, Ceruti C, Rozza A. (2015) Intrinsic Dimension Estimation: Relevant Techniques and a Benchmark Framework. *Math Prob Eng*, 2015: 1–21.
- [56] Levina E, Bickel PJ. Maximum likelihood estimation of intrinsic dimension. In: Saul LK, Weiss Y, Bottou L (eds.), *Advances in Neural Information Processing Systems 17*. Neural information processing systems foundation, 2005: 777–784.
- [57] Ghahramani Z, Mckay D (2005). Comments on 'Maximum likelihood estimation of intrinsic dimension'.
- [58] Gupta MD, Huang TS. (2010) Regularized maximum likelihood for intrinsic dimension estimation. *ArXiv*.
- [59] Rozza A, Lombardi G, Ceruti C, Casiraghi E, Campadelli P. (2012) Novel high intrinsic dimensionality estimators. *Mach Learn*, 89: 37–65.
- [60] Bassis S, Rozza A, Ceruti C, Lombardi G, Casiraghi E, Campadelli P. A Novel Intrinsic Dimensionality Estimator Based on Rank-Order Statistics. In: Masulli F, Petrosino A, Rovetta S (eds.), *Clustering High-Dimensional Data*. Springer Berlin Heidelberg, Berlin, Heidelberg, 2015: 102–117.
- [61] Ceruti C, Bassis S, Rozza A, Lombardi G, Casiraghi E, Campadelli P. (2014) DANCo: An intrinsic dimensionality estimator exploiting angle and norm concentration. *Pattern Recognit*, 47: 2569–2581.
- [62] Facco E, D'errico M, Rodriguez A, Laio A. (2017) Estimating the intrinsic dimension of datasets by a minimal neighborhood information. *Sci Rep*, 1–8.
- [63] Camastra F, Vinciarelli A. (2002) Estimating the intrinsic dimension of data with a fractal-based method. *IEEE Trans Pattern Anal Mach Intell*, 24: 1404–1407.
- [64] Johnsson K, Sonesson C, Fontes M. (2015) Low Bias Local Intrinsic Dimension Estimation from Expected Simplex Skewness. *IEEE Trans Pattern Anal Mach Intell*, 37: 196–202.

- [65] Chelly O, Houle ME, Kawarabayashi KI. (2016) Enhanced estimation of local Intrinsic Dimensionality using auxiliary distances. NII Technical Reports.
- [66] Amsaleg L, Chelly O, Furon T, Girard S, Houle ME, Kawarabayashi Ki, Nett M. Estimating Local Intrinsic Dimensionality. In: Proceedings of the 21th ACM SIGKDD International Conference on Knowledge Discovery and Data Mining - KDD '15, Cd. ACM Press, New York, New York, USA, 2015: 29–38.
- [67] Amsaleg L, Chelly O, Furon T, Girard S, Houle ME, Kawarabayashi Ki, Nett M. (2018) Extreme-value-theoretic estimation of local intrinsic dimensionality. *Data Min Knowl Discov*, 32: 1768–1805.
- [68] Amsaleg L, Chelly O, Houle ME, Kawarabayashi Ki, Radovanović M, Treeratana-jaru W. Intrinsic Dimensionality Estimation within Tight Localities. In: Proceedings of the 2019 SIAM International Conference on Data Mining. Society for Industrial and Applied Mathematics, 2019: 181–189.
- [69] Farahmand AM, Szepesvári C, Audibert JY. Manifold – adaptive dimension estimation. In: Proceedings of the 24th international conference on Machine learning. ACM Press, 2007: 265–272.
- [70] Berenyi A, Somogyvari Z, Nagy AJ, Roux L, Long JD, Fujisawa S, Stark E, Leonardo A, Harris TD, Buzsaki G. (2014) Large-scale, high-density (up to 512 channels) recording of local circuits in behaving animals. *J Neurophysiol*, 111: 1132–1149.
- [71] Benkő Z, Fabó D, Somogyvári Z. Time series and interactions: Data processing in epilepsy research. In: Érdi P, Sen Bhattacharya B, Cochran AL (eds.), *Computational Neurology and Psychiatry*. Springer International Publishing, Cham, 2017: 73–91.
- [72] Bartolomei F, Wendling F, Vignal JP, Kochen S, Bellanger JJ, Badier JM, Le Bouquin-Jeannes R, Chauvel P. (1999) Seizures of temporal lobe epilepsy: identification of subtypes by coherence analysis using stereo-electro-encephalography. *Clin Neurophysiol*, 110: 1741–1754.
- [73] Walker JE. (2008) Power spectral frequency and coherence abnormalities in patients with intractable epilepsy and their usefulness in long-term remediation of seizures using neurofeedback. *Clin EEG Neurosci*, 39: 203–205.

- [74] Hume D. *A Treatise of Human Nature Being an Attempt to Introduce the Experimental Method Into Moral Subjects; and Dialogues Concerning Natural Religion*. Longmans Green & Co, London, 1874.
- [75] Hernán MA, Robins JM. *Causal Inference: What If*. Chapman & Hall/CRC., 2020.
- [76] Glass T, Goodman S, Hernán M, Samet J. (2013) Causal inference in public health. *Annu Rev Public Health*, 34: 61–75.
- [77] Pearl J. *Causality: Models, Reasoning and Inference*. Cambridge University Press, USA, 2009.
- [78] Xiong M, Sebastiani P, Li S, Zhang K, Glymour C, Spirtes P. (2019) Review of Causal Discovery Methods Based on Graphical Models. *Front Genet*, 1: 524.
- [79] Wiener N. *The Theory of Prediction*. In: Beckenbach EF (ed.), *Modern Mathematics for Engineers*, volume 58. McGraw-Hill, New York, 1956: 323–329.
- [80] Granger CWJ. (1969) Investigating Causal Relations by Econometric Models and Cross-spectral Methods. *Econometrica*, 37: 424–438.
- [81] Granger CWJ. (1969) Investigating causal relations by econometric models and cross-spectral methods. *Econometrica*, 37: 424–438.
- [82] Kaminski MJ, Blinowska KJ. (1991) A new method of the description of the information flow in the brain structures. *Biol Cybern*, 65: 203–210.
- [83] Kaminski M, Ding M, Truccolo WA, Bressler SL. (2001) Evaluating causal relations in neural systems: granger causality, directed transfer function and statistical assessment of significance. *Biol Cybern*, 85: 145–157.
- [84] Baccala LA, Sameshima K. (2001) Partial directed coherence: a new concept in neural structure determination. *Biol Cybern*, 84: 463–474.
- [85] Liang H, Ding M, Nakamura R, Bressler SL. (2000) Causal influences in primate cerebral cortex during visual pattern discrimination. *Neuroreport*, 11: 2875–2880.
- [86] Schreiber T. (2000) Measuring information transfer. *Phys Rev Lett*, 85: 461–464.
- [87] Wibral M, Vicente R, Lizier JT (eds.), *Directed Information Measures in Neuroscience. Understanding Complex Systems*. Springer-Verlag Berlin Heidelberg, 2014.

- [88] Sugihara G, May R, Ye H, Hsieh CH, Deyle E, Fogarty M, Munch S. (2012) Detecting causality in complex ecosystems. *Science*, 338: 496–500.
- [89] Takens F. Detecting strange attractors in turbulence. In: Rand DA, Young LS (eds.), *Dynamical Systems and Turbulence, Lecture Notes in Mathematics*, volume 898. Springer-Verlag, 1978: 366–381.
- [90] Deyle ER, Sugihara G. (2011) Generalized theorems for nonlinear state space reconstruction. *PLoS One*, 6: e18295.
- [91] Ye H, Deyle ER, Gilarranz LJ, Sugihara G. (2015) Distinguishing time-delayed causal interactions using convergent cross mapping. *Sci Rep*, 5: 14750.
- [92] Schumacher J, Wunderle T, Fries P, Jakel F, Pipa G. (2015) A Statistical Framework to Infer Delay and Direction of Information Flow from Measurements of Complex Systems. *Neural Comput*, 27: 1555–1608.
- [93] Ma H, Aihara K, Chen L. (2014) Detecting causality from nonlinear dynamics with short-term time series. *Sci Rep*, 4: 7464.
- [94] Hirata Y, Aihara K. (2010) Identifying hidden common causes from bivariate time series: a method using recurrence plots. *Phys Rev E*, 81: 016203.
- [95] Nicholson C, Freeman JA. (1975) Theory of current source-density analysis and determination of conductivity tensor for anuran cerebellum. *J Neurophysiol*, 38: 356–368.
- [96] Mitzdorf U. (1985) Current source-density method and application in cat cerebral cortex: investigation of evoked potentials and EEG phenomena. *Physiol Rev*, 65: 37–100.
- [97] Pettersen KH, Devor A, Ulbert I, Dale AM, Einevoll GT. (2006) Current-source density estimation based on inversion of electrostatic forward solution: Effect of finite extent of neuronal activity and conductivity discontinuities. *J Neurosci Methods*, 154: 116–133.
- [98] Potworowski J, Jakuczun W, Leski S, Wojcik D. (2012) Kernel current source density method. *Neural Comput*, 24: 541–575.
- [99] Somogyvári Z, Cserpán D, István U, Péter E. (2012) Localization of single-cell current sources based on extracellular potential patterns: the spike csd method. *Eur J Neurosci*, 36: 3299–3313.

- [100] Vigario R, Oja E. (2008) BSS and ICA in neuroinformatics: from current practices to open challenges. *IEEE Rev Biomed Eng*, 1: 50–61.
- [101] Aitken P, Fayuk D, Somjen G, Turner D. (1999) Use of Intrinsic Optical Signals to Monitor Physiological Changes in Brain Tissue Slices. *Methods*, 18: 91–103.
- [102] Andrew R, Jarvis CR, Obeidat AS. (1999) Potential Sources of Intrinsic Optical Signals Imaged in Live Brain Slices. *Methods*, 18: 185–196.
- [103] Syková E, Vargová L, Kubinová Š, Jendelová P, Chvátal A. (2003) The relationship between changes in intrinsic optical signals and cell swelling in rat spinal cord slices. *Neuroimage*, 18: 214–230.
- [104] Lipton P. (1973) Effects of membrane depolarization on light scattering by cerebral cortical slices. *The Journal of Physiology*, 231: 365–383.
- [105] Pál I, Nyitrai G, Kardos J, Héja L. (2013) Neuronal and Astroglial Correlates Underlying Spatiotemporal Intrinsic Optical Signal in the Rat Hippocampal Slice. *PLoS One*, 8: e57694.
- [106] Világi I, Klapka N, Luhmann HJ. (2001) Optical recording of spreading depression in rat neocortical slices. *Brain Res*, 898: 288–296.
- [107] Cerne R, Haglund MM. (2002) Electrophysiological correlates to the intrinsic optical signal in the rat neocortical slice. *Neurosci Lett*, 317: 147–150.
- [108] De Guzman P, D’Antuono M, Avoli M. (2004) Initiation of electrographic seizures by neuronal networks in entorhinal and perirhinal cortices in vitro. *Neuroscience*, 123: 875–886.
- [109] Jones RS, Heinemann U. (1988) Synaptic and intrinsic responses of medial entorhinal cortical cells in normal and magnesium-free medium in vitro. *J Neurophysiol*, 59: 1476–1496.
- [110] Miles R, Wong RK, Traub RD. (1984) Synchronized afterdischarges in the hippocampus: Contribution of local synaptic interactions. *Neuroscience*, 12: 1179–1189.
- [111] Borbély S, Körössy C, Somogyvári Z, Világi I. (2014) In vitro intrinsic optical imaging can be used for source determination in cortical slices. *Eur J Neurosci*, 39: 72–82.

- [112] Kántor O, Benkő Z, Énzsöly A, Dávid C, Naumann A, Nitschke R, Szabó A, Pálfi E, Orbán J, Nyitrai M, Németh J, Szél Á, Lukáts Á, Völgyi B. (2016) Characterization of connexin36 gap junctions in the human outer retina. *Brain Struct Funct*, 221: 2963–2984.
- [113] Rhodes C, Morari M. (1997) The false nearest neighbors algorithm: An overview. *Comput Chem Eng*, 21: S1149 – S1154.
- [114] Krakovská A, Mezeiová K, Budáčová H. (2015) Use of False Nearest Neighbours for Selecting Variables and Embedding Parameters for State Space Reconstruction. *Journal of Complex Systems*, 2015: 1–12.
- [115] Gautama T, Mandic DP, Van Hulle MM. A differential entropy based method for determining the optimal embedding parameters of a signal. In: *ICASSP, IEEE International Conference on Acoustics, Speech and Signal Processing - Proceedings*, volume 6. 2003: 29–32.
- [116] Pedregosa F, Varoquaux G, Gramfort A, Michel V, Thirion B, Grisel O, Blondel M, Prettenhofer P, Weiss R, Dubourg V, Vanderplas J, Passos A, Cournapeau D, Brucher M, Perrot M, Duchesnay E. (2011) Scikit-learn: Machine learning in Python. *J Mach Learn Res*, 12: 2825–2830.
- [117] Virtanen P, Gommers R, Oliphant TE, Haberland M, Reddy T, Cournapeau D, Burovski E, Peterson P, Weckesser W, Bright J, van der Walt SJ, Brett M, Wilson J, Jarrod Millman K, Mayorov N, Nelson ARJ, Jones E, Kern R, Larson E, Carey C, Polat İ, Feng Y, Moore EW, VanderPlas J, Laxalde D, Perktold J, Cimrman R, Henriksen I, Quintero EA, Harris CR, Archibald AM, Ribeiro AH, Pedregosa F, van Mulbregt P, Contributors S. (2020) SciPy 1.0: Fundamental Algorithms for Scientific Computing in Python. *Nat Methods*, 17: 261–272.
- [118] Ryzhii E, Ryzhii M. (2014) A heterogeneous coupled oscillator model for simulation of ECG signals. *Comput Methods Programs Biomed*, 117: 40–49.
- [119] Bradley AP. (1997) The use of the area under the ROC curve in the evaluation of machine learning algorithms. *Pattern Recognit*, 30: 1145–1159.
- [120] Ichimaru Y, Moody GB. (1999) Development of the polysomnographic database on CD-ROM. *Psychiatry Clin Neurosci*, 53: 175–177.
- [121] Goldberger AL, Amaral LA, Glass L, Hausdorff JM, Ivanov PC, Mark RG, Mietus JE, Moody GB, Peng CK, Stanley HE. (2000) PhysioBank, PhysioToolkit,

- and PhysioNet: components of a new research resource for complex physiologic signals. *Circulation*, 101: E215–E220.
- [122] Van Rossum G, Drake FL. *Python 3 Reference Manual*. CreateSpace, Scotts Valley, CA, 2009.
- [123] Oliphant TE. *A guide to NumPy, volume 1*. Trelgol Publishing USA, 2006.
- [124] Hunter JD. (2007) Matplotlib: A 2d graphics environment. *Comput Sci Eng*, 9: 90–95.
- [125] MATLAB (2020) MATLAB version 9.8.0.1396136 (R2020a). The Mathworks, Inc., Natick, Massachusetts.
- [126] Lombardi G. (Retrieved July 16, 2020) Intrinsic dimensionality estimation techniques. MATLAB Central File Exchange.
- [127] Garcia S, Guarino D, Jaillet F, Jennings T, Pröpper R, Rautenberg P, Rodgers C, Sobolev A, Wachtler T, Yger P, Davison A. (2014) Neo: an object model for handling electrophysiology data in multiple formats. *Front Neuroinf*, 8:10.
- [128] Gramfort A, Luessi M, Larson E, Engemann D, Strohmeier D, Brodbeck C, Goj R, Jas M, Brooks T, Parkkonen L, Hämäläinen M. (2013) MEG and EEG data analysis with MNE-Python. *Front Neurosci*, 7: 267.
- [129] Abbott R, et al. (2019) Open data from the first and second observing runs of Advanced LIGO and Advanced Virgo. *ArXiv*.
- [130] Benkő Z, Stippinger M, Rehus R, Bencze A, Fabó D, Hajnal B, Eröss L, Telcs A, Somogyvári Z. (2020) Manifold-adaptive dimension estimation revisited. *ArXiv*, 1–21.
- [131] Laplace PS. (1986) Memoir on the Probability of the Causes of Events. *Statistical Science*, 1: 364–378.
- [132] Hein M, Audibert JY. Intrinsic dimensionality estimation of submanifolds in  $\mathbb{R}^d$ . In: *Proceedings of the 22nd international conference on Machine learning - ICML '05*. ACM Press, 2005: 289–296.
- [133] Borbély S, Halasy K, Somogyvári Z, Détári L, Világi I. (2006) Laminar analysis of initiation and spread of epileptiform discharges in three in vitro models. *Brain Res Bull*, 69: 161–167.

- [134] Department of Justice of The United States (2012). Barclays bank PLC admits misconduct related to submissions for the london interbank offered rate and the euro interbank offered rate and agrees to pay \$160 million penalty.
- [135] Snider C, Youle T. (2009) Diagnosing the libor: strategic manipulation member portfolio positions. Working paper- facultywashingtonedu.
- [136] Snider C, Youle T. (2010) Does the libor reflect banks' borrowing costs? SSRN.
- [137] Snider C, Youle T. (2012) The fix is in: Detecting portfolio driven manipulation of the libor. SSRN.
- [138] Rieke C, Andrzejak RG, Mormann F, Lehnertz K. (2004) Improved statistical test for nonstationarity using recurrence time statistics. *Phys Rev E*, 69: 046111.
- [139] Kriegel HP, Kröger P, Schubert E, Zimek A. LoOP: Local outlier probabilities. In: *International Conference on Information and Knowledge Management, Proceedings*. 2009.
- [140] Tajima S, Yanagawa T, Fujii N, Toyoizumi T. (2015) Untangling Brain-Wide Dynamics in Consciousness by Cross-Embedding. *PLoS Comput Biol*, 11: e1004537.
- [141] Mormann F, Lehnertz K, David P, Elger C. (2000) Mean phase coherence as a measure for phase synchronization and its application to the EEG of epilepsy patients. *Physica D*, 144: 358–369.
- [142] Bullmore E, Brammer M, Bourlon P, Alarcon G, Polkey C, Elwes R, Binnie C. (1994) Fractal analysis of electroencephalographic signals intracerebrally recorded during 35 epileptic seizures: evaluation of a new method for synoptic visualisation of ictal events. *Electroencephalogr Clin Neurophysiol*, 91: 337–345.
- [143] Päivinen N, Lammi S, Pitkänen A, Nissinen J, Penttonen M, Grönfors T. (2005) Epileptic seizure detection: A nonlinear viewpoint. *Comput Methods Programs Biomed*, 79: 151–159.
- [144] Esteller R, Vachtsevanos G, Echauz J, Henry T, Pennell P, Epstein C, Bakay R, Bowen C, Litt B. Fractal dimension characterizes seizure onset in epileptic patients. In: *1999 IEEE International Conference on Acoustics, Speech, and Signal Processing. Proceedings. ICASSP99 (Cat. No.99CH36258)*, volume 4. IEEE, 1999: 2343–2346.
- [145] Rutecki P. (2006) Ions in the Brain: Normal Function, Seizures, and Stroke. *Neurology*, 66: 618–618.

- [146] Buchheim K, Wessel O, Siegmund H, Schuchmann S, Meierkord H. (2005) Processes and components participating in the generation of intrinsic optical signal changes in vitro. *Eur J Neurosci*, 22: 125–132.
- [147] Pereira A. (2017) Astroglial hydro-ionic waves guided by the extracellular matrix: An exploratory model. *J Integr Neurosci*, 16: 57–72.
- [148] Toft-Bertelsen TL, Larsen BR, MacAulay N. (2018) Sensing and regulation of cell volume – We know so much and yet understand so little: TRPV4 as a sensor of volume changes but possibly without a volume-regulatory role? *Channels (Austin)*, 12: 100–108.
- [149] Larsen BR, MacAulay N. (2017) Activity-dependent astrocyte swelling is mediated by pH-regulating mechanisms. *Glia*, 65: 1668–1681.
- [150] Fayuk D, Aitken PG, Somjen GG, Turner DA. (2002) Two different mechanisms underlie reversible, intrinsic optical signals in rat hippocampal slices. *J Neurophysiol*, 87: 1924–1937.
- [151] Mané M, Müller M. (2012) Temporo-Spectral Imaging of Intrinsic Optical Signals during Hypoxia-Induced Spreading Depression-Like Depolarization. *PLoS One*, 7.
- [152] Nicholson C, Syková E. (1998) Extracellular space structure revealed by diffusion analysis. *Trends Neurosci*, 21: 207–215.
- [153] Ye H, Beamish RJ, Glaser SM, Grant SC, Hsieh CH, Richards LJ, Schnute JT, Sugihara G. (2015) Equation-free mechanistic ecosystem forecasting using empirical dynamic modeling. *Proc Natl Acad Sci U S A*, 112: E1569–E1576.

## 10 Publications

### Peer reviewed publications related to the dissertation

Kántor O, Benkő Zs, Énzöly A, Dávid Cs, Naumann A, Nitschke R, Szabó A, Pálfi E, Orbán J, Nyitrai M, Németh J, Szél Á, Lukáts Á, and Völgyi B. (2016) Characterization of connexin36 gap junctions in the human outer retina. *Brain Structure and Function*, 221:2963–2984

Benkő Zs, Moldován K, Szádeczky-Kardoss K, Zalányi L, Borbély S, Világi I, and Somogyvári Z. (2019) Causal relationship between local field potential and intrinsic optical signal in epileptiform activity in vitro. *Scientific Reports*, 91:5171

Benkő Zs, Fabó D, and Somogyvári Z. Time Series and Interactions: Data Processing in Epilepsy Research. In P Érdi, B Sen Bhattacharya, and A Cochran (editors), *Computational Neurology and Psychiatry*, Springer, Cham, 2017: 73–91.

### Preprints related to the dissertation

Benkő Zs, Bábel T, and Somogyvári Z. (2020) How to find a unicorn: a novel model-free, unsupervised anomaly detection method for time series. *arXiv:2004.11468*

Benkő Zs, Stippinger M, Rehus R, Bencze A, Fabó D, Hajnal B, Erőss L, Telcs A, and Somogyvári Z. (2020) Manifold-adaptive dimension estimation revisited. *arXiv:2008.03221*

### Other publications

Kántor O, Szarka G, Benkő Zs, Somogyvári Z, Pálfi E, Baksa G, Rácz G, Nitschke R, Debertin G, and Völgyi B. (2018) Strategic Positioning of Connexin36 Gap Junctions Across Human Retinal Ganglion Cell Dendritic Arbors. *Frontiers in Cellular Neuroscience*

Benkő Zs, Zlatniczki Á, Stippinger M, Fabó D, Sólyom A, Erőss L, Telcs A, and Somogyvári Z. (2018) Complete Inference of Causal Relations between Dynamical Systems. *arXiv:1808.10806*

## 11 Acknowledgements

I acknowledge that this work could not manifest itself in this form without the help of many people. I am grateful to my master, Zoltán Somogyvári for his guidance and for being an inspiration with his optimistic approach towards life. I would like to thank my colleagues in the Theoretical Neuroscience and Complex Systems research group at Wigner Research Centre for Physics the refreshing, vivid atmosphere up at the hill and that they were open to answer any question. Also, I am thankful for Orsolya Kántor and Béla Völgyi for the opportunity to gather experiences for 3 weeks at Freiburg during my phd studies.

I am thankful for the support of my friends, especially for the project managers: Alex Balogh and Réka Bodnár. I feel gratitude towards my grandfather, who started this whole journey – maybe unwillingly – by telling me tales about electrons and lasers since I was 3. I am grateful for my parents and brothers and sisters for the warm atmosphere in which I grew up. I am thankful for my wife and children for giving me purpose.